A critical evaluation of the design of removable cover-plate header boxes for air-cooled heat exchangers

by

Lionel Prinsloo

Submitted in partial fulfilment of the requirements for the degree

Master of Engineering

in the Faculty of

Engineering, Built Environment and Information Technology

University of Pretoria

April 2011

A critical evaluation of the design of removable cover-plate header boxes for air-cooled heat exchangers

Author: Lionel Prinsloo
Supervisor: Dr. Helen Inglis
Co-supervisor: Dr. Schalk Kok
Department: Mechanical and Aeronautical Engineering
Degree: Master of Engineering

Keywords: air-cooled heat exchanger, removable cover-plate header box, pressure vessel, finite element analysis, design by formula, design by analysis

Abstract

Large air-cooled heat exchangers (ACHEs) are most popularly implemented in the petrochemical and power industries at arid locations. They operate on a simple concept of convective heat transfer, whereby air in the surrounding atmosphere is caused to flow across a tube bundle, which in turn transports a process fluid. The distribution and direction of the process fluid flow may furthermore be guided via a set of appropriately located header boxes, which essentially consist of a collection of welded flat plates and nozzle attachments. Perforations on one of the faces of these boxes serve as an interface to the tube bundle.

The overall design and construction of an ACHE is commonly regulated by an American Petroleum Institute (API) standard, which is required to be used in conjunction with acceptable design codes. In spite of this, the design of certain header box configurations remains of prominent concern. It is the focus of the present study to investigate the approach adopted for a header box variant labelled as the removable cover type. In this configuration, one of the plates used to construct the header box is fastened and sealed by a collection of bolted joints and a gasket, allowing it to be removed.

One appropriate design code for the header box equipment is the ASME (American Society of Mechanical Engineers) boiler and pressure vessel code. However, it provides no specific approach pertaining to the removable cover design. Instead it has been commonplace in industry for a number of aspects from this code to be synthesized, together with a collection of assumptions surrounding the header box behaviour, into an all encompassing design by rule approach. In this approach, the header box behaviour is accepted as being planar, whilst circumstances such as nozzle attachments and associated loading would suggest that a more comprehensive approach should be undertaken.

The aim of the present study is therefore to critically evaluate the current practice, and establish its adequacy. To do so, a detailed three-dimensional finite element model (FEM) of an example header box design is developed. Subsequent comparisons with the stress distribution predicted via current practice show that the existing analytical model gives inaccurate and, in cases, overly conservative results. A new analytical approach developed from rigid frame theory is demonstrated to provide improved correlation with FEM.

The linear elastic design by analysis approach, presented in the ASME code, is also utilised as a method for establishing design adequacy. Results obtained via design by analysis incorporating the finite element method are shown to be less conservative than those arising from design by rule methods. The design by analysis approach is also used to conduct a more detailed investigation of nozzle placement and external loading. In general, the effect of including a nozzle did not result in a significant increase in side plate stress, with failure more likely to occur within the nozzle wall.

Acknowledgements

I would like to extend a word of thanks to everyone that supported and contributed towards this work. I am grateful to those listed below in particular.

- **SASOL** – SASOL granted me a bursary, and provided funding for my post-graduate studies. I would also like to acknowledge my mentors at SASTECH, Ashveer Maharaj and Francois Lombaard, for suggesting the topic which lead to this work, and their support throughout. In addition, thank you to Jerry Wykes for his guidance at the beginning of the project.

- **ESTEQ Engineering** – Thank you to everyone who assisted me with respect to the FEA software packages, especially Gerrit Visser who also provided important source code from their ASME plug-in.

- **Advanced Structural Mechanics** – Thank you to Prof Rudy du Preez for the few consultations we had. I appreciate the insight you provided, especially within the context of this work.

- **Engineering Systems** – Gratitude is due to David Shklaz, who gave permission to investigate and reference the methods used by the Optivessel software package.

- **Study leaders** – Thank you to Dr Schalk Kok and Dr Helen Inglis for their support and guidance throughout my Master's.

- My sincerest gratitude is due to my parents and sister for their unwavering support and encouragement.

Table of Contents

List of Figures

List of Tables

List of Symbols

Note that some of the symbols were excluded from this list, since they are defined at appropriate locations throughout the document.

A_b	Actual total cross-sectional area of the bolts
A_{m1}	Minimum required total bolt area for operating conditions
A_{m2}	Minimum required total bolt area for initial loading
A_m	Maximum of A_{m1} and A_{m2}
b	Effective gasket seating width
b_0	Basic gasket seating width
D_c	Recalculated internal tube sheet width
d_c	Recalculated header depth
E	Young's modulus of elasticity
E_l	Ligament efficiency
F	Force
G	Recalculated gasket width
H	Recalculated gasket length
H_1	Reaction force for current design practice (see Figure 4-4)
h	Flange lever arm length for header walls stress calculation
h_1	Flange lever arm length for flange thickness calculation
I_s	Second moment of area of the side plate
I_t	Second moment of area of the tube sheet
M	Bending moment
M_1	Secondary bending moment used in current design practice (see Figure 4-4)
M_{jf}	Bending moment for flange stress calculation
M_{jw}	Bending moment for header walls stress calculations
M_{p2}	Bending moment at the centre of the cover-plate (current approach)
M_{p4}	Bending moment at the centre of the side plate (current approach)
M_{p8}	Bending moment at the centre of the tube sheet (current approach)
M_{px}	Bending moment at the centre most tube row (current approach)
P	Pressure
P_b	Primary bending equivalent stress
P_L	Local primary membrane equivalent stress
P_m	General primary membrane equivalent stress

p_b	Actual bolt pitch
$p_{b,max}$	Maximum allowed bolt pitch
$p_{b,min}$	Minimum allowed bolt pitch
Q	Secondary equivalent stress
T	Temperature
t	Thickness
t_e	End-plate thickness
t_n	Nozzle wall thickness
S	Maximum allowable stress
S^e	Von Mises equivalent stress
S_s	Nominal shear stress
S_b	Nominal bending stress
S_{b4}	Bending stress at the centre of the side plate (current approach)
S_{b5}	Bending stress at the end of the side plate (current approach)
S_{b6}	Bending stress at the end of the tube sheet (current approach)
S_{b7}	Bending stress at the centre of the tube sheet (current approach)
S_{b8}	Bending stress at the centre most tube row (current approach)
S_c	Combined bending stress
S_y	Yield strength
W_1	Reaction force for current design practice (see Figure 4-4)
W_2	Reaction force for current design practice (see Figure 4-4)
W_{m1}	Total bolt load required for operating conditions
W_{m2}	Minimum initial bolt load
W_j	Total bolt load

Greek symbols:

θ	Angle of rotation
σ	Stress component
σ^b	Linearized bending stress component
σ^m	Linearized membrane stress component
v	Poisson's ratio

Abbreviations

ACHE	Air-Cooled Heat Exchanger
API	American Petroleum Institute
ASME	The American Society of Mechanical Engineers
DbA	Design by Analysis
DbR	Design by Rule
DOF	Degrees Of Freedom
FE	Finite Element
FEA	Finite Element Analysis
FEM	Finite Element Method
MATLAB	Matrix Laboratory
MPC	Multi-Point Constraint
MSC	MacNeal-Schwendler Corporation
Nastran	NASA Structural Analysis
NPS	Nominal Pipe Size
PCL	Patran Command Language
QP	Quadratic Programming
RF	Rigid Frame
SASOL	Suid-Afrikaanse Steenkool-, Olie- en Gaskorporasie
SASTECH	SASOL Technology
SCL	Stress Concentration Line
SQP	Sequential Quadratic Programming

1 Introduction

Large air-cooled heat exchangers (ACHE) are most popularly implemented in the petrochemical and power industries in circumstances of water scarcity. Their operation is founded on a simple principle, whereby ambient air is caused to flow across an array of tubes which transport a process fluid. This results in an accelerated exchange of heat between the process fluid and the surrounding air through the mechanism of convection. The flow of the process fluid through the tube bundle is guided by header boxes.

In recent years the mechanical design of certain header box variants has grown to be of significant concern at SASOL's petrochemical plants in Sasolburg and Secunda. This has been prompted by the inability of existing methods to deal with newly formulated requirements regarding nozzle attachments and external loading originating from the American Petroleum Institute (API) standard 661 [1]. Additionally, the current design approach appears to rely on questionable assumptions about the behaviour of header boxes. As a result, there is a need for the design process to be critically reviewed, and appropriate alternatives to be suggested where possible. Within certain limitations, these necessities drive the present work.

In particular, this study will focus on the removable cover type header box introduced in Section 1.1. The conventional design process is elaborated upon with reference to the experience of SASOL in Section 1.2, with attention being given to the relevant concerns. Finally, the project objectives and scope are discussed, and an overview of the thesis is provided.

1.1 Overview of ACHE and header box designs

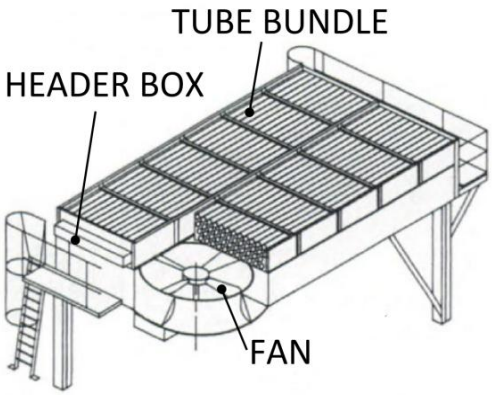

Figure 1-1: Illustration of a typical forced draught ACHE, showing its primary constituents (adapted from [2])

Figure 1-1 shows the most important constituents in the construction of an ACHE, including a large fan for creating a draught, and a tube bundle to transport the process fluid. The flow of the process fluid is guided by header boxes positioned at either end of the tube bundle. In general, the process fluid enters an in/out header box via a nozzle attachment and is directed into a collection of tubes by means of a perforated plate (tube sheet) on one of the box's sides. Once the flow traverses the tube bundle, it enters a return header box, again by means of a tube sheet, and is caused to flow in the reverse direction along the tube bundle in a different collection of tubes so as to re-enter the in/out

header box. At this point the fluid may be discharged, or guided towards completing more passes along the tube bundle, depending on the thermal design of the ACHE. Header boxes are compartmentalized by means of partition plates to separate the stages of fluid flow.

In general, an ACHE is categorized according to the method by which the cooling airstream is generated. Depending on the configuration of the fan, we may denote an ACHE as being of the forced or induced draught kind (see Figure 1-2).

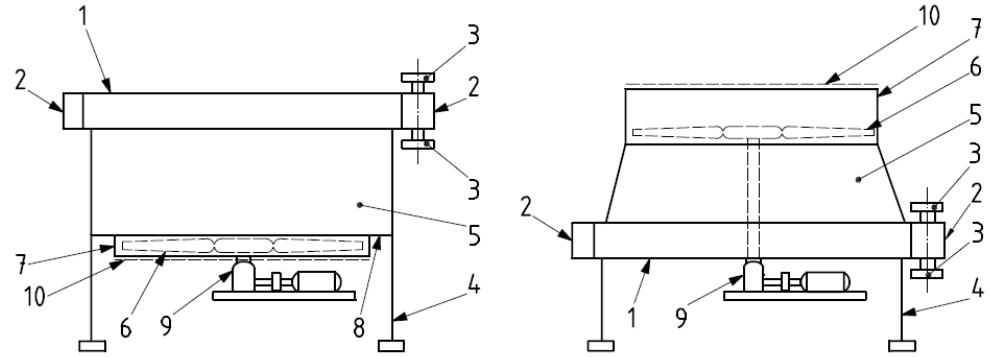

a) Forced draught b) Induced draught

Key

1	tube bundle	6	fan
2	header	7	fan ring
3	nozzle	8	fan deck
4	supporting column	9	drive assembly
5	plenum	10	fan guard

Figure 1-2: Typical components of an air-cooled heat exchanger [1]

In the forced draught case, a fan is installed below the tube bundle and is used to blow cool air across it. This allows the fan assembly to operate in cooler conditions which is beneficial in a number of ways, for example reduced power consumption and improved maintainability. On the other hand, a forced draught configuration is susceptible to adverse environmental conditions and recirculation, i.e. the re-entry of the warm exit air at the top around the sides of the tube-bundle, resulting in reduced efficiency.

In the induced draught configuration the fan is installed above the tube bundle and used to draw air across. Since the fan and motor now operate in the warmer exit airstream, power consumption is higher and maintenance tasks become more difficult. Conversely, this configuration is less susceptible to environmental effects due to its enclosed nature. A higher airstream velocity at the top also mitigates recirculation effects.

The configurations depicted in Figure 1-2 represent the vast majority of ACHEs in the petrochemical industry, and serve to highlight the placement of header boxes and accompanying nozzle attachments.

Nee [3] identifies the following classes of header box designs: removable cover; shoulder-plug and manifold types. This discussion will consider the first two classes. The most significant factors when selecting a suitable design are maintainability and ability to sustain pressure. Maintainability is

predominantly affected by the degree of difficulty involved in mechanical cleaning. In the sections to follow the attributes of each class of design are discussed in more detail.

1.1.1 Removable cover type

Two configurations of removable cover headers are illustrated in API 661 [1]: the removable cover-plate and removable bonnet header. Removable cover header box designs allow for mechanical cleaning and simpler construction of partition plates, since one face of the box is detachable, typically by means of a bolted rectangular flange-plate connection. They are ideal for applications with severe fouling conditions.

A gasket is typically used to seal the flange-plate connection, which consequently places restrictions on the configuration of the partition plates, and dramatically reduces their effectiveness in providing stiffening support in comparison with the shoulder-plug type. From Nee [3], a typical upper bound on the operating pressure of a removable cover header is in the range of 2 MPa, although in some industrial applications much higher operating pressures have been sustained [4].

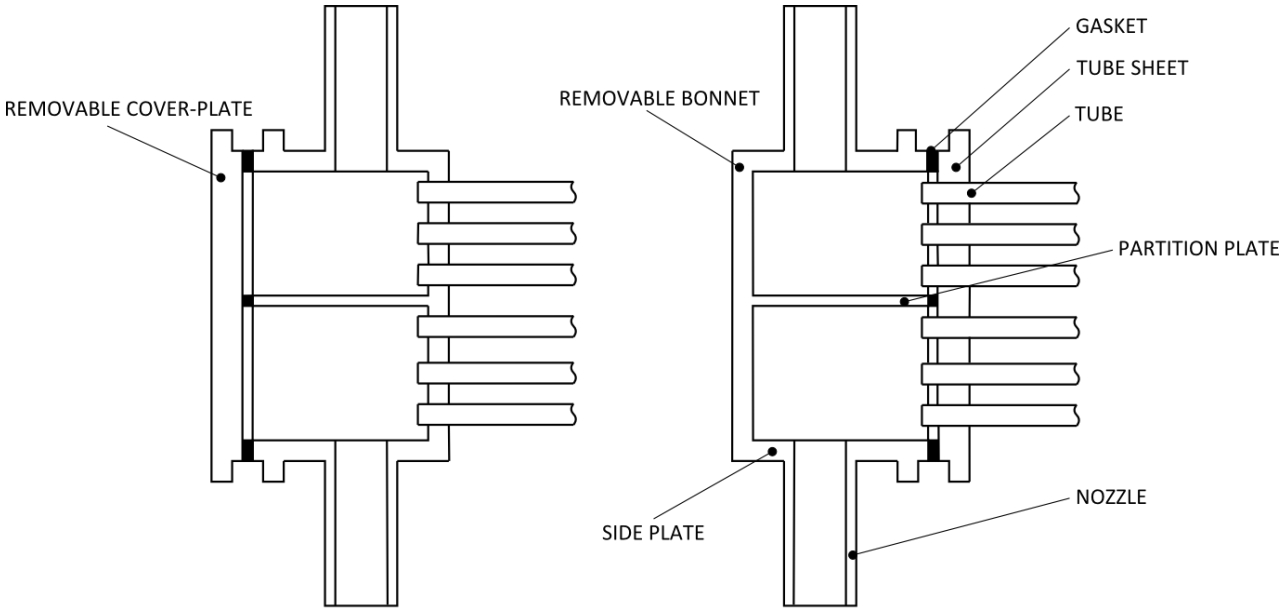

(a) Removable cover-plate header (b) Removable bonnet header

Figure 1-3: Layout of two removable header types from side-on perspective (adapted from [1])

1.1.2 Shoulder-plug type

In shoulder-plug headers none of the sides of the box are removable. Instead, threaded plug-holes are used for the installation of tubes (see Figure 1-4). The box therefore cannot be opened, which makes the manufacturing of partition plates a more challenging task, and cleaning a cumbersome process since tubes have to be dealt with individually.

The design however does away with the need for gaskets, and allows for a considerably higher operating pressure as compared to removable cover designs. A typical maximum pressure is in the

range of 7 MPa or more. At present, this configuration is the most common header type used in industry.

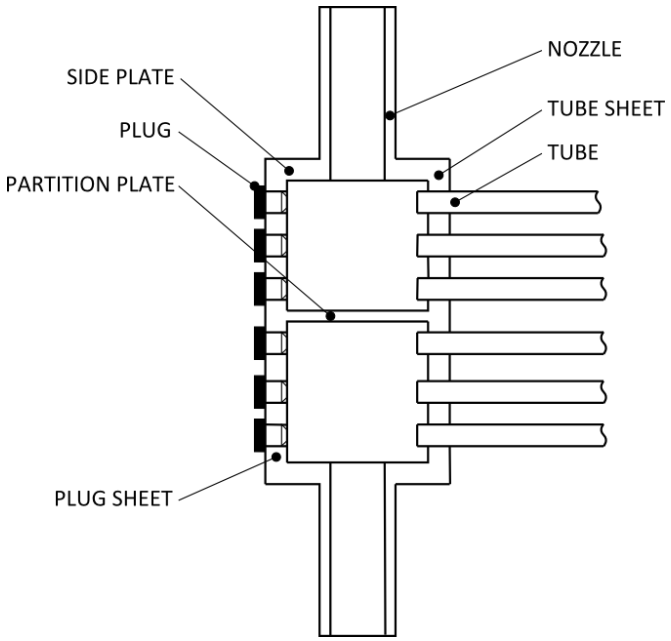

Figure 1-4: Layout of a shoulder-plug header box from side-on perspective (adapted from [1])

1.1.3 Practical considerations for the design of header boxes

It should be clear that the removable cover and shoulder-plug configurations have very similar designs. They essentially represent a collection of flat plates welded together so as to form an enclosed rectangular space, except that in the one scenario a plate is left detachable. This primarily results in differences in their maintainability, and ability to sustain pressure. On the one hand the removable cover-plate type eases the cleaning process in circumstances of fouling, whilst the shoulder-plug design presents a more robust option in terms of operating pressure. One of the main reasons for the superiority of the shoulder-plug design in this regard relates to the effectiveness of partition plates in providing structural support.

Pass partition plates are included in a header box to guide the flow of process fluid. They also serve the purpose of supporting the header structure, essentially helping to resist the bowing of the tube sheet through reducing the effective size of the header box. This structural role is most effective in a shoulder-plug design, since the support of a partition plate is equally enforced on either side of the box (it is welded into place on four sides). In contrast, cover-plate headers employ gaskets which dramatically reduce the supporting effect.

If one were to consider a header with six tube rows and six passes of flow in and out of the box (i.e. each row is a pass) three partition plates would be required. This translates to a maximum of two tube rows being unsupported in the case of a shoulder-plug header. In a cover-plate header the partition plates provide little support against bowing of the header box. Conservatively one could therefore assume all six of the tube rows to remain unsupported. Referring to Table 1-1 for a 3/4 inch thickness, one can observe a substantial difference in allowable working pressure. The cover-

plate header would only be able to sustain 0.48 MPa in comparison to 3.28 MPa for the case of a shoulder-plug header.

Table 1-1: Estimated maximum allowable design pressure [MPa] for shoulder-plug or cover-plate headers [3]

Number of unsupported tube rows	Header thickness, in				
	3/4	7/8	1	1-1/8	1-1/4
2	3.28	4.48	5.79	7.24	8.79
3	1.69	2.34	3.14	4.00	4.90
4	1.01	1.45	1.90	2.48	3.10
5	0.66	0.97	1.28	1.65	2.10
6	0.48	0.69	0.93	1.21	1.48
Note: This table applies for the following scenario: 1-in tubes, 2-1/2-in triangular pitch, SA-515 gr. 70 material, corrosion allowance 1/8 in.					

A further method for reducing a header's effective size is to minimize the width of the side plates. This dimension is commonly governed by the size of a nozzle attachment. Header boxes can have multiple nozzle attachments, typically ranging from two to six inches in diameter. In an effort to keep the side plate width short, large nozzles are in some cases flattened at the end which is welded to the header side plate, so as to create an oval shape of smaller width.

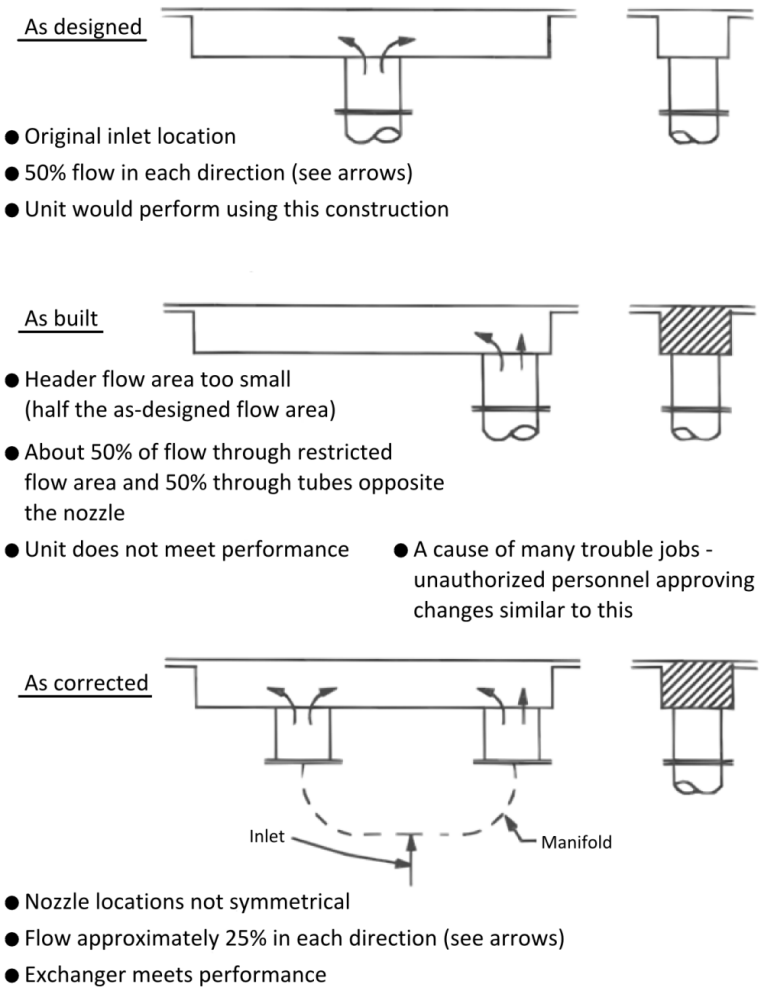

Figure 1-5: Example header distribution problem (adapted from [3])

From the perspective of the process flow distribution and heat exchanger performance it is important for nozzles to be placed appropriately. In the case of a single nozzle, it should be placed at the center of the header so as to allow half of the flow to distribute to either side of the nozzle. When two nozzles are included they are ideally positioned at a quarter and three-quarters of the total header box length. In this scenario it is assumed that each nozzle accounts for half of the total flow. As a result of piping needs however, nozzles are frequently placed at disadvantageous locations with respect to the distribution of flow. A good example of this is illustrated in Nee [3] (shown in Figure 1-5). Poor nozzle placement resulted in a 70 % decrease in desired cooling. This necessitated a re-design of the header box and an extra nozzle had to be included, which required an extra take-off from the supply line.

The above example illustrates the fact that, although undesirable, it is possible for a nozzle to be placed at any point along a header depending on the piping arrangement and space provided, as well as the requirements of the design engineer. From a structural perspective, provision must therefore be made to ensure safe operation of the header box under all circumstances. In particular, care must be taken in designing the system to safely sustain external loading requirements associated with nozzle attachments (presented in API 661 [1]), for which sensitivity to nozzle placement may exist.

1.2 Header box design process and concerns

The present study results from concerns over header box designs at SASOL, a large petrochemical company based in South Africa. In order to familiarize himself with these concerns, and to gain understanding of the design process, the author had numerous contact sessions with personnel at SASOL Technology (also known as SASTECH) in Secunda. SASTECH is responsible for reviewing the designs of heat exchanger equipment, frequently purchased from a local ACHE company.

The overall design and construction of a large ACHE is governed by a standard, such as that developed by the American Petroleum Institute (API), API 661 [1]. This standard does not necessarily provide guidelines for the appropriate design procedures (i.e. design calculations and so forth) to be followed for each of the components. It is therefore a requirement that the standard be used in conjunction with a design code, a popular one being the ASME boiler and pressure vessel code [5].

Local ACHE companies generally make use of in-house mechanical design software, such as Optivessel [6], to ensure the quality of their header box products. Optivessel [6] itself draws from numerous design codes/standards, including Section VIII of the ASME code [5]. For header boxes in particular, the software makes use of the design by rule approach. In short, design by rule is based on a set of simple formulas to determine either the minimum thickness or the maximum allowable working pressure for pressure load conditions [7]. It represents a quick and simple method, which reduces engineering costs for vessel design.

Design by rule methods are presented in Division 1, Section VIII of the ASME code [5]. Mandatory Appendix 13 of this division provides for vessels of noncircular cross section, into which category both the removable cover and shoulder-plug designs fall. Details do exist for shoulder-plug designs. However, no comprehensive approach is presented for the design of removable cover headers.

Consequently, there are concerns over the accuracy of the methods and representativeness of the assumptions adopted in design software such as Optivessel [6]. It therefore becomes necessary to establish the adequacy of this software in this scenario.

Furthermore, API 661 [1] has requirements for external loading applied to nozzle attachments, which would be difficult to incorporate in a design by rule approach. Unsurprisingly, these mandatory requirements are not considered by the Optivessel [6] design software. Because of the complexity involved, a more advanced method of design may be required. For this reason, SASOL has, in the past, contracted third party mechanical design companies to perform Finite Element Analysis (FEA), whereby the design by analysis method is followed. Requirements for design by analysis are presented in Part 5 of Division 2, Section VIII of the ASME code [5]. In general, linear elastic methods, rules for stress categorization, and appropriate limits are used to evaluate the design loading conditions of the vessel [7]. This method requires a higher degree of engineering. Nevertheless, uncertainty remains over how analysis of the loading requirements is to be performed, as well as the extent of their effect on the outcome of a design.

1.3 Project objectives

The header box design concerns are summarized in the following three questions.

1. Is the current design practice, including software such as Optivessel, adequate?
2. Is it necessary for a more comprehensive approach, such as the finite element method to be adopted?
3. What is the importance of a nozzle attachment, with respect to location and external loading, in terms of design?

The primary objective is to perform a critical evaluation of the design of removable cover-plate header boxes by addressing each of the questions above within a limited scope.

A secondary objective is to investigate the formulation of a superior design by rule approach. A comprehensive design by rule method is especially appealing due to its efficiency.

1.4 Project scope

- Only the removable cover-plate design is studied.
- A single representative header box design is used throughout.
- Pass partition plates, interaction between the tubes and tube sheet, and perforations are disregarded.
- The only loadings considered are bolt pre-tension, operating pressure and external loading associated with nozzle attachments.
- Only linear elastic finite element analyses are performed.
- Fluid flow and temperature effects are not studied.

1.5 Thesis overview

Chapter 2 provides the reader with an overview of the design code (ASME [5]) and standard (API 661[1]) which have bearing on the problem. Both the design by rule and design by analysis methods are elaborated upon.

In Chapter 3 the details of a representative header box design are illustrated. This single design is referred to throughout the thesis.

Chapter 4 provides an illustration of current design practice. The process undertaken by Optivessel [6] in particular is explained in detail, with results for the representative header box design being provided, and critiqued. Subsequently, Chapter 5 presents rigid frame theory as a method for developing a superior design by rule approach. A variety of models are formulated in an effort to capture the header box behaviour accurately. Nozzle attachments are however neglected.

In Chapter 6 a comprehensive finite element model of the representative design is developed without regard for nozzle attachments. Certain implications for design by analysis are also introduced, and used to demonstrate the importance of modelling accuracy. In Chapter 7, the results for Optivessel [6], rigid frame models, and the comprehensive finite element model are compared and discussed.

In Chapter 8 a nozzle attachment is finally incorporated into the finite element model, and appropriate analyses performed. At this point, a review of the design approaches is made.

Chapter 9 serves to conclude the thesis. It provides an overview and summarizes the significant outcomes of the study.

2 Overview of design codes/standards and requirements

Pressure vessels are containers designed to hold pressure, either internal or external. This pressure may be obtained from an external source or by the application of heat from a direct or indirect source as a result of a process, or any combination thereof (ASME Section VIII [5]). It is imperative for these containers to be designed adequately since any shortcomings may pose a significant safety hazard. It is for this reason that the design and certification of pressure vessels is legally required to be governed by codes and standards [8]. One of the more popular design codes is the ASME code of construction [5]. A further international standard which deals with air-cooled heat exchangers is API standard 661 [1].

2.1 ASME boiler and pressure vessel code Section VIII

The principal requirements in pressure vessel design are the determination of loads and boundary conditions. These should be determined as thoroughly and accurately as possible, and should be dealt with in a conservative manner. In general, loads are determined on the basis of past experience, design codes, calculations, or testing. Once the loads have been established, stresses can be calculated through either of two approaches in the ASME code [5], design by rule or design by analysis. Subsequently, the stresses must be compared with appropriate allowable limits in the determination of design adequacy.

2.1.1 Division 1: rules for construction of pressure vessels ("design by rule")

Division 1 provides a number of formulae to compute stresses due to internal and external pressures, and makes use of allowable values to determine either the minimum thickness or the maximum allowable working pressure for pressure load conditions. The maximum stress theory of failure is used. Basically, the direct stresses in the circumferential and longitudinal directions are not allowed to exceed a maximum tensile stress value. In certain circumstances, e.g. where bending is prominent, the allowable stress is permitted to go to 1.5 times the maximum tensile stress.

Division 1 however does not provide for all kinds of geometries and loading, and can be impractical in certain situations. Unfortunately, this is the case with removable cover-plate headers. In such scenarios it is still necessary to determine adequacy, subject to the approval of an authorized inspector. Alternative means for analysis must therefore be identified.

2.1.2 Division 2 Part 5: design by analysis requirements

Division 2 provides alternative rules for the design and construction of pressure vessels. Part 5 in particular provides requirements for the method of design by analysis, whereby numerous failure criteria have to be satisfied, including plastic collapse, brittle fracture, buckling and fatigue amongst others. The finite element method may be employed, for which linear elastic, limit load and elastic-plastic analyses may be undertaken. The approach generally requires a higher level of engineering, because of the detail with which the geometry and loading are to be considered. Proper understanding of the method used for analysis is also a necessity.

Implementation of the linear elastic finite element method according to Part 5 requires stresses to be quantified via the method of linearization. Classification of these stresses is very important and can be challenging in certain scenarios. Each mode of failure also has a unique failure criterion. In the case of plastic collapse for example, the maximum octahedral shear stress (Von Mises equivalent) failure theory is used.

2.1.2.1 Stress classification

Stress classification is done according to the nature of the loads applied as well as the distribution and location of the stresses. Guidelines are provided in the code in tabular form, detailing example scenarios. Different allowable stress limits are applicable for the different stress categories. The stresses can be divided into three categories, as listed below.

1. ***Primary stress*** is produced by steady mechanical loads and excludes discontinuity stress or stress concentrations. Its main characteristic is that it is not self limiting. It can furthermore be divided into two subcategories, general and local.
    a. ***General primary stress*** is the result of the equilibration of internal and external mechanical forces. Any yielding will not cause a redistribution of stress, and can most likely be carried to failure. The stress may furthermore be evaluated as a composition of a membrane and a bending component. In the design by analysis approach these components are extracted via the linearization method, where a membrane component represents some averaged value of stress throughout the thickness, and a bending component represents an associated linear curve fit.
    b. ***Local primary stress*** is produced by design pressure or by other mechanical loads. It has a self-limiting characteristic, i.e. if the stress exceeds yield it gets redistributed and carried by other parts of the vessel. This typically occurs at structural discontinuities and the effect should diminish rapidly with distance from the discontinuity.
2. ***Secondary stress*** is characteristically self-limiting. Minor yielding is expected to reduce the relative intensity of the stress as it is most commonly attained at discontinuities or where thermal stresses are important.
3. ***Peak stress*** is the highest component of stress at some local point and is considered important for vessels in cyclic service as it has a significant influence upon failure through fatigue.

2.1.2.2 Linearization

The method of linearization makes use of the stress distribution along a path, denoted as a stress concentration line (SCL), which traverses the thickness of a part or component. Components of stress for the distribution are approximately represented by a uniform part (membrane stress) and a linear part (bending stress), by means of an integration technique. Consequently a full tensor of linearized stress quantities becomes available.

A few guidelines included in Division 2 of the code are repeated below. They illustrate what is accepted as being good practice for the accurate determination of linearized membrane and bending stresses. Figure 2-1 further eases the interpretation of these guidelines. It illustrates the three normal stress components relevant to a cylindrical vessel subjected to internal or external pressure. If it is not possible to comply with any of the stated criteria, the applicability of an SCL immediately becomes suspect. In such cases the code recommends following one of the more expensive techniques, e.g. limit load or elastic-plastic analyses.

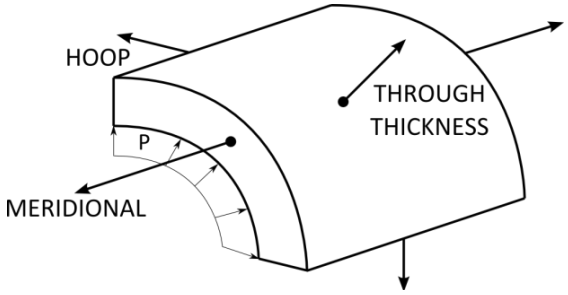

Figure 2-1: Quarter section of a cylindrical vessel subjected to internal pressure (P), showing the three normal stress components

1. SCLs should be oriented normal to contour lines of the stress component of highest magnitude. However, as this may be difficult to implement, similar accuracy can be obtained by orienting the SCL normal to the mid-surface of the cross section. SCL orientation guidelines are shown in Figure 2-2.
2. Hoop and meridional component stress distributions on the SCL should be monotonically increasing or decreasing, except for the effects of stress concentration or thermal peak stresses, see Figure 2-2 (b).
3. The distribution of the through-thickness stress should be monotonically increasing or decreasing. For pressure loading the through-thickness stress should be equal to the compressive pressure on the applied surface, and approximately zero on the other surface defining the SCL (see Figure 2-2 (c)). When the SCL is not perpendicular to the surfaces, this requirement will not be satisfied.
4. The shear stress distribution should be parabolic and/or the stress should be low relative to the hoop and meridional stresses. Depending on the type of loading, the shear stress should be approximately zero on both surfaces defined by the SCL. Guidelines are provided in Figure 2-2 (d).
    - The shear stress distribution along an SCL will approximate a parabolic distribution only when the inner and outer surfaces are parallel and the SCL is normal to the surfaces. If the surfaces are not parallel or an SCL is not normal to the surfaces, the appropriate shear distribution will not be obtained. However, if the magnitude of shear stress is small as compared to the hoop or meridional stresses, this orientation criterion can be waived.
    - When the shear stress distribution is approximately linear, the shear stress is likely to be significant.
5. For pressure boundary components, the hoop or meridional stresses typically are the largest magnitude component stresses and are the dominant terms in the equivalent stress. Typically the hoop or meridional stresses deviate from a monotonically increasing or decreasing trend along an SCL if the SCL is skewed with respect to the interior, exterior, or mid surfaces. For most pressure vessel applications, the hoop or meridional stresses due to pressure should be nearly linear.

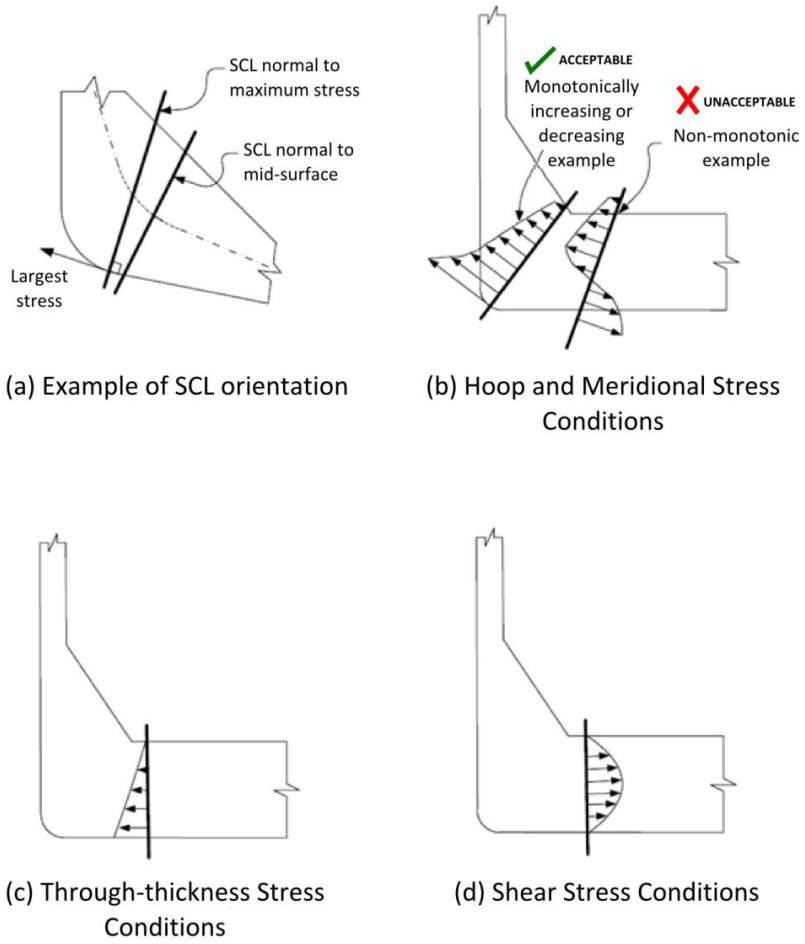

Figure 2-2: SCL orientation and validity guidelines (adapted from [5])

To summarize, the pivotal requirements for linearization involve the orientation of the corresponding SCL, as well as the distribution of the six stress components along its length. The SCL should preferably be oriented perpendicular to both the inside and outside surfaces, where the distributions of the stress components must be of a certain nature, including monotonically increasing or decreasing (hoop, meridional and torsion) and parabolic (shear components). Non-monotonic variation of stress is disallowed.

Available methods for linearization

As far as the actual linearization method is concerned, three alternatives are presented in annex 5.A of Division 2 [5]:

A. Stress Integration Method
B. Structural Stress Method Based on Nodal Forces
C. Structural Stress Method Based on Stress Integration

Method C is recommended as it is supposedly mesh insensitive. This method makes use of integration to linearize the through-thickness stress distribution, whilst only considering the

contributions of elements to one side of the SCL as depicted in Figure 2-3. Method B makes use of the contributions from the same elements, although the nodal forces are extracted, and is said to be equivalent to method C. However, in the case of method C each of the stress tensor components is linearized, whereas in the case of method B only those components oriented normal to the SCL are linearized. In a cylindrical shell this would translate to the hoop and meridional components of stress. Having only these quantities available makes it difficult to interpret certain failure criteria. For example, both plastic collapse and local failure require three principal stresses to evaluate, which implies the availability of a complete stress tensor.

The restriction posed by method B and C on the contributing set of elements further complicates matters, since it becomes quite difficult to implement for certain geometries. Arranging elements in the suggested form requires excellent control of the mesh, an aspect over which the capability of the modelling software at one's disposal has an important influence. As a result of the complications associated with methods B and C they were discarded. Only method A is considered.

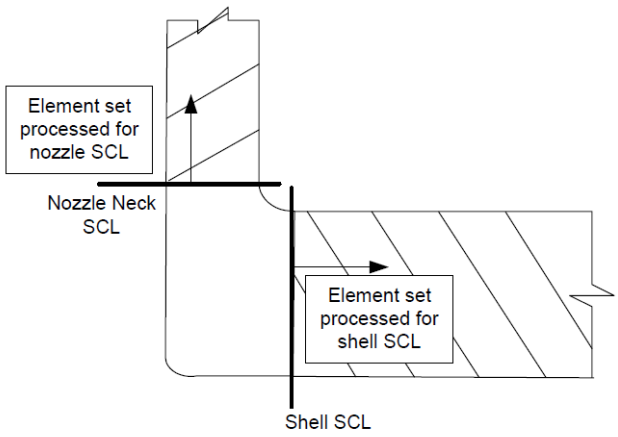

Figure 2-3: SCL processing for methods B and C [5]

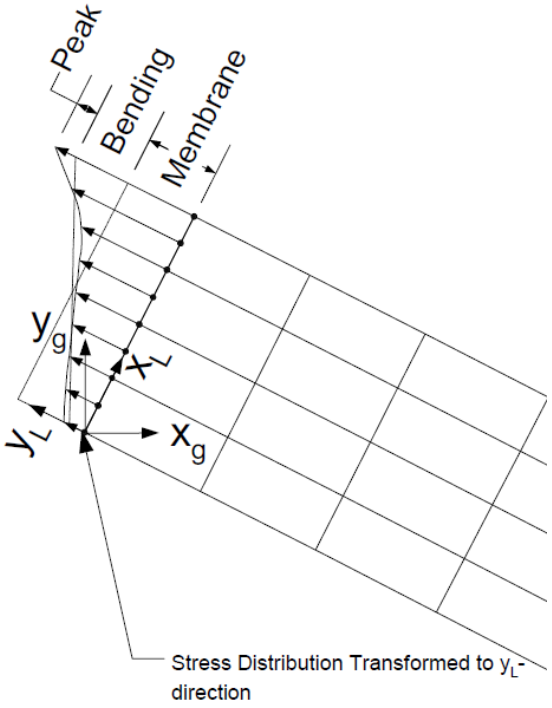

Figure 2-4: Typical linearized stress distribution [5]

Method A is performed in exactly the same manner as method C, except that all of the elements associated with the SCL have a contributing role. To illustrate the calculation of the membrane and bending stress tensors, the relevant formulae are shown in Equations (2-1) and (2-2).

I. **Membrane stress tensor.**

- The membrane stress tensor σ_{ij}^{m} is the tensor comprised of the average of each stress component σ_{ij} along the SCL, or:

$$\sigma_{ij}^{m} = \frac{1}{t}\int_{0}^{t}\sigma_{ij}dx \qquad \textbf{(2-1)}$$

where *t* denotes the thickness of the structural element under consideration.

II. **Bending stress tensor.**

- Bending stresses are calculated only for the local hoop and meridional (normal) component stress, and not for the local component stress parallel to the SCL or in-plane shear stress.
- The linear portion of shear stress needs to be considered only for shear stress distributions that result in torsion of the SCL.
- The bending stress tensor σ_{ij}^{b} is comprised of the linearly varying portion of each stress component σ_{ij} along the SCL, or:

$$\sigma_{ij}^{b} = \frac{6}{t^2}\int_0^t \sigma_{ij}\left(\frac{t}{2} - x\right)dx. \qquad \textbf{(2-2)}$$

It is further possible to calculate a collection of peak stresses which represent the difference between the actual and linearized stress components. This calculation has been omitted for the present study since peak stresses are typically used in fatigue calculations, which are not considered. Attention will however be given to the modes of plastic collapse and local failure. To quantify failure the linearized stress tensors are used to compute principal membrane, bending and combined stresses. These principal stresses (σ_1, σ_2, σ_3) are subsequently used to compute a scalar Von Mises equivalent stress quantity, S^e, defined as

$$S^e = \frac{1}{\sqrt{2}}\sqrt{\left(\sigma_1 - \sigma_2\right)^2 + \left(\sigma_2 - \sigma_3\right)^2 + \left(\sigma_3 - \sigma_1\right)^2}. \qquad \textbf{(2-3)}$$

2.1.2.3 Failure criteria

As a further guide to the use and application of linearization Hechmer & Hollinger [9] was used. This bulletin presents some guidelines for assessing stress results from three-dimensional finite element analyses in terms of the ASME boiler and pressure vessel code [5]. According to Hechmer & Hollinger [9] the failure modes that relate to membrane, bending, and membrane plus bending stresses are:

- ***General primary membrane equivalent stress (P_m):***
  - The principal failure mode is "collapse", in the sense that collapse includes *tensile instability* and *ductile rupture*.
- ***Primary bending equivalent stress (P_b):***
  - The failure modes for P_m also apply to P_b. The difference is that through-thickness yielding (shape factor effect) requires a stress higher than the yield, S_y, for collapse to occur.
- ***Local primary membrane equivalent stress (P_L) + Primary bending equivalent stress (P_b):***
  - The principal failure mode is excessive plastic deformation. However, it also relates to plastic instability due to the nature of P_b.
- ***Primary stresses (P) + Secondary equivalent stress (Q):***
  - The limit on $P + Q$ assures that the membrane plus bending stress will shake down to an elastic cycle. This is fundamental to assuring that the elastic fatigue analysis has

valid stresses even though they exceed twice the yield. It also precludes significant plastic strain ratchet.

In the ASME code [5], the following allowable limits are enforced in the case of a linear elastic finite element analysis. *S* denotes the maximum allowable stress value.

Evaluation of plastic collapse

$$P_m \leq S \quad \textbf{(2-4)}$$

$$P_L \leq 1.5S \quad \textbf{(2-5)}$$

$$\left(P_L + P_b\right) \leq 1.5S \quad \textbf{(2-6)}$$

Evaluation of local failure

$$\left(\sigma_1 + \sigma_2 + \sigma_3\right) \leq 4S \quad \textbf{(2-7)}$$

2.2 API standard 661

API 661 [1] is an international standard which gives requirements and recommendations for the design, materials, fabrication, inspection, testing and preparation for shipment of air-cooled heat exchangers, for use in the petroleum and natural gas industries. A few of the requirements and recommendations thought to be applicable to the present study are presented here.

General design requirements

The standard requires a purchaser to either specify or agree on the use of a pressure design code, such as the ASME code [5], for the design of any pressure component, which primarily involves the header box and tube bundle of an air-cooler assembly. Supplemental requirements are however provided in this standard. In respect of stress calculation the following combinations of load are considered important for header boxes and associated nozzles:

1. Stress caused by temperature and pressure;
2. Stress caused by nozzle forces and moments;
3. Stress caused by differential tube expansion between rows/passes in the coil sections (heating coils are used to protect the tube bundle against freeze-up).

The present study is primarily concerned with the effects of pressure loading and external nozzle loading. Stresses caused by temperature gradients and associated with the tube bundle are outside the scope of this study.

Irrespective of any design calculation results, limitations are also placed on minimum nominal thicknesses of header box components, as described in Table 2-1. A maximum corrosion allowance of 3 mm is specified in the case of a carbon or low-alloy steel.

Table 2-1: Minimum nominal thickness of header box components [1]

Component	Minimum thickness	
	Carbon or low-alloy steel	High-alloy steel or other material
Tube sheet	19 mm (3/4 in)	16 mm (5/8 in)
Plug sheet	19 mm (3/4 in)	16 mm (5/8 in)
Top, bottom and end plates	12 mm (1/2 in)	10 mm (3/8 in)
Removable cover-plates	25 mm (1 in)	22 mm (7/8 in)
Pass partition plates and stay plates	12 mm (1/2 in)	6 mm (1/4 in)
Note: The thickness indicated for any carbon or low-alloy steel component includes a corrosion allowance of up to 3 mm (1/8 in). The thickness indicated for any component of high-alloy steel or other material does not include a corrosion allowance. The thickness is based on an expanded tube-to-tube sheet joint with one groove.		

A further important requirement which specifically affects the cover-type header is that of minimum flange bolt spacing (bolt pitch). Depending on the nominal diameter of the bolts used, the following tabulated values are applicable (adapted from [1]):

Table 2-2: Minimum flange bolt spacing [1]

Nominal bolt diameter	Minimum bolt spacing
16 mm (5/8 in)	38 mm
19 mm (3/4 in)	44 mm
22 mm (7/8 in)	52 mm

A maximum flange bolt spacing value is calculated by means of the ASME code [5], and is illustrated in Chapter 4.

Nozzle requirements

Dimensions for acceptable nozzles, and the associated minimum nominal thickness of the nozzle neck are provided in Table 2-3 (adapted from [1]). A maximum corrosion allowance of 3 mm is once again applicable.

Maximum allowable moments and forces for nozzle attachments are stipulated in API 661 [1]. A nozzle is required to be capable of withstanding these loads in its design corroded condition. The header supporting structure is also to be designed so as to protect against damage from the simultaneous application of multiple nozzle loadings. The components of the nozzle loadings on a single header box shall not exceed the following values [1]:

$$M_x = 6\ 100\ \text{Nm}, \qquad F_x = 10\ 010\ \text{N},$$
$$M_y = 8\ 130\ \text{Nm}, \qquad F_y = 20\ 020\ \text{N},$$
$$M_z = 4\ 070\ \text{Nm}, \qquad F_z = 16\ 680\ \text{N}.$$

The coordinate system relating to these forces and moments is depicted in Figure 2-5. The maximum allowable nozzle loads for application to a single nozzle is furthermore included in Table 2-4. Each of the loads are interpreted to be implemented in either the positive or reversed orientation of the depicted coordinate system, and to be subject to a designer's interpretation. Selecting the correct

orientation for each of the loads presents a necessary task, since certain combinations may be of greater severity than others.

Table 2-3: Minimum nozzle neck nominal thickness (adapted from [1])

Nominal pipe size (NPS)	Pipe outer diameter	Nozzle neck thickness
2 in	60 .3 mm	8.74 mm
3 in	88.9 mm	11.13 mm
4 in	114.3 mm	13.49 mm
6 in	168.3 mm	10.97 mm
Note: The data in this table is taken from [10], using Schedule 160 for sizes up to NPS 4, and Schedule 80 for the larger sizes.		

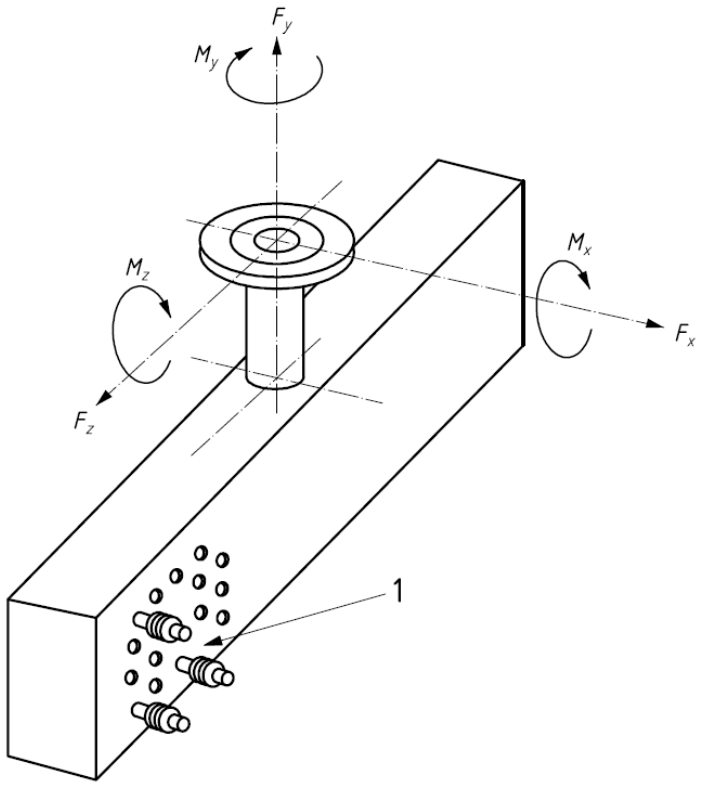

Key
1 fin tubes

Figure 2-5: Nozzle loads and orientation [1]

Table 2-4: Maximum allowable loads associated with nozzles of a certain size (adapted from [1])

Nozzle size (NPS)	Moments (*Nm*)			Forces (*N*)		
	M_x	M_y	M_z	F_x	F_y	F_z
2 in	150	240	150	1020	1330	1020
3 in	410	610	410	2000	1690	2000
4 in	810	1220	810	3340	2670	3340
6 in	2140	3050	1630	4000	5030	5030

3 Problem definition

A single representative removable cover-plate design is studied. The typical layout of such a design is shown in Figure 3-1.

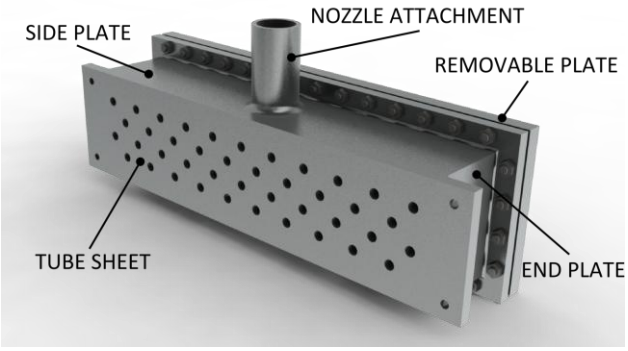

Figure 3-1: Illustration of a removable cover-plate header box

A detail drawing of the representative design is depicted in Figure 3-2, including annotations for the relevant dimensions. Specifications for this design are given in Table 3-1, including details for loading, material, and geometrical properties. In general, input to Optivessel [6] design software is arranged in a similar manner, where requirements are determined by an authorized design engineer.

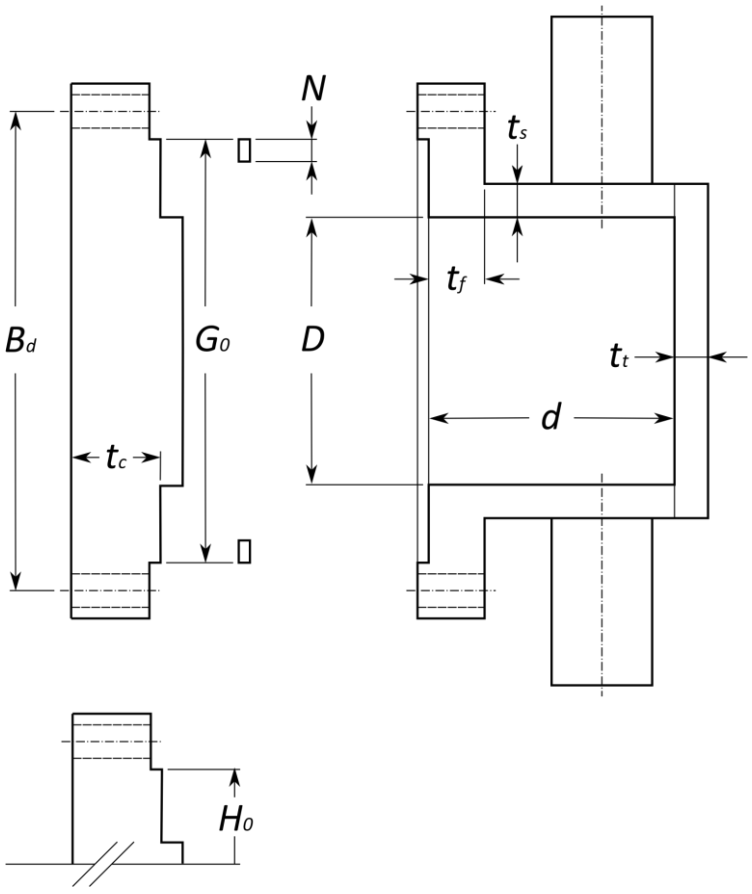

Figure 3-2: Detail schematic of header box

Table 3-1: Design specification of the representative removable cover-plate header box

Description	*Symbol*	*Value*	*Units*	*Additional detail*
Loading properties				
Design temperature	T	120.0	˚C	
Design pressure	P	1.0	MPa	
Material properties				
Wall material allowable stress at design temperature	S_{wd}	117.9	MPa	SA-516 Grade 60 N
Flange material allowable stress at design temperature	S_{fd}	117.9	MPa	SA-516 Grade 60 N
Cover material allowable stress at design temperature	S_{cd}	117.9	MPa	SA-516 Grade 60 N
Minimum recommended bolt stress at operating/design temperature	S_{ba}/S_{bd}	172.4	MPa	SA-193 B7
Dimensions and configuration properties				
Outer gasket width	G_0	328.0	mm	
Outer gasket length	H_0	1116.0	mm	
Internal tube sheet width	D	234.0	mm	
Header depth	d	220.0	mm	
Number of partition plates	N_{pp}	0	---	
Maximum span between partitions	M_{sp}	234.0	mm	
Distance between opposite bolts on short span	B_d	356.0	mm	
Gasket factor	m	2.0	---	
Gasket seating stress	y	17.24	MPa	
Corrosion allowance	C_a	3.0	Mm	
Corroded side plate thickness	t_s	27.0	mm	
Corroded end plate thickness	t_e	17.0	mm	
Corroded tube sheet plate thickness	t_t	27.0	mm	
Cover-plate thickness	t_c	45.0	mm	
Flange plate thickness	t_f	30.0	mm	
Major bolt diameter	d_b	19.05	mm	Major diameter
Minor bolt diameter	d_r	15.75	mm	Minor diameter
Bolt pitch used	p_b	80.0	mm	
Number of bolts	N_b	36	---	
Gasket width	N	15.0	mm	
Efficiencies				
Joint efficiency on welding	E_w	1.000	---	
Efficiency for nozzle opening (single nozzle on side plate)	E_n	0.500	---	Sch. 160 NPS 4 [10]
Tube sheet ligament efficiency	E_l	1.000	---	
End plate efficiency	E	1.000	---	

Table 3-2 provides details for the nozzle attachment. These were identified from ASME B36.10 M [10], and correspond with the 4" nozzle requirements specified by API 661 [1] (see Table 2-3).

Table 3-2: Nozzle design characteristics

Description	*Symbol*	*Value*	*Units*	*Additional detail*
Material properties				
Material allowable stress	S_{nd}	117.9	MPa	SA-516 Grade 60 N
Dimensions and configuration properties				
Non-corroded nozzle inside diameter	D_n	87.3	mm	
Non-corroded nozzle wall thickness	t_n	13.49	mm	
Nozzle length	L_n	200.00	mm	

In an effort to address the project objectives, this design is analyzed in a number of ways in this thesis. In Chapter 4, it is used to illustrate the current design practice. The process Optivessel [6] uses is thoroughly discussed, and results are presented. In Chapter 5 the design details are used to investigate rigid frame models as a means for developing an alternative design by rule method. Subsequently, in Chapter 6 a comprehensive finite element model of the design is developed. In all of these cases, a nozzle attachment is not considered. Only bolt pre-tension, and pressure loading are considered.

Bolt pre-tension is an important feature of the finite element model, since gasket seating must be represented appropriately. In Optivessel [6] bolt pre-tension is calculated based on a prescribed stress, the minor (smallest) diameter of the bolt, and ASME code [5] requirements. For adequate gasket seating in the finite element model of Chapter 6, the calculation was however changed to make use of the major bolt diameter. This is discussed in greater detail in Chapter 6, and is consistently implemented for all of the results presented in Chapter 7. In Chapter 7, results for Chapters 4 through 6 are compared with the following in mind:

1. The first intention is to establish how the methods in Chapters 4 and 5 compare to the finite element model, which is assumed to provide the most comprehensive solution.
2. The second intention is to perform design by analysis on the finite element model so as to draw comparisons with the design by rule results, for two reasons: firstly, to establish whether the design by rule method is comprehensive enough to consider all failure locations, and secondly to compare the level of conservatism of both design methods. Only the plastic collapse failure criterion is used.

Of the methods considered, finite element analysis presents the best option to establish the influence of the nozzle attachment. In Chapter 8, the nozzle attachment is included into the finite element model. The significance of the following is investigated by means of design by analysis:

1. Nozzle placement and external loading orientation.
2. Nozzle loading in comparison with operating pressure and bolt pre-tension.

Finally, a review of all the methods and scenarios is performed, and appropriate comparisons drawn.

4 Current design practice

In this chapter the design process used by Optivessel [6] is discussed in detail. All of the information was inferred from a header box design report made available to the author by I.F. Lombaard of SASTECH on June 4, 2010 [4].

4.1 Design process

The current design approach relies on the following key assumptions:

- The header box is represented as a collection of simply supported beams.
- Only bolt loading and internal pressure loading is considered.
- The bolt-induced bending moment is uniformly distributed throughout the header box structure.
- Under pressure loading a secondary bending moment acts to ensure the joint formed by the side plate and the tube sheet remains right-angled (i.e. rigid frame assumption).
- This secondary bending moment acts uniformly throughout the side plate.

4.1.1 Dimensions

Figure 4-1 shows the planar representation of the header box (see Figure 3-2), whereby the side plates, tube sheet and cover-plate are evaluated as simply supported beams.

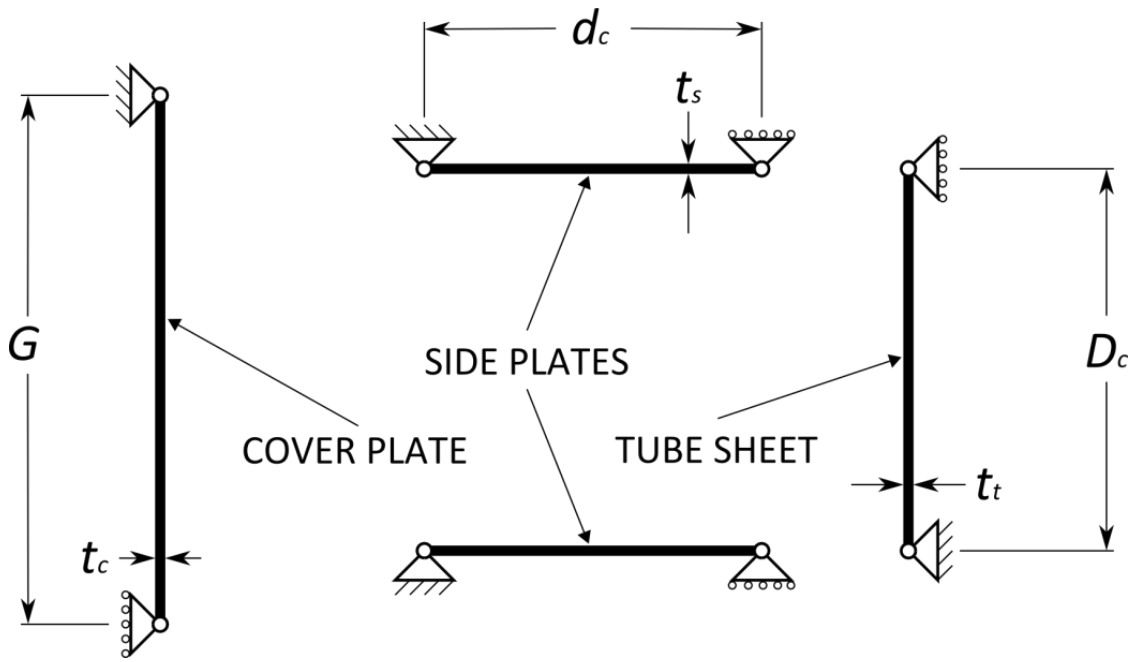

Figure 4-1: Segmented representation of header box by means of simply supported beams

In determining the dimensions shown, it is first and foremost necessary to calculate an effective gasket seating width, *b*. This is done in accordance with Mandatory Appendix 2 of ASME VIII Division 1 [5], which provides rules for bolted flange connections with ring type gaskets. These rules are

generally for pressure vessels of cylindrical form, but are adapted for use with the rectangular shape of the header box.

Specifically, in Table 2-5.2 of this Appendix provision is made for flanged joints in which the gasket is contained entirely within the inner edges of the bolt holes. The calculation of b is illustrated by Equations (4-1) through (4-3). The basic gasket seating width b_0 is given by

$$b_0 = \frac{N}{2}, \tag{4-1}$$

where N is the gasket width, and the effective gasket seating width (b) is then calculated from

$$b = b_0, \text{ when } b_0 \leq 6 \text{ mm}; \tag{4-2}$$

$$b = 0.5 C_{ul} \sqrt{\frac{b_0}{C_{ul}}}, \text{ where } C_{ul} = 25.4 \text{ (conversion for metric units), when } b_0 > 6 \text{ mm}. \tag{4-3}$$

Two of the dimensions applicable to the cover-plate, G_0 and H_0, are adjusted for further calculations by means of this effective gasket seating width. The recalculated dimensions are:

$$G = G_0 - 2b, \text{ and} \tag{4-4}$$

$$H = H_0 - 2b. \tag{4-5}$$

Two of the dimensions associated with the header box bonnet, D and d, are simply adjusted for corrosion allowance, as follows:

$$D_c = D + 2C_a \text{ (internal tube sheet width);} \tag{4-6}$$

$$d_c = d + 2C_a \text{ (header depth).} \tag{4-7}$$

The remaining dimensions (t_c, t_s, t_t) are defined in Table 3-1. They correspond to the thicknesses of the cover-plate, side plates and tube sheet.

4.1.2 Free body diagrams

A free body diagram for the scenario of bolt loading (i.e. pre-tension) is illustrated in Figure 4-2. Since the bolts are positioned at an offset to the gasket they cause a bending moment.

Two independent bending moments are calculated so as to perform stress calculations for the flange (M_{jf}) and header walls (M_{jw}), which include the cover-plate, side plate, and tube sheet. These bending moments are interpreted to arise from a tensile bolt force acting over distinct lever arms. In Figure 4-3 the lever arms are represented by h_1 and h respectively, calculated as follows:

$$h_1 = \frac{B_d - (D + 2t_s + 2C_a)}{2}; \quad \textbf{(4-8)}$$

$h = \frac{B_d - G}{2}$, where B_d is the distance between opposite bolts on the short span. **(4-9)**

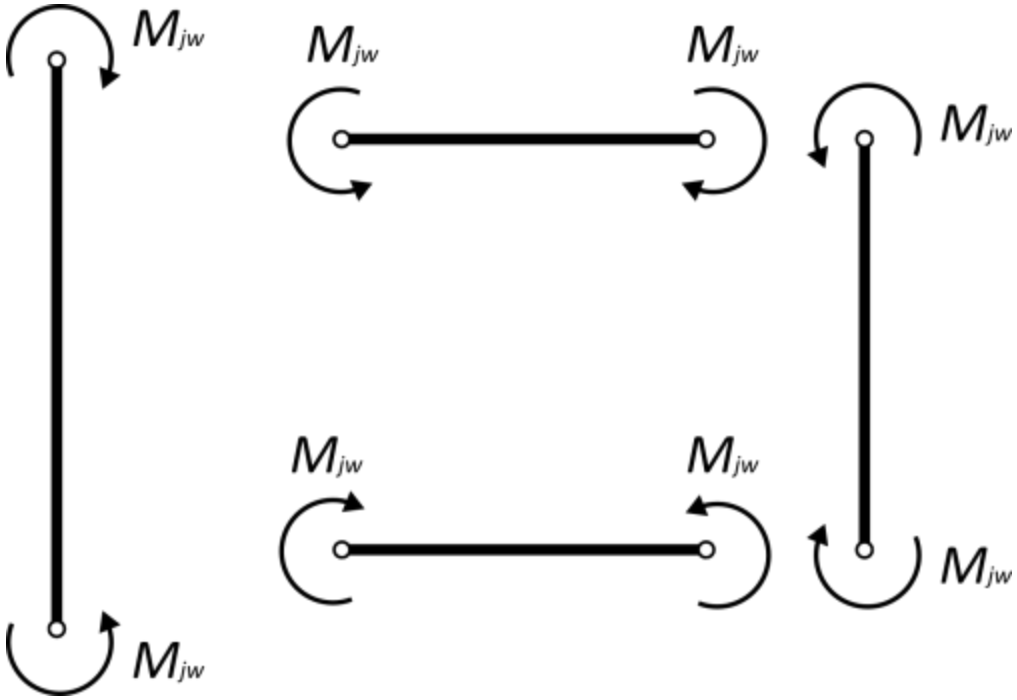

Figure 4-2: Bolt loading diagram for header box

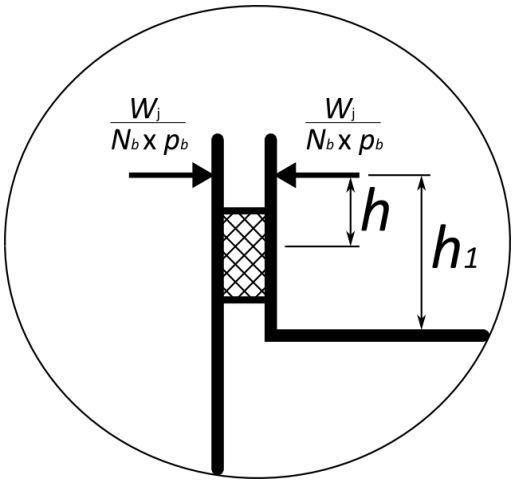

Figure 4-3: Illustration of the lever arms used in the calculation of the bolt induced bending moments

A further free body diagram of the pressure loading scenario is depicted in Figure 4-4. Essentially, the cover-plate, side plate and tube sheet are represented by simply supported beams carrying a uniformly distributed load (pressure). Additionally, the joint formed by the side plate and tube sheet is accepted as remaining right-angled, hence the bending moment M_1. The implementation of this moment will be discussed in particular detail in the section to follow.

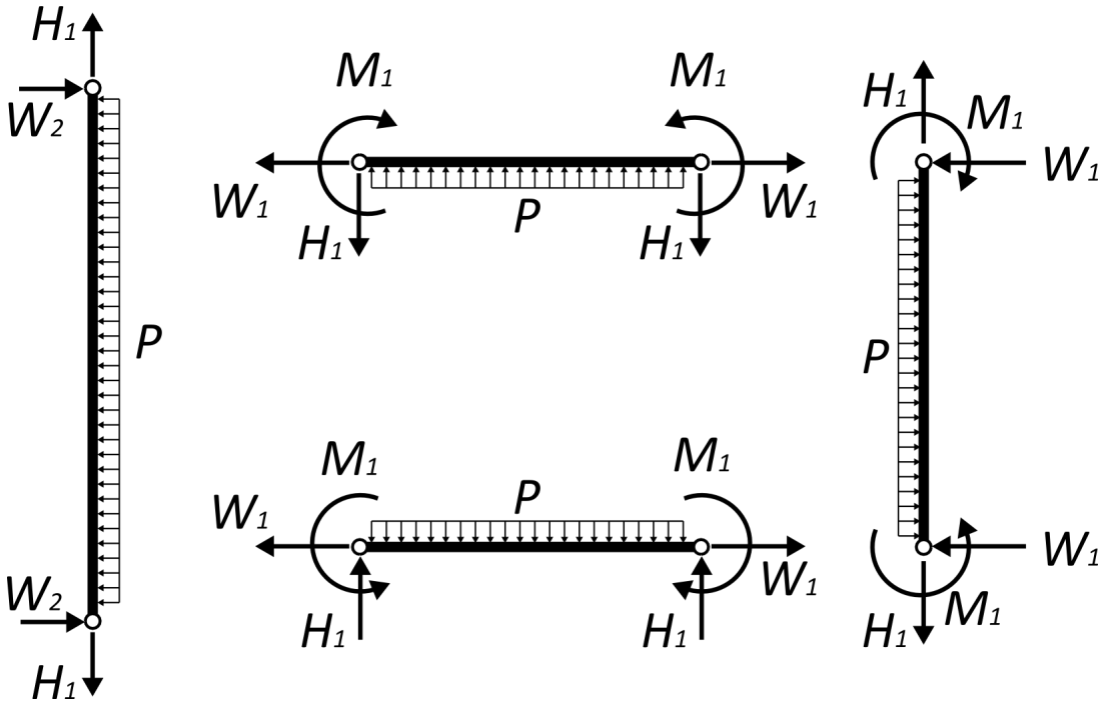

Figure 4-4: Pressure loading diagram for header box

4.1.3 Calculation of forces and moments related to bolt loading

Bolts are evaluated as though they are only capable of resisting tensile load, i.e. no bending moment is resisted. In accordance with Mandatory Appendix 2 (ASME [5]), a minimum required bolt load for operating conditions (W_{m1}) and gasket seating is calculated (W_{m2}). These two results are used to determine whether an adequate number of bolts have been selected at an appropriate bolt pitch. Once this has been established, the ultimate arrangement of bolts is used to calculate a total bolt load (W_j), which is used for the calculation of the bending moments, M_{jf} and M_{jw}, and subsequent stress calculations.

The required bolt load for operating conditions (W_{m1}) should be sufficient to resist the hydrostatic end force exerted by the maximum allowable working pressure on the area bounded by the gasket reaction, and in addition, to maintain on the gasket or joint-contact surface a compression load, which experience has shown to assure a tight joint. This compression load is expressed as a multiple m (see Table 3-1) of the internal pressure. Equation (4-10), adapted from [5], shows the calculation of W_{m1}.

$$\begin{aligned} W_{m1} &= P \times (\text{Area bounded by gasket reaction}) + 2mP \times (\text{Gasket contact surface}) \\ &= P \times (G \times H) + 2mP \times \left[\left(2 \times (G + H) + H \times N_{pp} \right) \times b \right] \end{aligned} \quad \textbf{(4-10)}$$

A gasket must be seated properly by applying an initial load through pre-tightening of the bolts. This is done without the presence of internal pressure, and is a function of the gasket material and the effective gasket area to be seated (adapted from [5]). Equation (4-11) illustrates an expression for the minimum initial bolt load (W_{m2}) for this purpose.

$$W_{m2} = y \times (\text{Gasket contact surface}) = y \times \left[\left(2 \times (G + H) + H \times N_{pp} \right) \times b \right] \quad \textbf{(4-11)}$$

where y is the gasket seating stress. The computed bolt loads, W_{m1} and W_{m2}, are now used to compute minimum required bolt areas, A_{m1} and A_{m2}, to comply with the prescribed bolt stress. The greater of these areas (defined as A_m) is used to evaluate the actual total cross-sectional area of the bolts (A_b) for adequacy (i.e. A_b must not be less than A_m).

$$A_{m1} = \frac{W_{m1}}{S_{bd}}, \text{ where } S_{bd} \text{ is the minimum bolt stress at design temperature.} \quad \textbf{(4-12)}$$

$$A_{m2} = \frac{W_{m2}}{S_{ba}}, \text{ where } S_{ba} \text{ is the minimum bolt stress at operating temperature.} \quad \textbf{(4-13)}$$

$$A_m = \max(A_{m1}, A_{m2}) \quad \textbf{(4-14)}$$

$$A_b = N_b \times \frac{\pi}{4} d_r^2 \ (N_b = \text{number of bolts; } d_r = \text{minor bolt diameter}) \geq A_m \quad \textbf{(4-15)}$$

In addition to the minimum area requirement, the spacing of the bolts also needs to be verified. To this end a maximum bolt pitch ($p_{b,\max}$) is calculated according to the TEMA standard [11]. The maximum bolt pitch is defined as a function of the major bolt diameter (d_b), flange thickness (t_f) and gasket factor (m):

$$p_{b,\max} = \left(2 \times d_b\right) + \left(\frac{\left(6 \times t_f\right)}{m + 0.5} \right) \quad \textbf{(4-16)}$$

API 661 [1] provides a minimum bolt pitch ($p_{b,\min}$) based on bolt size (see Table 2-2). The selected bolt pitch (p_b) is required to fall within $p_{b,\min}$ and $p_{b,\max}$.

Once a bolt arrangement is found which meets the requirements of spacing and minimum cross-sectional area, a total bolt load (W_j) can be calculated for the purposes of design. The ASME code [5] also distinguishes between the scenarios of operating conditions (Equation (4-17)) and gasket seating (Equation (4-18)) in this respect.

$$W_j = W_{m1} \quad \textbf{(4-17)}$$

$$W_j = \frac{S_{ba} \times (A_m + A_b)}{2} \ (A_m = \text{minimum required bolt area; } A_b = \text{total bolt area}) \quad \textbf{(4-18)}$$

In the case of operating conditions, the total bolt loading corresponds to the minimum required to assure a tight joint. For gasket seating on the other hand the total bolt load includes a margin against abuse of the flange from over-bolting [5]. Since the bolts are pre-tensioned at atmospheric temperature and before application of internal pressure, the flange design is required to satisfy this

loading only under such conditions. However, if additional safety against abuse is desired, or where it is necessary that the flange be suitable to withstand the full available bolt load, the following equation may be used in lieu of Equation (4-18):

$$W_j = S_{ba} \times A_b. \quad \textbf{(4-19)}$$

In current design practice, only Equation (4-18) is considered. It is used in the calculation of the bending moments M_{jf} (moment due to bolt load on header flange only) and M_{jw} (moment due to bolt load on header walls) resulting from the bolts being placed at an offset to the gasket. These moments are calculated from

$$M_{jf} = \frac{W_j \times h_1}{N_b \times p_b}, \text{ and} \quad \textbf{(4-20)}$$

$$M_{jw} = \frac{W_j \times h}{N_b \times p_b} \ (N_b = \text{number of bolts; } p_b = \text{bolt pitch used}). \quad \textbf{(4-21)}$$

The moment acting upon all of the walls results from assuming the tensile force of the bolts to cause a couple in conjunction with reaction forces at the gasket interface. The moment acting on the flange only is equivalent to having the flange built in (fixed) at the joint with the side plates. Note that since beam calculations are being performed, forces and moments are also evaluated on a per unit depth basis.

The results for Equations (4-18), (4-20) and (4-21) are used in a number of further calculations relating to stresses associated with the flange and planar representation of the header box. In this implementation, the stresses resulting from pressure loading are superimposed on those resulting from gasket seating.

Certainly, Equation (4-19) would present a more conservative option in terms of total bolt load. It is used to draw appropriate comparisons with finite element model results in Chapter 7. For the bolt material SA-193 B7 pre-loading is required to fall within a recommended minimum (172.4 MPa) to maximum (413.7 MPa) stress range [12]. The minimum in this instance corresponds to the prescribed value used in design practice. Since the bolts can be expected to be pre-tightened to this value during operation it is only appropriate for it to be dealt with as such.

4.1.4 Calculation of forces and moments related to pressure loading

In view of the free body diagram presented in Figure 4-4, three reaction forces have to be calculated (H_1, W_1, W_2). These forces correspond to the support reactions of a simply supported beam subject to a uniformly distributed load, in this case pressure. On a per unit depth basis, they may therefore be calculated as follows:

$$H_1 = \frac{P \times d_c}{2}; \quad \textbf{(4-22)}$$

$$W_1 = \frac{P \times D_c}{2}; \tag{4-23}$$

$$W_2 = \frac{P \times G}{2}. \tag{4-24}$$

Typically, stresses are computed at the centre and ends of the tube sheet and side plate, whilst only at the centre for the cover-plate. This is sufficient, due to the symmetry of the assumed loading distribution for each of the beam segments. The bending moment at the centre of such a beam configuration may be solved easily as depicted below (see Equation (4-25)).

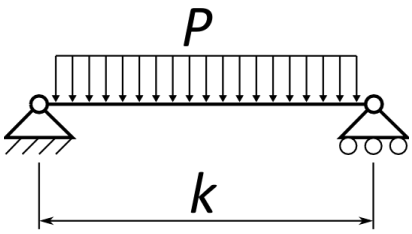

Figure 4-5: Simply supported beam subject to distributed load

$$M = (\frac{Pk}{2} \times \frac{k}{2}) - (\frac{Pk}{2} \times \frac{k}{4}) = \frac{Pk^2}{8} \tag{4-25}$$

Subsequently the bending moments at the centre of the cover-plate (M_{p2}), side plate (M_{p4}) and tube sheet (M_{p8}) may be expressed on a per unit depth basis as follows:

$$M_{p2} = \frac{P \times G^2}{8}; \tag{4-26}$$

$$M_{p4} = \frac{P \times d_c^{\,2}}{8}; \tag{4-27}$$

$$M_{p8} = \frac{P \times D_c^{\,2}}{8}. \tag{4-28}$$

A final bending moment is calculated in M_1. It is evaluated at the joint formed between a side plate and the tube sheet, and is intended to take account of interaction between the plates. To this end, we approximate the corner joint as being rigid, where rotation of both the side plate and tube sheet at the supported points must be equal. The secondary bending moment M_1 enforces this rigidity, as pressure alone on the plates cause a discrepancy in rotation at this point.

In this instance we make use of the angular rotation resulting at either end of a simply supported beam due to an enforced bending moment at either or both ends with consideration of a superimposed uniformly distributed load. The beam equations considered are illustrated in Figure 4-6, whereupon the derivation for M_1 follows.

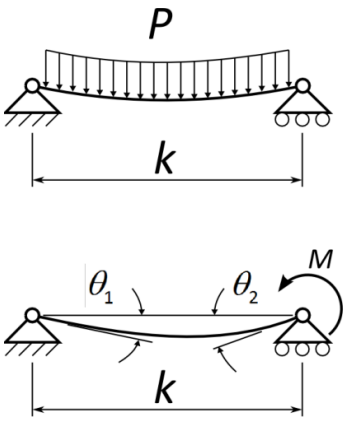

Figure 4-6: Equations used for junction moment

$$\theta_{\text{tube sheet}} = \theta_{\text{side plate}}$$

$$\frac{P \times D_c^{\,3}}{24EI_t} - \frac{M_1 \times D_c}{6EI_t} - \frac{M_1 \times D_c}{3EI_t} = \frac{M_1 \times d_c}{3EI_s} - \frac{P \times d_c^{\,3}}{24EI_s}$$

$$\frac{P \times D_c^{\,3}}{24EI_t} - \frac{M_1 \times D_c}{2EI_t} = \frac{M_1 \times d_c}{3EI_s} - \frac{P \times d_c^{\,3}}{24EI_s}$$

It subsequently follows that:

$$M_1 = \frac{P}{24} \times \frac{D_c^{\,3} / I_t + d_c^{\,3} / I_s}{D_c / 2I_t + d_c / 3I_s}. \qquad \textbf{(4-29)}$$

The second moment of area of the side plate (I_s) and tube sheet (I_t) may be computed by means of Equations (4-30) and (4-31) on a unit depth basis.

$$I_s = \frac{t_s^{\,3}}{12} \qquad \textbf{(4-30)}$$

$$I_t = \frac{t_t^{\,3}}{12} \qquad \textbf{(4-31)}$$

The moment at the junction is derived so as to only be applied at the corner joint for the side plate. However, for the calculations of current practice, this moment is effectively assumed to act uniformly throughout the side plate's beam element representation. This can be observed in Figure 4-4, and is equivalent to evaluating the side plate as a cantilever beam fixed at the flange junction, with M_1 applied at the free end.

4.1.5 Calculation of stresses

Enough information is now available to evaluate the stress at critical points within the structure for comparison to prescribed allowable values. The allowable values with which comparisons are struck include that of shear, membrane and bending stresses, as well as combinations.

Header flange:

In the flange section only a shear stress (S_s) and a bending stress (S_b) is evaluated, both of which result solely from bolt loading. A combined stress (S_c) value is subsequently computed which effectively corresponds to a Tresca stress value. Expressions for these values and their allowable limits are provided in Equations (4-32) through (4-34).

$$S_s = \frac{W_j}{p_b \times N_b \times t_f \times E_w} < \frac{S_{fd}}{2} \tag{4-32}$$

$$S_b = \frac{6M_{jf}}{t_f^{\,2} \times E_w} < 1.5 \times S_{fd} \tag{4-33}$$

$$S_c = \sqrt{(2 \times S_s)^2 + S_b^{\,2}} < 1.5 \times S_{fd} \tag{4-34}$$

Cover-plate:

In the cover-plate section we compute a membrane and bending stress, as well as a combined stress which is simply the sum of the two. Calculations are furthermore based on a selected width of the cover-plate (M_{inC}).

$$S_m = \frac{H_1}{M_{inC}} < S_{cd} \tag{4-35}$$

$$S_b = \frac{6 \times (M_{jw} + M_{p2})}{M_{inC}^{\,2}} < 1.5 \times S_{cd} \tag{4-36}$$

$$S_c = S_m + S_b < 1.5 \times S_c \tag{4-37}$$

Side plate:

For the side plate we evaluate a membrane stress as well as two bending stresses. The first bending stress (S_{b4}) is located at the centre of the side plate, and the further bending stress (S_{b5}) is located at either end of the plate. A further maximum combined stress is computed as per usual.

$$S_m = \frac{W_1}{t_s \times E_n} < S_{wd} \tag{4-38}$$

$$S_{b4} = \frac{6 \times (M_{p4} - M_1 + M_{jw})}{t_s^{\,2} \times E_n} < 1.5 \times S_{wd} \tag{4-39}$$

$$S_{b5} = \frac{6 \times \left(M_{jw} - M_1 \right)}{t_s^{\,2} \times E_w} < 1.5 \times S_{wd} \tag{4-40}$$

$$S_c = S_m + \max\left(S_{b4}, S_{b5} \right) < 1.5 \times S_{wd} \tag{4-41}$$

Tube sheet:

The tube sheet is analyzed in an analogous manner to the side plate, where S_{b7} corresponds to the bending stress at the centre of the plate and S_{b6} to the bending stress at a junction with the side plate.

$$S_m = \frac{H_1}{t_t \times E_l} < S_{wd} \tag{4-42}$$

$$S_{b6} = \frac{6 \times \left(M_{jw} - M_1 \right)}{t_t^{\,2} \times E_w} < 1.5 \times S_{wd} \tag{4-43}$$

$$S_{b7} = \frac{6 \times \left(M_{jw} + M_{p8} - M_1 \right)}{t_t^{\,2}} < 1.5 \times S_{wd} \tag{4-44}$$

$$S_c = S_m + \max\left(S_{b6}, S_{b7} \right) < 1.5 \times S_{wd} \tag{4-45}$$

If perforations were to be included, the calculations are slightly different. In that case the ligament efficiency (E_l) is not zero. It may in general be calculated in accordance with the ASME code [5] as follows:

$$E_l = \frac{p - d}{p}, \tag{4-46}$$

where

d = average diameter of the same two adjacent openings;

p = centre-to-centre spacing of two adjacent openings.

In current practice, a further bending moment (M_{px}) is calculated at the most centre tube row, and used for a bending stress calculation (S_{b8}) incorporating the ligament efficiency.

$$M_{px} = \frac{P \times X \times \left(D_c - X \right)}{2}, \tag{4-47}$$

where

X = distance from side plate to most centre tube row.

$$S_{b8} = \frac{6 \times \left(M_{jw} + M_{p8} - M_1 \right)}{t_t^{\,2} \times E_l} < 1.5 \times S_{wd} \tag{4-48}$$

Subsequently, Equation (4-45) may be modified as follows:

$$S_c = S_m + \max\left(S_{b6}, S_{b7}, S_{b8} \right) < 1.5 \times S_{wd}. \tag{4-49}$$

4.1.6 Requirements for the end plate thickness

In UG-34, Section VIII Division 1, of the ASME code [5] requirements are given for the minimum thickness of unstayed flat heads, cover-plates and blind flanges. For flat unstayed heads, covers, or blind flanges of square, rectangular, elliptical, obround, segmental, or otherwise noncircular shape the required thickness (t_e) is to be calculated by the following formula:

$$t_e = d\sqrt{\frac{ZCP}{SE}}, \tag{4-50}$$

where

$$Z = \max\left(2.5; 3.4 - \frac{2.4d}{D} \right), \tag{4-51}$$

with the limitation that Z need not be greater than two and one-half (2.5). The symbols used are defined as follows:

C	=	a factor depending upon the method of attachment of head, shell dimensions, and other items listed in the ASME code [5];
d	=	short span of the flat head or cover;
D	=	long span of the flat head or cover measured perpendicular to short span;
E	=	joint efficiency relating to the weld, specified in the ASME code [5];
P	=	internal design pressure
S	=	maximum allowable stress;
Z	=	a factor of noncircular heads or covers that depends on the ratio of short span to long span, and is dimensionless.

Equation (4-50) provides for safe construction as far as stress is concerned when used diligently. According to the ASME code [5] it is not to be used in instances where noncircular heads, covers or blind flanges are attached by bolts causing a bolt edge moment. The code [5] does provide an equation in this respect suited to cases where bolted joints are included around the circumference of the head/cover. The end plates of a removable cover-plate header box however represent a special case, where a single side of the rectangular plate is joined by means of bolts. Since the bolts are positioned at an offset to the gasket, a bolt edge moment is a factor.

In current practice, Equation (4-50) and (4-51) are used for the end plates with inclusion of a corrosion allowance (C_a). This is illustrated in Equation (4-52).

$$t_e = d\sqrt{\frac{ZCP}{SE}} + C_a \tag{4-52}$$

The value for C is typically identified as 0.2 from Mandatory Appendix 13 of the code [5], which provides for vessels of noncircular cross section. This value is specified for all cases dealt with by the Appendix, which does not include the removable cover-plate header box. The shoulder-plug type header box is for example included.

To consider partition plates, the short span (d) and long span (D) are adjusted. Partition plates are assumed to provide ideal support. If a single partition plate were for example to be placed midway along the long span (traversing the tube sheet), this span would be halved. The short span and long span would then have to be rearranged accordingly.

4.1.7 Requirements for the nozzle wall thickness

In UG-27, Section VIII Division 1, of the ASME code [5] requirements are given for the minimum thickness of shells under internal pressure. Using these requirements, current practice evaluates a nozzle attachment as a cylindrical shell for which circumferential and longitudinal stress calculations are performed (see Equation (4-53) and (4-54)). The equations provided in the ASME code [5] are simply modified to include a corrosion allowance.

Circumferential stress:

$$t_n = \frac{PR}{SE_w - 0.6P} + C_a \tag{4-53}$$

Longitudinal stress:

$$t_n = \frac{PR}{2SE_w + 0.4P} + C_a, \tag{4-54}$$

where

E_w = joint efficiency for, or the efficiency of, appropriate joint in cylindrical shell;
P = internal design pressure;
R = inside radius of the shell under consideration;
S = maximum allowable stress value.

The greater of Equation (4-53), (4-54) and requirements presented in API 661 [1] (see Table 2-3) are used to determine the minimum thickness of a nozzle attachment. Generally, the minimum requirement presented in API [1] dictates the result.

4.2 Results

Results are shown for all stress calculations presented in Chapter 4.1.5 associated with the representative header box design in Table 4-1. All of the results may be observed to meet the maximum allowable requirements.

In Table 4-2 results for the thickness calculations presented in Chapter 4.1.6 and 4.1.7 are presented. In this case, the requirements are once again met.

Table 4-1: Current practice stress results for representative header box

Quantity	*Result (MPa)*	*Allowable (MPa)*	*Equation number*	*Comments*
Header flange				
S_s	9.45	58.95	(4-32)	Acceptable
S_b	58.61	176.85	(4-33)	Acceptable
S_c	61.58	176.85	(4-34)	Acceptable
Cover-plate				
S_m	2.48	117.90	(4-35)	Acceptable
S_b	54.13	176.85	(4-36)	Acceptable
S_c	56.60	176.85	(4-37)	Acceptable
Side plate				
S_m	8.89	117.90	(4-38)	Acceptable
S_{b4}	111.96	176.85	(4-39)	Acceptable
S_{b5}	4.82	176.85	(4-40)	Acceptable
S_c	120.85	176.85	(4-41)	Acceptable
Tube sheet				
S_m	4.13	117.90	(4-42)	Acceptable
S_{b6}	4.82	176.85	(4-43)	Acceptable
S_{b7}	64.08	176.85	(4-44)	Acceptable
S_c	68.21	176.85	(4-45)	Acceptable

Table 4-2: Current practice results for minimum thickness calculations of the header box end plate and nozzle wall

Quantity	*Minimum thickness (mm)*	*Actual thickness (mm)*	*Equation number*	*Comments*
End plate				
t_e	12.93	20.00	(4-52)	Acceptable
Nozzle wall				
t_n (Circumferential)	3.40	13.49	(4-53)	Acceptable
t_n (Longitudinal)	3.20	13.49	(4-54)	Acceptable

4.3 Discussion

The results suggest that the most critical location on the header is at the centre of the side plate. At this location the bending and combined stresses are of the greatest magnitude, where the peak combined stress value is approximately 70 % of the maximum allowable. The membrane stress is of little significance in all of the cases, resulting from pressure induced loading.

4.3.1 Distribution of stress along the side plate and tube sheet

The nature of the assumptions made in current practice dictate the distribution of stress in the side plate and tube sheet. Firstly, the calculated bending moment resulting from the bolt loading is assumed to act throughout the walls of the bonnet (i.e. side plates and tube sheet). Secondly, the bending moment M_1 resulting from the deformation of the corner joint (connection between side plate and tube sheet) for pressure loading is used in the calculation of the bending stress at the centre of the plates as well as the ends. Finally, pressure loading is considered independently for each of the plates as depicted in Figure 4-4. Figure 4-7 illustrates the superposition of these influencing factors with relevance to the side plates and tube sheet.

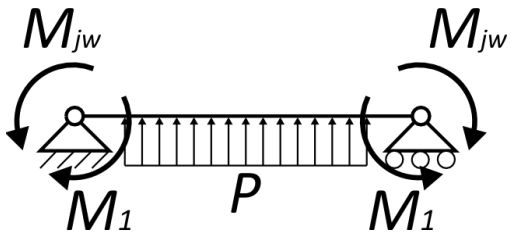

Figure 4-7: Load application in analysis of a header wall

Using the deduced loading scenario depicted in Figure 4-7, the stress distributions along the length of the side plate and tube sheet were evaluated, and are depicted in Figure 4-8. Note that the nozzle efficiency (E_n) is considered separately since it is used to predict a value mid-span only.

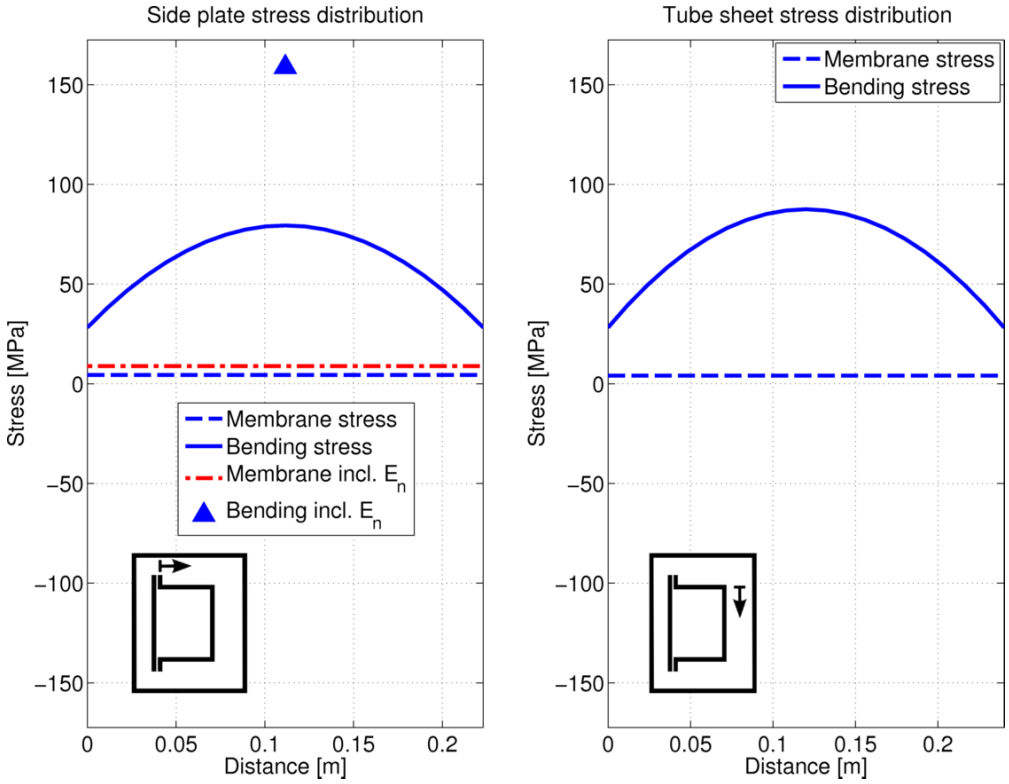

Figure 4-8: Stress distribution for current practice assumptions

The layout of Figure 4-8 is used throughout the thesis. In this layout, images are superimposed on the plots which depict the side-on perspective of the header box. An arrow in these images is

intended to convey the location of the corresponding stress distribution to the reader. Results for alternative analytical solutions (Chapter 5) as well as FEA (Chapter6) will be presented and compared in this arrangement.

4.3.2 Interpretation of the nozzle efficiency factor (E_n) for stress in the side plate

Efficiency factors are also incorporated to add an extra margin of safety. A calculated membrane or bending stress is simply divided by such a factor, representing a value between zero and one. In most cases all of the junctions are provided with efficiency factors of one (i.e. no extra margin is included).

The most significant factor is the effect of the nozzle positioned on the side plate. The weakening effect may be analogized to the stress concentration in a flat plate with a hole positioned at its centre, subject to either bending or tensile load. In current design practice, the norm is to simply select a nozzle efficiency of fifty percent, equivalent to a stress concentration factor of two. It would however be beneficial if this factor could also provide a margin of safety against the nozzle loading requirements presented in API 661 [1]. SASOL in particular, contracts third party mechanical design companies to perform finite element analysis to address nozzle loading [4].

Consider Figures 4-9 and 4-10 which illustrate the mentioned stress concentration effect. From the graphs presented, the influencing factors on the stress concentration can be determined as the depth of the header box, the size of the nozzle hole and the thickness of the side plate. This is valid for the assumptions surrounding the current beam design formulation taking the nature of the load application into account.

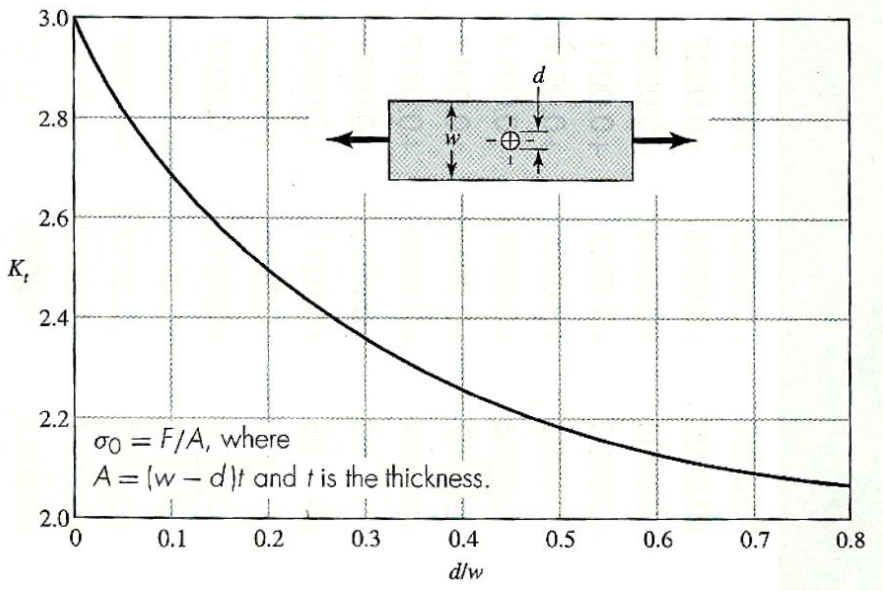

Figure 4-9: Tensile load stress concentration (adapted from [13])

The same stress concentration factor is used both in the case of the membrane and bending stresses. Seeing as the depth of a header box (*w* in this case) can vary greatly with respect to the diameter (*d*) of a nozzle, it is conceivable that the tensile stress concentration could vary anywhere

upwards from two to three. This would suggest that for the current practice assumptions it would be non-conservative in the case of the side plate membrane stress (S_m) to only make use of a stress concentration factor of two. The membrane stress is however quite small in relation to the bending stress. It could therefore be argued that this influence is of little importance.

The bending stress concentration factor is presented in Figure 4-10. For current designs, the ratio of nozzle diameter to plate thickness is often quite high and can be expected to fall in the range between two and infinity. In certain cases lower ratios are however still possible. Nozzles typically range in size from two inches to six inches. For the suggested range between two and infinity (ratio of nozzle diameter to plate thickness) a stress concentration of two more or less represents an upper bound.

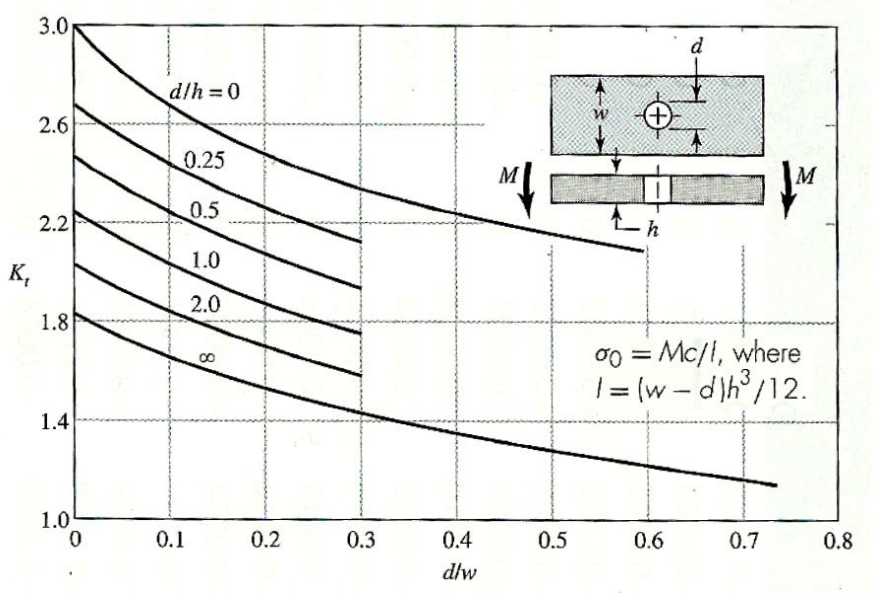

Figure 4-10: Bending load stress concentration (adapted from [13])

In both the cases of the tensile and bending stress calculation it is however necessary to adjust the depth of the plate with the nozzle hole diameter, which is not carried out in current practice since unit depth beam formulations are used. Such an implementation would suggest that the depth of the header is assumed to be large, in which case the nozzle diameter has a negligible effect. In the case of tensile loading the stress concentration factor would approach a value of three for this assumption. Further, in the case of bending load, for the greatest level of conservatism (very low nozzle diameter to plate thickness ratio), a stress concentration of three would also be approximated.

Considering the above arguments, the assumed stress concentration factor of two cannot be validated under all circumstances. It is most applicable in instances where the nozzle diameter is much larger than the plate thickness under bending load, as was illustrated by the upper bound argument. It is furthermore important to keep in mind that its application relies on the assumptions made to compute the stress in the first place.

4.4 Final remarks

In this example design, perforations on the tube sheet as well as pass partition plates are discarded. These two factors complicate analysis, and were placed outside of the scope of the present study. Current design practice in any case largely neglects these influences. Intuitively, a pass partition plate is expected to provide a strengthening effect, whereas perforations effectively reduce the stiffness of the tube sheet. These two may be implemented in a great variety of ways. The pass partition plate may be positioned at any location along the height of the tube sheet, and a pressure difference may exist on either side of it. Negating the use of a pass partition plate is representative of a return header. Nozzles are still positioned on such designs to serve as a drain or vent.

Further, a number of different tube patterns may be used at various pitch and size configurations. A method for taking account of the weakening effect is presented in the ASME code [5], whereby the plate is effectively modelled as having a reduced stiffness.

It would be difficult to consider nozzle loading accurately by means of the current design method, especially since the nature of the loading [1] and the header box geometry in itself represents a full three-dimensional problem. The assumptions used in formulating the current practice solution must also be reviewed so as to establish the representativeness of the ensuing header box stress distribution. It is the intention of the present study to investigate these concerns via the design by analysis approach (see Chapters 7 and 8).

5 Rigid frame theory as a means for a design by rule method

In an attempt to find alternative means for evaluating the stress distribution in the header box bonnet without consideration of a nozzle, rigid frame theory was employed.

According to Norris et al. [14] a rigid frame may be defined as '... a structure composed of a number of members all lying in one plane and connected so as to form a rigid configuration by joints, some or all of which are moment-resisting (rigid) instead of hinged ...'. A rectangular rigid frame can be represented by two vertical columns, joined by a cross tie (horizontal member), which are either hinged or fixed to the support (see Figure 5-1). In many cases the support constraints result in a statically indeterminate system, which may be solved analytically via deformation based methods. Expressions for the slope and displacement on the elastic curve of a beam are essential in this approach.

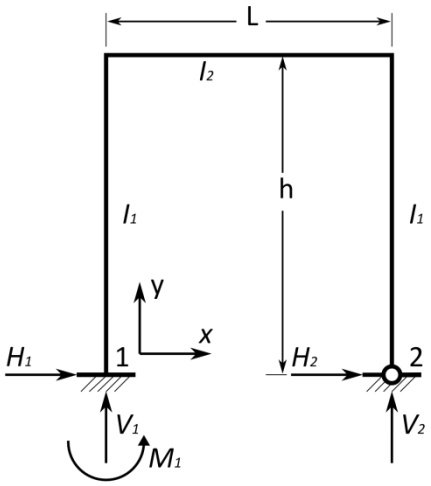

Figure 5-1: Example loading diagram of a rigid frame (adapted from [15])

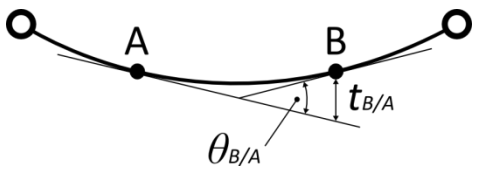

Figure 5-2: Relative deflection formula for an elastic curve (adapted from [16])

To compute the slope and displacement of an elastic curve, the moment-area method [16] is used, where respective solutions are presented by Equations (5-1) and (5-2). As the name implies, this method relies on the calculation of areas associated with a curve's bending moment diagram.

$$\theta_{B/A} = \int_A^B \frac{M}{EI} dx \qquad \textbf{(5-1)}$$

$$t_{B/A} = \int_A^B x \frac{M}{EI} dx \qquad \textbf{(5-2)}$$

With Equation (5-1), the relative slope of two points (*A* and *B*) on an elastic curve is computed. Equation (5-2) is used to compute the transverse deflection of a point (*B*) with respect to the projected tangent of another point (*A*) on the same elastic curve (see Figure 5-2).

A compilation of frame formulas is furthermore presented in Griffel [15] with application to specific boundary condition and loading scenarios. Griffel [15] adopts the elastic energy method, whereby a

"dummy" load is used in the place of an existing boundary constraint to enforce an overall deformation requirement. It should however be noted that in Griffel's [15] approach, and consequently this study, distortion due to axial forces is neglected. These effects are inherently dealt with by the finite element software package MSC.Nastran [17,18], and are shown to have a small influence on the calculation of reaction forces and stresses in Section 5.1.1 upon comparison.

From the geometry depicted in Figure 5-1, it follows that an analogy may be struck between the rectangular rigid frame, and the construction of the header box bonnet. In many of the rigid frame models provided in Griffel [15], both of the vertical beams are assumed to be of the same uniform thickness and resultantly second moment of area, whereas the cross tie has distinct uniform properties. Similarly, the side plates of a header box bonnet are typically identical with a distinct tube sheet.

Using a rigid frame modelling approach, a number of boundary constraint configurations is investigated in this chapter for comparison with the current header box design method, as well as a finite element model solution. To this end, investigations were performed both for the inclusion and exclusion of flange arms and are elaborated upon in the sections to follow.

5.1 Flanged frame model

A comprehensive evaluation of the header box bonnet as a rigid frame is expected to provide an improved approximation over current design practice to its behaviour under load. With this in mind, a flanged frame model, which takes account of the lever arm over which the bolts of the flanged connection act (see Figure 5-3), was developed.

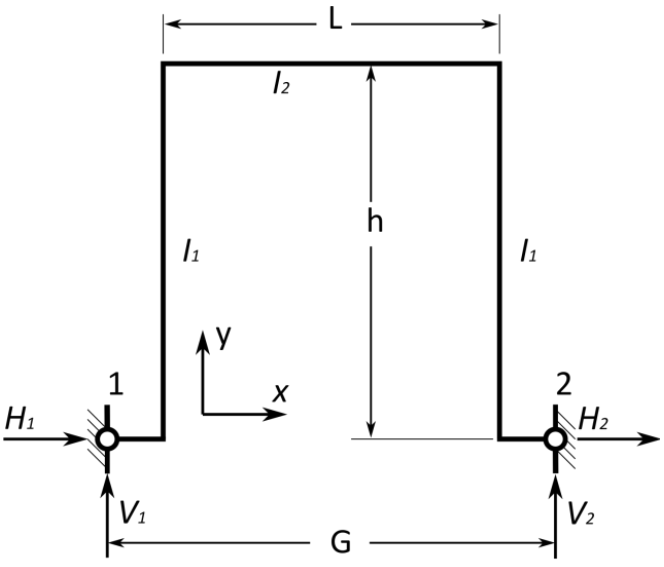

Figure 5-3: Flanged supports diagram

Two boundary constraint scenarios were evaluated for this geometry, including constrained and unconstrained hinged supports. Bolt and pressure loading were included for each. Bolt loading is enforced by means of bending moment M_{jw} acting at both of the hinged supports, whereas pressure

loading is taken care of by a uniformly distributed load. As in current practice, the bending moment M_{jw} is calculated by reducing the offset tensile forces in the bolt, and reaction forces in the gasket to an effective couple acting on the bonnet. The overall length between the locations at which the flange arms are cut (*1* and *2*) may be represented by the recalculated outer gasket width *G* (see Figure 5-3).

To furthermore evaluate the accuracy of derived solutions, analytical results were directly compared with equivalent one-dimensional beam models built in MSC.Patran [17,18] and solved via MSC.Nastran [17,18]. As current design practice is based on unit depth beam calculations, the same principle was implemented here. To draw comparisons the ensuing stress distributions along the side plate and tube sheet were also plotted comparatively. Exactly the same dimensions as per Chapter 4 were used, although the bolt bending moment (M_{jw}) was based on Equations (4-19) and (4-21). With reference to Figure 5-3, details are provided in Table 5-1.

Table 5-1: Details for the rigid frame analysis

Variable	*Symbol*	*Value*	*Units*
Rigid frame model details			
Pressure	P	1.000	MPa
Bolt bending moment	M_{jw}	8773.9	Nm/m
Header depth	h	223	mm
Header height	L	240	mm
Outer gasket width	G	314.2	mm
Side-plate thickness	t_s	27	mm
Tube sheet thickness	t_t	27	mm
Flange plate thickness	t_f	30	mm

5.1.1 Constrained hinged supports model

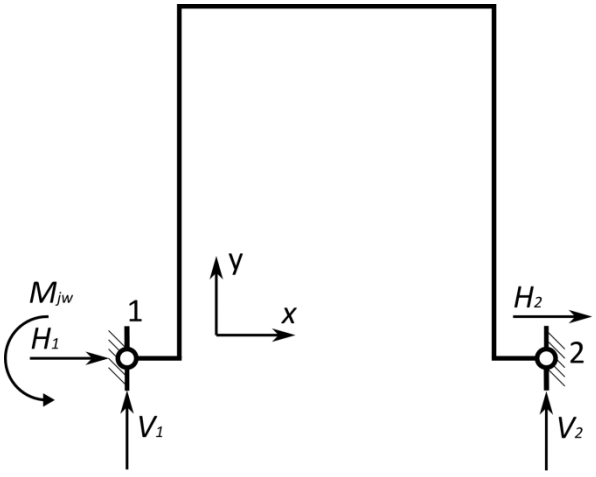

Figure 5-4: Single-sided application of bolt induced bending moment to the constrained flanged frame model. For application at both of the supports, superposition is implemented

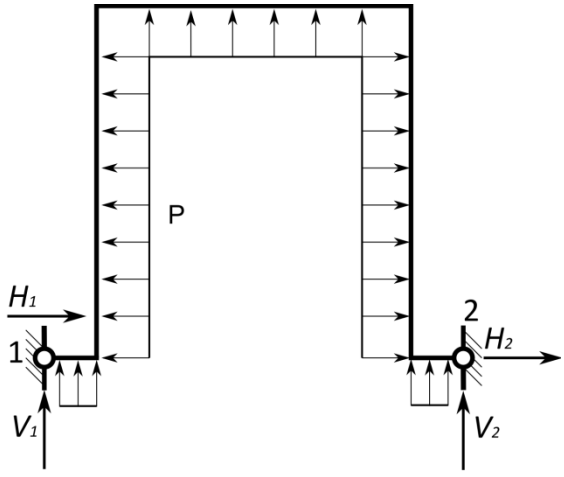

Figure 5-5: Pressure load applied to the constrained flanged frame model

In the constrained form, the supports of the rigid frame are prohibited from moving relative to one another. To some extent, this may be perceived as representing a perfectly rigid cover-plate for the header box. Two independent statically indeterminate problems have to be solved as illustrated by Figures 5-4 and 5-5, for each of the load sources (bolts and pressure). This is done by the method of elastic energy, as per Griffel [15], below. Once all of the reaction forces are solved for both cases, the two results may be superimposed and a stress distribution calculated.

- ***Detailed solution to the bolt loading problem***

In this case, bolt loading is evaluated for application to only one of the hinged supports (see Figure 5-4). To extend the solution for bolt loading on both supports, the bending moment is superimposed on either end.

As mentioned, a "dummy" load is implemented to satisfy a total deformation requirement. This is done so as to enforce the analysis of a statically determinate system. In the case of the bolt loading problem we remove the boundary constraint force H_2 from the model. This gives three unknown reactions (H_1, V_1 and V_2), which may be computed from the three available equations of equilibrium (see Equations (5-3) to (5-5)). Subsequently, a full bending moment diagram may be found for the rigid frame as in Figure 5-6, where k denotes the flange arm length (i.e. $k = (G - L)/2$).

Since H_2 is removed, $H_1 = H_2 = 0$. **(5-3)**

$$\sum M_1 = 0 \Rightarrow V_2 = -\frac{M_{jw}}{G} \quad \textbf{(5-4)}$$

$$\sum F_y = 0 \Rightarrow V_1 = \frac{M_{jw}}{G} \quad \textbf{(5-5)}$$

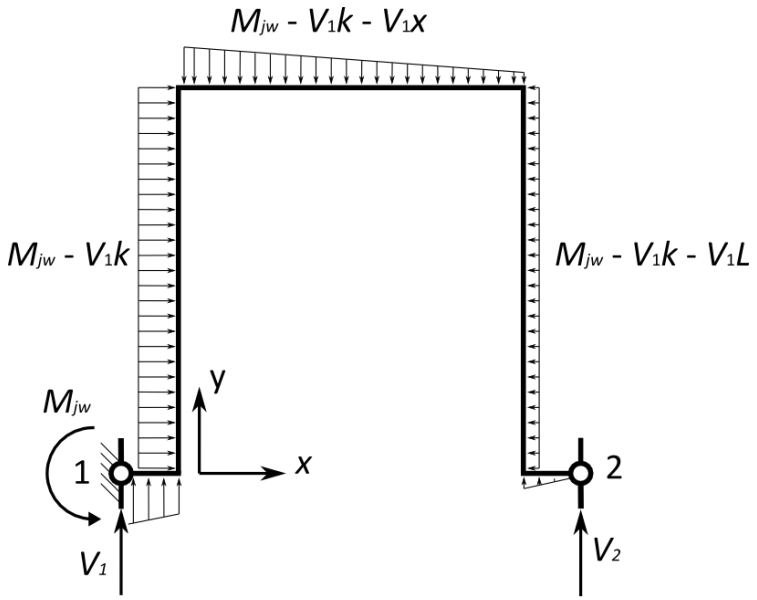

Figure 5-6: Bending moment diagram A for the bolt loading problem

In addition, the discarded force is implemented in a "dummy" load scenario, whereby only a unit force H_2 is applied. Once again, the remaining reaction forces are subsequently computed (see Equations (5-6) to (5-8)) and used to evaluate a bending moment distribution (see Figure 5-7). Note that since a sign convention is consistently followed, the orientation of the reactions follows from the analysis.

$$\sum F_x = 0 \Rightarrow H_1 = -H_2 \tag{5-6}$$

$$\sum M_1 = 0 \Rightarrow V_2 = 0 \tag{5-7}$$

$$\sum F_y = 0 \Rightarrow V_1 = 0 \tag{5-8}$$

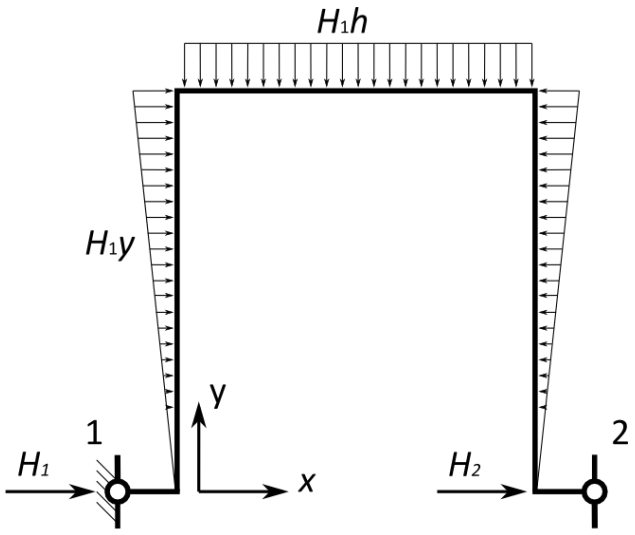

Figure 5-7: Bending moment diagram B for the bolt loading problem

Finally, the theory of elastic energy is used to dictate that the overall horizontal deflection at point 2, due to the simply supported bolt induced loading (Figure 5-6) and "dummy" load (Figure 5-7) scenarios, must equal zero. For this implementation, integration is performed along the length of the frame from joint 1, where a value for distance from the *x*-axis is used for the displacement orientation. This may be observed in the derivation of reaction force H_1 in Equation (5-9).

$$t_A + t_B = 0$$

$$\left[\int_0^h \left(M_{jw} - V_1 \times k\right)\frac{y}{EI_1}dy + \int_0^h M_{jw} - V_1\left(k+L\right)\frac{y}{EI_1}dy + \int_0^L \left(M_{jw} - V_1 \times k - V_1 \times x\right)\frac{h}{EI_2}dx\right] + \ldots$$

$$\ldots \left[2\int_0^h H_1 \frac{y^2}{EI_1}dy + \int_0^L H_1 h \frac{h}{EI_2}dx\right] = 0$$

$$\left[\left(M_{jw} - V_1 k\right)\frac{h^2}{2I_1} + \left(M_{jw} - V_1\left(k+L\right)\right)\frac{h^2}{2I_1} + \left(M_{jw} - V_1 k\right)\frac{hL}{I_2} - V_1\frac{hL^2}{2I_2}\right] + H_1\left[\frac{2h^3}{3I_1} + \frac{Lh^2}{I_2}\right] = 0$$

Simplify to obtain an expression for H_1.

Substitute $k = \frac{G-L}{2}$ and from equilibrium $V_1 = \frac{M_{jw}}{G}$.

$$H_1 = \frac{M_{jw}\left[-h^2/2I_1 - hL/2I_2\right]}{2h^3/3I_1 + Lh^2/I_2} \qquad \textbf{(5-9)}$$

With H_1 known, the remaining reaction forces may be computed from equilibrium. Subsequently, this solution may be superimposed for application of the bolt loading on either end of the supports. Consequently, the horizontal reaction forces (H_1 and H_2) double, whereas the vertical reaction forces cancel out.

- ***Solution to the pressure loading problem***

Solving the pressure loading problem in Figure 5-5 follows in exactly the same manner. The horizontal reaction force at joint 2 is once again removed, and a "dummy" load introduced, whereby bending moment distributions for two statically determinate problems (*A* and *B*) are solved. Subsequently, the reaction force H_1 is derived by means of the theory of elastic energy (see Equation (5-10)), with the remaining reaction forces following from equilibrium.

$$t_A + t_B = 0$$

$$\left[\begin{array}{c} 2\int_0^k \left(-V_1 x - P\frac{x^2}{2}\right)\times\frac{0}{EI_{flange}}dx + 2\int_0^h \left[-V_1 k - P\left(\frac{k^2}{2}+\frac{y^2}{2}\right)\right]\times\frac{y}{EI_1}dy + \ \ldots \\ \ldots \int_0^L \left[-V_1(k+x) - P\left(kx+\frac{k^2}{2}+\frac{h^2}{2}+\frac{x^2}{2}\right)\right]\times\frac{h}{EI_2}dx \end{array}\right] + \left[2\int_0^h H_1\frac{x^2}{EI_1}dx + \int_0^L H_1 h\frac{h}{EI_2}dx\right] = 0$$

$$\frac{2}{I_1}\left[-V_1 k\frac{h^2}{2} - P\frac{k^2h^2}{4} - P\frac{h^4}{8}\right] + \frac{1}{I_2}\left[-V_1 khL - V_1\frac{L^2h}{2} - P\frac{khL^2}{2} - P\frac{k^2hL}{2} - P\frac{h^3L}{2} - P\frac{hL^3}{6}\right] + H_1\left[\frac{2h^3}{3I_1} + \frac{Lh^2}{I_2}\right] = 0$$

Simplify to obtain an expression for H_1.

Substitute $k = \frac{G-L}{2}$ and from equilibrium $V_1 = \frac{M_{jw}}{G}$.

$$H_1 = \frac{P/I_1 \times \left(h^4/4 - G^2h^2/8 + L^2h^2/8\right) + P/I_2 \times \left(Lh^3/2 + L^3h/24 - G^2Lh/8\right)}{2h^3/3I_1 + Lh^2/I_2} \qquad \textbf{(5-10)}$$

- ***Superimposed solutions compared to 1D FEM***

An exaggerated deformation and maximum combined stress (bending plus membrane) plot were superimposed from finite element model results and are included in Figure 5-8. The rotation of the supports in this figure is indicative of the hinged support assumption. The peak value for stress may furthermore be observed to occur in the vicinity of the side plate to flange junction.

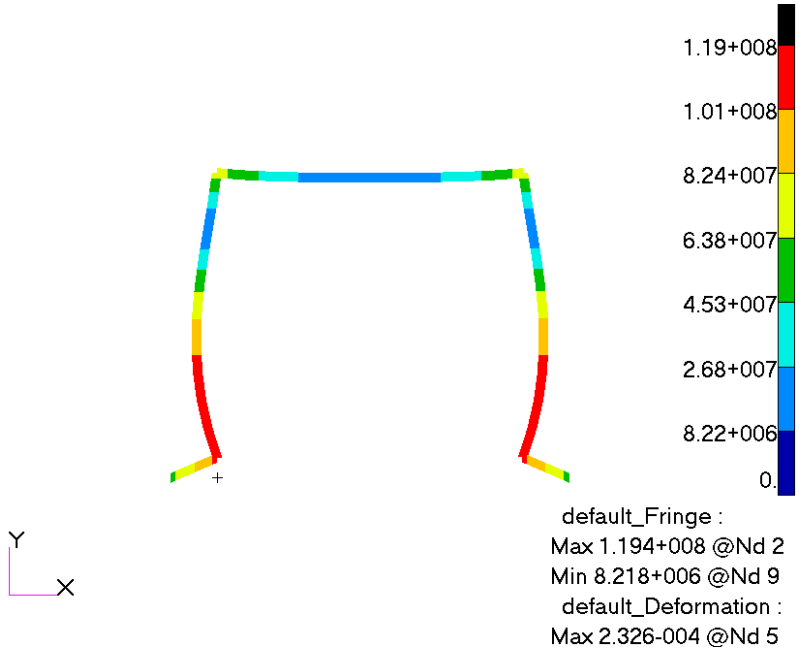

Figure 5-8: Maximum combined stress for constrained pivot-base problem (deformation scaled by a factor of 100)

Only the solutions presented in Equations (5-9) and (5-10) following from Griffel's [15] approach are affected by the negligence of axial beam distortion. These correspond to the horizontal reaction forces (H_1 and H_2) at the supports for the cases of bolt loading and pressure respectively. The solution for the vertical reaction forces (V_1 and V_2) are unaffected, since they are independent of the overall deformation requirement and can be solved by means of equilibrium. Table 5-2 illustrates the difference between the horizontal reaction forces calculated by the elastic energy method and the finite element method. The analytical solutions are within approximately 0.5 %.

Table 5-2: Difference between reaction forces for the flanged rigid frame model (constrained supports) following from the elastic energy method and finite element analysis

Reaction force	*Theory of elastic energy*	*Finite element model*	*Percentage difference*
H_1 (bolt loading)	-46 870 N/m	-46 632 N/m	0.51 %
H_1 (pressure loading)	60 088 N/m	60 408 N/m	0.53 %

Bending and axial stress values at nodal points along the side plate and tube sheet were furthermore extracted and compared against the derived analytical solution. The derived reactions forces and moments were simply used to compute nominal axial and bending stress values throughout the frame. The absolute difference between the two cases, for superimposed bolt and pressure loading, may be observed in Figure 5-9. As should be expected, the difference in bending stress is seen to rise linearly along the side plate and to remain constant along the length of the tube sheet. The

horizontal reaction force induces a bending stress which is a linear function of displacement from the *x*-axis. The difference in axial stress is zero along the side plate, and also constant along the tube sheet. Upon substituting the horizontal reaction forces computed by the finite element solution into the rigid frame solution, all the differences could furthermore be observed to reduce to zero.

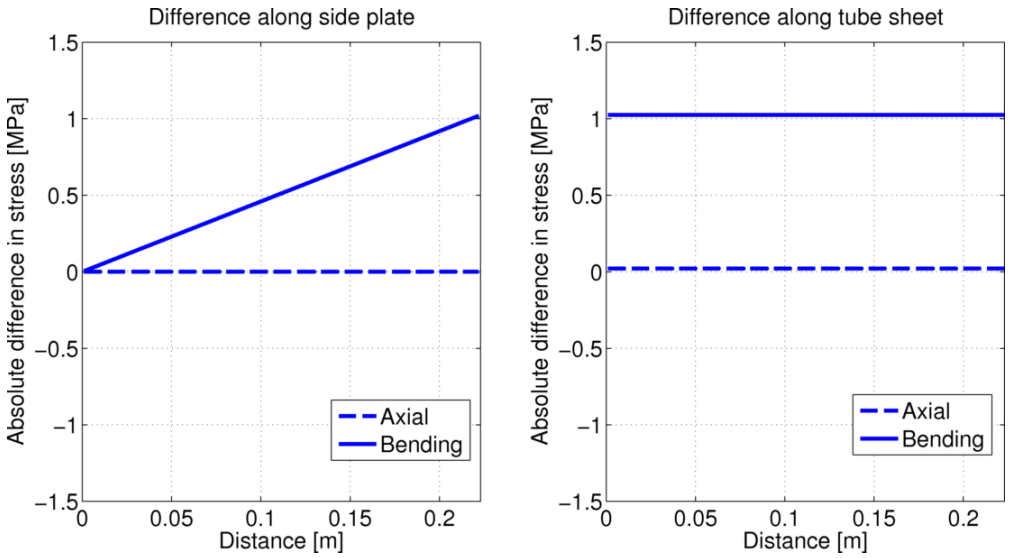

Figure 5-9: Absolute difference in stress between the elastic energy method and finite element for the case of the flanged rigid frame model having constrained supports

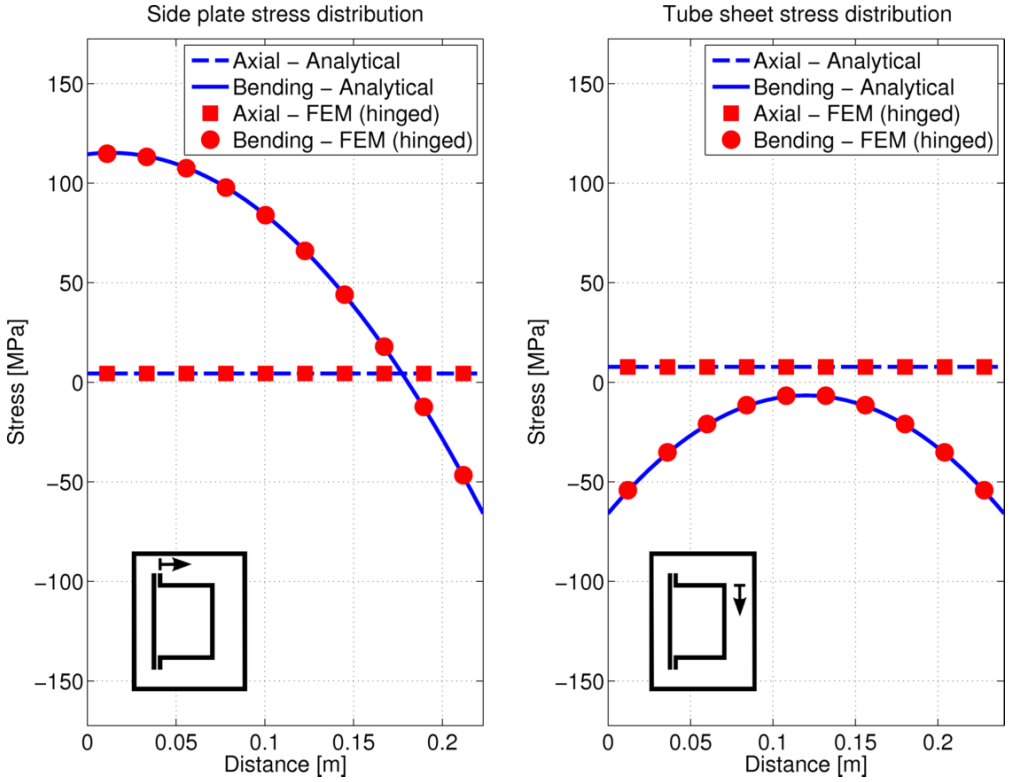

Figure 5-10: Stress distribution for the constrained flanged rigid frame model

A plot comparing the overall stress distribution result for the analytical and 1D finite element solutions is presented in Figure 5-10. It follows that the greatest difference in bending stress is at the junction formed by the side plate and tube sheet, and along the tube sheet's length. In the case of

the junction, the percentage difference is 1.6 %. For the uniform axial stress difference along the tube sheet, it is 0.3 %.

5.1.2 Unconstrained hinged supports model

In the unconstrained flanged frame model, free relative horizontal movement is allowed between the two supporting joints. Contrary to the constrained case, this more closely correlates with a header box cover-plate having zero stiffness.

By setting the supports to be unconstrained in the horizontal direction, the reaction force H_2 is removed. In doing so, the rigid frame effectively becomes simply supported, and therefore represents a statically determinate problem. An exact solution may be found by means of the equations for equilibrium.

For application of the bolt induced bending moment only, at both of the joints, they effectively cancel resulting in nil reaction forces prevailing at the supports. This results in a uniform bending moment existing throughout the frame. Furthermore, for the advent of internal pressure the only reactions are of vertical orientation (see Equation (5-11)).

$$V_1 = V_2 = -\frac{PG}{2} \qquad \textbf{(5-11)}$$

Nominal axial and bending stress distributions now follow for known reactions at the supports, and may be compared against finite element results as before. Comparative plots are included in Appendix A.1.

5.2 Simple frame model

In the simple frame model, the header box bonnet is modelled by the rigid frame depicted in Figure 5-1. In doing so, the contribution of the flange arms is discarded. This correlates with the current design approach, since the bending moment for bolt loading is applied directly at the end of the side plate. There is no offset for the flange section. In current practice however, a number of assumptions are made with regard to the interaction between both of the side plates and the tube sheet, whereby each of the plates is evaluated independently. By evaluating the collection of beams as a rigid frame an improved solution may be obtained.

Four boundary configurations were considered for this model, including both constrained and unconstrained hinged support and fixed support scenarios. The hinged scenario allows for direct application of the bolt induced bending moment at the supporting joints, although zero moment resistance to internal pressure load is provided. This is solved in the same manner as the two flanged frame cases.

Fixed supports on the other hand represent a built-in scenario, whereby rotation at the supporting joints is resisted. This however presents a complication, since the bolt bending moment can't be implemented at the supporting point. To circumvent it, the bolt bending moment scenario is

evaluated for hinged supports, whereas the pressure loading scenario is evaluated for built-in supports. This approximately corresponds to enforcing a rotation at the supports for the case of bolt loading, and superimposing a pressure load scenario for the built-in assumption.

5.2.1 Constrained support models

The constrained support models present statically indeterminate problems which are required to be solved via a deformation based method. In keeping with the approach followed thus far, these problems will be solved via the superposition of a bolt bending moment problem, and an internal pressure loading problem. Additional details and comparative plots for the solutions are provided in Appendix A.2.1. The expressions for the important reactions are however repeated here for convenience.

5.2.1.1 Hinged supports

Of all the simple frame models, this one has the closest correlation to the approach used in current design practice. In this instance however, interaction between all of the plates is dealt with inherently. Free body diagrams for the bolt loading, and internal pressure loading problems are presented in Figure 5-11.

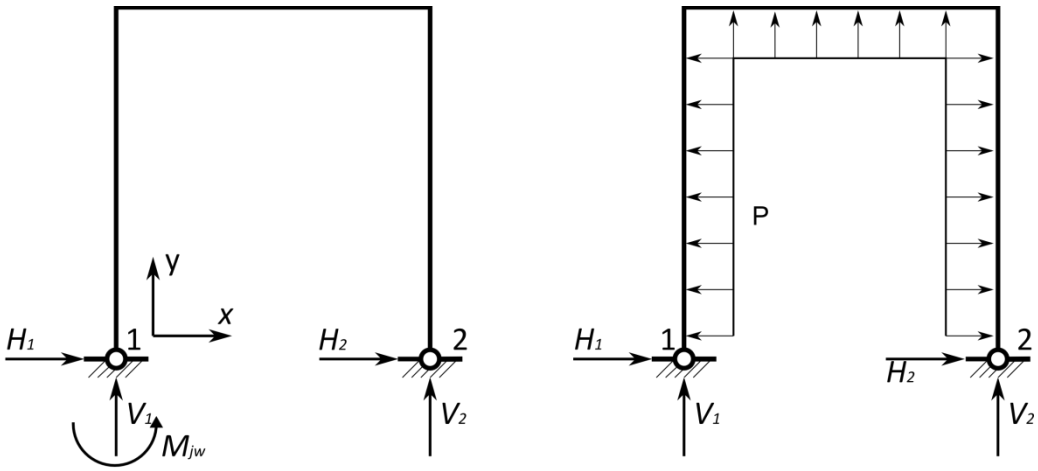

Figure 5-11: Constrained simple frame model having hinged supports

Expressions for the reaction force H_1 in the case of bolt loading and pressure loading is respectively provided in Equations (5-12) and (5-13). The remaining reaction forces may of course be solved for via force and moment equilibrium. From Equation (5-12), the bolt bending moment case may be observed to reduce to the same expression as for the flanged frame model (see Equation (5-9)). Comparably, the same solution would have been obtained for the pressure loading problem if *G* and *L* were equal, in other words, if there had been no flange arm.

$$H_1 = \frac{M_{jw}\left[-h^2/2I_1 - hL/2I_2\right]}{2h^3/3I_1 + Lh^2/I_2} \qquad \textbf{(5-12)}$$

$$H_1 = \frac{Ph^4/4I_1 + PLh^3/2I_2 - PL^3h/12I_2}{2h^3/3I_1 + Lh^2/I_2} \quad \textbf{(5-13)}$$

5.2.1.2 Fixed supports

In this rigid frame model, the vertical columns are assumed to be fixed at the support. The two joints are also restricted from relative movement. This strictly applies for the internal pressure loading, and is intended to be representative of a scenario where the flange is large. To further address the bolt loading problem, the solution to the hinged support model is superimposed. Taking account of the respective loading scenarios in this manner is meant to correlate with the mechanisms by which each load case acts. The loading scenarios may be observed in Figure 5-12.

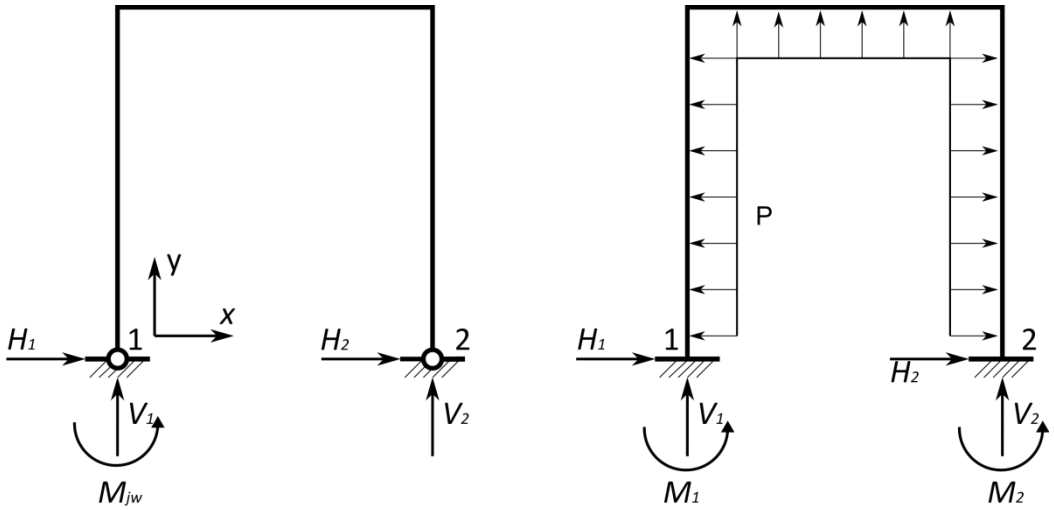

Figure 5-12: Constrained simple frame model having fixed supports

As the bending moment scenario has already been solved via the evaluation of the hinged supports model (see Equation (5-12)), all that remains is to solve for the pressure loading case. In this instance it is more complicated since more than one reaction force would have to be removed to gain a statically determinate system, which necessitates the further use of both displacement and slope evaluations to obtain a solution. Fortunately, from the compilation of solutions offered in Griffel [15] superposition could be utilised to solve for the reactions. The derivations of the solutions, as well as comparative plots, are presented in Appendix A.2.2. The corresponding reaction forces and moments are presented in Equations (5-14) through (5-16).

$$M_1, M_2 = \pm\frac{P \times L^2}{12D} \pm Ph^2\left\{\frac{-C}{12D}\left[1 + \frac{3}{C}\right]\right\} \quad \textbf{(5-14)}$$

$$H_1, H_2 = \mp\frac{P \times L^2}{4hD} \pm Ph\left\{\frac{1}{2} + \frac{1}{4D}\right\} \quad \textbf{(5-15)}$$

$$V_1, V_2 = \frac{-PL}{2} \quad \textbf{(5-16)}$$

Where $C = \frac{I_2}{I_1}\left(\frac{h}{L}\right)$ and $D = 2 + C$.

5.2.2 Unconstrained support models

In these two final rigid frame models the joints are left free to move relative to one another along the horizontal axis.

5.2.2.1 Hinged supports

For hinged supports, the unconstrained assumption results in the rigid frame being simply supported. This in turn represents a statically determinate problem. A solution may therefore be obtained directly by means of the equilibrium equations. As in the case of the unconstrained flanged frame model, the only support reactions exist for internal pressure loading, and are of vertical orientation (see Equation (5-17)).

$$V_1, V_2 = -\frac{PL}{2} \tag{5-17}$$

5.2.2.2 Fixed supports

In this unconstrained configuration the side plates are modelled as being built in. As was done for the corresponding constrained case the bending moment for the bolt load is superimposed via a hinged assumption. The two superimposed scenarios may be observed in Figure 5-13.

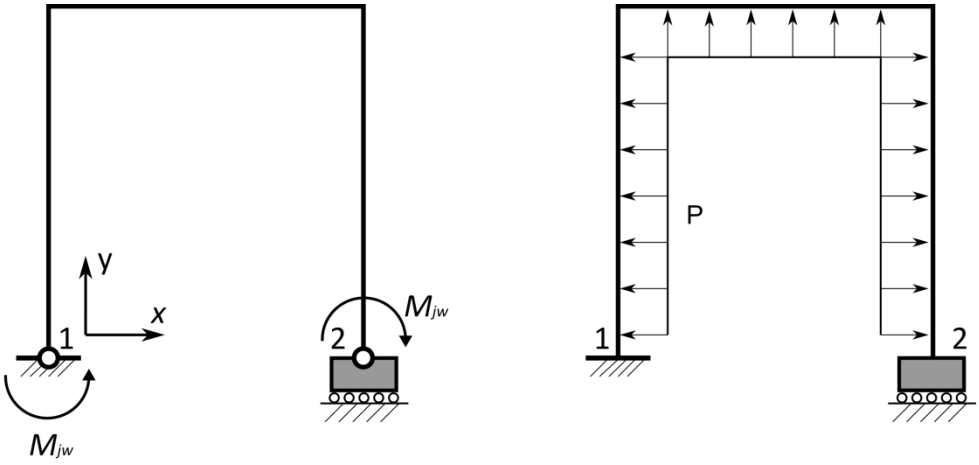

Figure 5-13: Superimposed cases for unconstrained fixed supports case

As was observed for the hinged model in the previous section, the bolt loading case once again represents a statically determinate system for which a uniform bending moment exists throughout the frame. The internal pressure loading case is however statically indeterminate. Since the vertical columns are fixed, the slope of the elastic curve represented by the deformed rigid frame at the joints must equal zero (displacement in *x* with respect to *y*). The slope may therefore be used as an

overall deformation requirement via the application of "dummy" moment reactions at the joints. As a result of the symmetrical construction and loading, the moment reactions at joint 1 and 2 are furthermore equal and opposite in sign.

The derivation of the solution to the pressure loading problem is presented in Appendix A.2.4, as well as validation plots. The corresponding reactions forces and moments are presented in Equations (5-18) through (5-20).

$$V_1 = V_2 = -\frac{PL}{2} \tag{5-18}$$

$$H_1 = H_2 = 0 \tag{5-19}$$

$$M_1, M_2 = \pm \frac{Ph^3/3I_1 + P/I_2\left(Lh^2/2 - L^3/12\right)}{2h/I_1 + L/I_2} \tag{5-20}$$

6 Finite element modelling and analysis

A number of problematic issues have to be overcome to generate a dependable finite element model of a header box. Provision has to be made for the rectangular flange, including a gasket and fasteners, as well as the welded joints and supporting structure, amongst others. The present chapter serves to highlight these difficulties, and attempts to provide viable solutions towards the development of a representative finite element model. In addition, the method of linearization is looked at more closely as a means for analysis.

6.1 Linearization

It is thought prudent to first illustrate the method by which results are processed for comparisons and evaluation of failure criteria: linearization. It is presented in the ASME code [5] and was first introduced on page 10 as part of the design by analysis approach. In short, linearization involves the extraction of a bending (linear) and membrane (uniform) component from the stress distribution represented along a straight line across the thickness of a finite element model. The process of extraction is performed by a method of integration (see Equations (2-1) and (2-2), repeated below for convenience). As mentioned, three methods are available for performing stress linearization, but it was decided to follow the stress integration method (see Section 2.1.2.2). It presents the simplest option in view of the complexity associated with generating a mesh for the header box geometry.

$$\sigma_{ij}^{m} = \frac{1}{t}\int_0^t \sigma_{ij} dx \qquad \textbf{(6-1)}$$

$$\sigma_{ij}^{b} = \frac{6}{t^2}\int_0^t \sigma_{ij}\left(\frac{t}{2} - x\right) dx \qquad \textbf{(6-2)}$$

The stress at any point in a continuum may of course be represented as a second order tensor, having six independent components. These components have to be linearized independently, according to prescribed guidelines. Two principles in particular, have to be kept in mind, namely [5]:

1. a bending stress is not to be calculated for the local component stress parallel to the SCL;
2. a bending stress is not to be calculated for the local component in-plane shear stress.

The through-thickness (parallel to SCL) and applicable shear stress components are only to be evaluated via a membrane stress. Torsion is a form of shear which may however require special treatment if the nature of the loading implicates it, although it still can't be viewed as a bending stress. These principles were incorporated into the linearization procedure, where for each stress concentration line (SCL) a local coordinate system is used, in accordance with the ASME code [5].

6.1.1 Numerical implementation of integration rules

To evaluate Equations (6-1) and (6-2) numerically two avenues were explored, as listed below.

A. *Extended trapezoidal rule*: Exact for linear polynomial functions.

B. *Simpson's rule*: Exact for quadratic polynomial functions.

Equations (6-3) and (6-4) provide expressions for integration by Simpson's rule in discrete form. Provision is also made for method A, included in Appendix B.

$$\sigma_{ij,m} \approx \frac{h}{6t}\left[\sum_{k=1}^{N-1}\left(\sigma_{ij}\left(x_s^k\right)+4\sigma_{ij}\left(\frac{x_s^k+x_s^{k+1}}{2}\right)+\sigma_{ij}\left(x_s^{k+1}\right)\right)\right] \tag{6-3}$$

$$\begin{aligned}\sigma_{ij,b} \approx \frac{h}{t^2}\Bigg[\sum_{k=1}^{N-1}\Bigg(&\sigma_{ij}\left(x_s^k\right)\times\left(\frac{t}{2}-x_s^k\right)+ \quad \ldots \\ &\ldots\ 4\sigma_{ij}\left(\frac{x_s^k+x_s^{k+1}}{2}\right)\times\left(\frac{t}{2}-\frac{x_s^k+x_s^{k+1}}{2}\right)+\ \ldots \\ &\ldots\ \sigma_{ij}\left(x_s^{k+1}\right)\times\left(\frac{t}{2}-x_s^{k+1}\right)\Bigg)\Bigg]\end{aligned} \tag{6-4}$$

The symbols used are defined as follows:

t = thickness of section;

x_s = coordinate along section;

$\sigma_{ij}\left(x_s^k\right)$ = σ_{ij} at point k along section;

h = the uniform interval size;

N = the number of intervals.

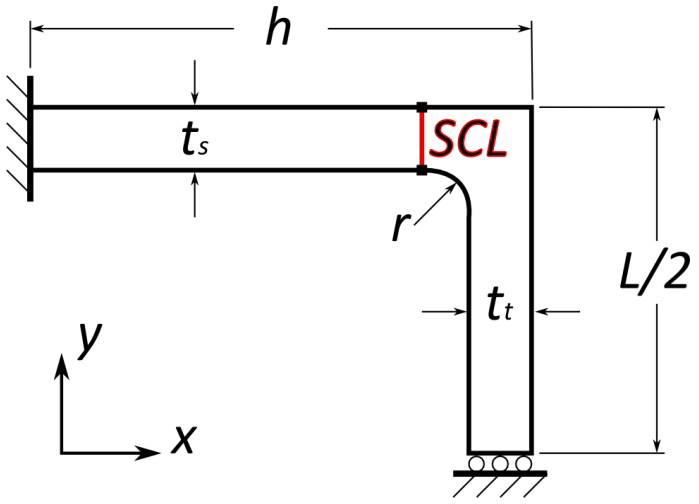

Figure 6-1: Example plane strain 2D model for linearization

Table 6-1: Example 2D model properties

2D Plane strain model properties	
Geometry	***Details***
h	220 mm
L	294 mm
t_t	27 mm
t_s	27 mm
r	8.5 mm
Material	
E	189 GPa
v	0.33
Load	
P	1 MPa

To further demonstrate the method of linearization, both methods A and B were implemented on a simple two-dimensional plane strain model, and evaluated for convergence. The example model is depicted in Figure 6-1 with its associated characteristics summarized in Table 6-1. The pressure load of 1 MPa is applied to all of the internal edges. This model effectively represents a half-symmetry

model of the bonnet of the header box as if it were rigidly supported at the flanges. In Section 6.3, the model is criticized as a means for modelling the header box. It is however adequate for the purpose of illustrating the method of linearization.

Eight-node quadrilateral (Q8) elements were used to mesh the geometry, and were refined based on the number of elements along the depicted SCL. This varied from one to as high as sixteen elements. The nodal values for each of the stress components along the length of the SCL were extracted in each case to perform linearization in MATLAB.

Trapezoidal integration is implemented by using each of the nodal values along the SCL. Simpson's rule is also quite straightforward, since along the edge of the elements a mid-side node is available. This complements the approach, since it requires three function values per evaluation. It may furthermore be noted that for the extraction of a membrane stress (Equation (6-3)) both the Trapezoidal and Simpson's rule method is expected to be exact, since each element inherently presents a linear stress distribution along the SCL. For the membrane plus bending stress however, a quadratic function must be integrated, and only Simpson's rule is exact.

The distribution of the stress components at the greatest level of refinement (16 elements) is depicted in Figure 6-2, where linearization results for the implementation of Simpson's rule is superimposed. Only four stress components are shown, since for a plane strain analysis the remaining shear components are zero.

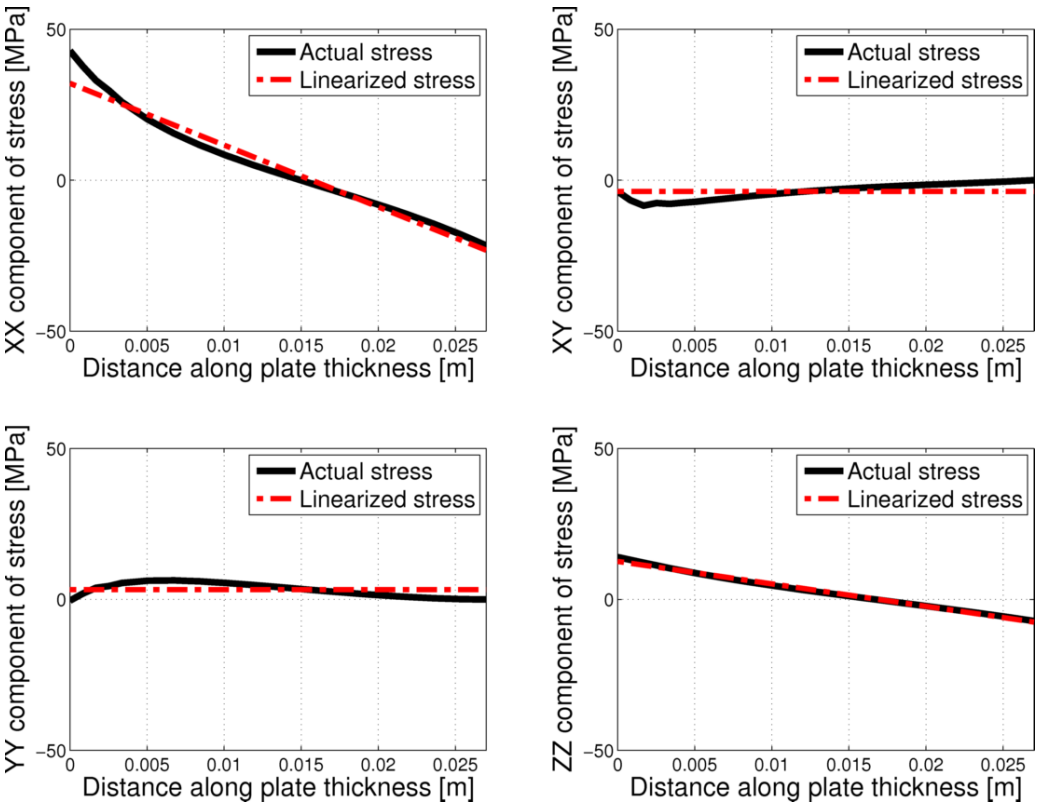

Figure 6-2: Stress component results for example 2D model to illustrate linearization (Simpson's rule)

Most notably, what may effectively be described as the hoop and meridional components of stress (the XX and ZZ components respectively) are monotonically decreasing and are expected to

dominate the result. The remaining through-thickness (YY component) and shear (XY component) stresses are however questionable. Although the through-thickness stress approximates the operating pressure (-1 MPa) at the internal face and zero at the outer, it is not monotonically increasing. This is due to the bulky corner joint providing resistance against the deformation related to the hoop and meridional components of stress. Furthermore, the shear stress distribution is not ideally parabolic. It is somewhat skewed. It does however approximate a value of zero at either end of the SCL, which is expected, since there is no shear traction on the surfaces, or forces supporting the notion of a shear stress distribution resulting from torsion.

Only membrane stresses may be evaluated in the case of the through-thickness and shear stress distributions, both of which may be observed as being reasonably small. In the case of the shear stress, the linearized value is approximately 12.5 % of the peak linearized hoop stress. The criterion of a parabolic distribution may be waived in the instance of a small linearized value. Furthermore, the linearized through-thickness stress is approximately 11 % of the peak linearized hoop stress. Since this problem can be observed as being dominated by bending stress, both the shear and through-thickness components will be assumed small enough to validate linearization. These results are in any case only intended to illustrate integration via the mentioned routines.

To establish convergence, the equivalent membrane and membrane plus bending values were evaluated as per Equation (2-3) for each level of refinement. The results for the two numerical approaches are presented in Figure 6-3. Each approach may be observed to converge to the same value for the respective integration rules.

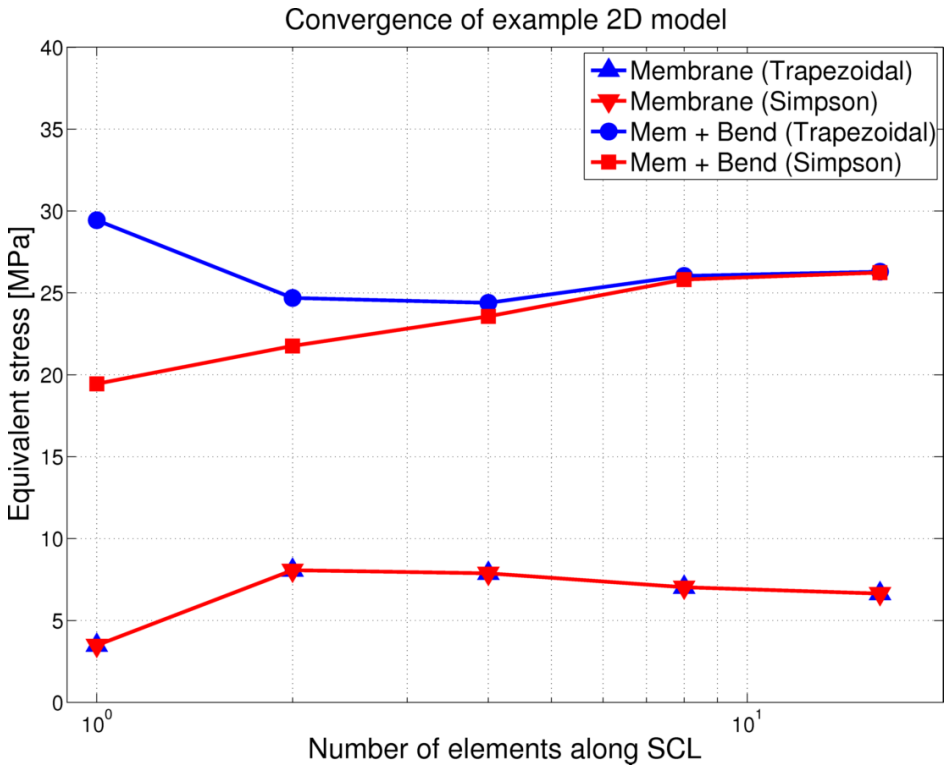

Figure 6-3: Convergence of example 2D model to demonstrate linearization

The equivalent membrane plus bending stress results are furthermore tabulated in Table 6-2. The results for the Simpson's rule implementation converge in a consistently increasing manner. Some

difficulties however arise with the implementation of the trapezoidal rule as it is very dependent on the number of nodal values and may converge from above or below, depending on the curvature of the stress distribution.

Table 6-2: Convergence of equivalent membrane plus bending stress for SCL depicted in Figure 6-1

	Numerical approach	
Number of elements	***Trapezoidal rule***	***Simpson's rule***
1	29.44 MPa	19.45 MPa
2	24.69 MPa	21.77 MPa
4	24.39 MPa	23.57 MPa
8	26.04 MPa	25.81 MPa
16	26.29 MPa	26.24 MPa

Obtaining values for an arbitrary SCL stress distribution may prove time consuming in three dimensions, since the elements encapsulating the SCL have to be identified and shape interpolated, for specific points. To promote efficiency it is important to keep the number of interpolation points to a minimum. For the investigated methods, the standard Simpson's rule implementation is thought to be best.

6.1.2 Practical considerations for implementation and SCL selection

Depending on the structure, it may be appropriate to model a weld bead as square in certain cases (see Figure 6-4 in contrast to Figure 6-1). In doing so, we effectively introduce a singularity (weld toe) into a finite element model. To circumvent this, one may represent the weld toe by means of a small radius. This however requires a greater level of mesh refinement, and higher computational expense as a consequence. Certain implications of modelling a square fillet weld and the selection of an SCL will now be elaborated upon.

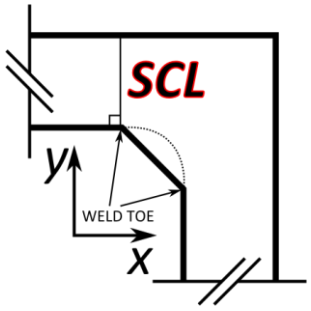

Figure 6-4: Square fillet weld and SCL selection

Representing a sharp weld toe complicates matters since convergence will not be obtained at a local point of interest. The method of linearization is intended to reduce the local effect of the singularity, since the stress distribution is integrated across the thickness. Nevertheless, it would not be a sensible decision to evaluate an SCL at the toe of the weld (as in Figure 6-4). It violates the requirement of having an SCL normal to both the internal and external surfaces. The through-thickness stress would for example not correspond with the internal pressure at the weld toe. To demonstrate the effects, the two-dimensional example shown in Figure 6-1 was adapted. In this

case, the round fillet is replaced by a square one having a throat thickness of 6 mm (see dotted line in Figure 6-4). The distribution of the stress components resulting from this modelling approach may be observed in Figure 6-5 for the finest level of refinement as per the previous case (16 elements along the SCL).

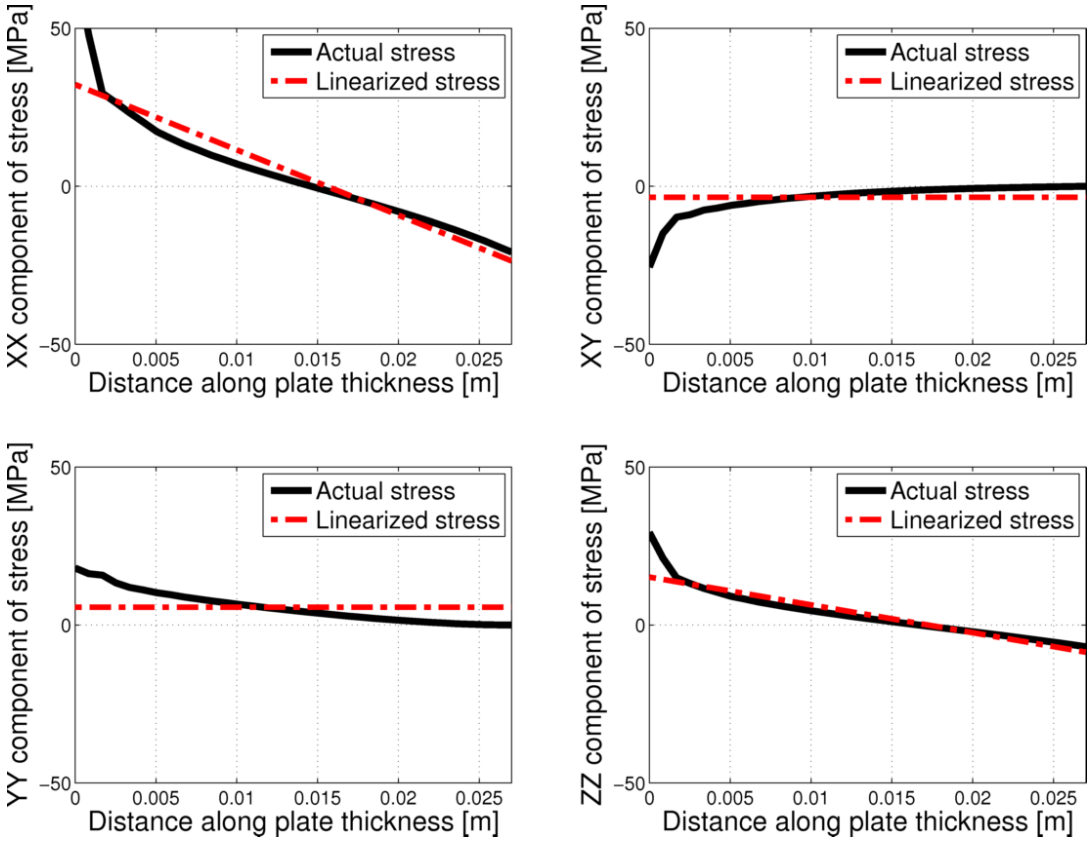

Figure 6-5: Stress component results for example 2D model having a square fillet

Both the hoop and meridional components are monotonically decreasing, where large values may be observed at the weld toe. As a result of this singularity, these values would inevitably approximate infinity in the limit of mesh refinement. In disagreement with the linearization guidelines, the through-thickness stress however fails to reflect the internal pressure at the weld toe. The shear stress also does not approximate a value of zero at this location. These results are to be expected, since the SCL is not located perpendicular to the internal surface.

Table 6-3: Linearized stress results comparison for example 2D model

Component of stress	Round fillet	Square fillet	Difference
XX	32.05 MPa	32.18 MPa	0.41 %
YY	3.270 MPa	5.645 MPa	72.63 %
ZZ	12.59 MPa	15.15 MPa	20.33 %
XY	-3.714 MPa	-3.525 MPa	5.09 %

Consider a comparison between the linearized component stress results for the square and round fillet cases in Table 6-3 at the weld toe. The greatest difference occurs for the through-thickness (YY) and meridional (ZZ) components of stress, where the square fillet model results in a higher value in both cases. This has the effect of bringing the normal stress components (XX, YY and ZZ) closer to

one another in value, and reducing the linearized Von Mises equivalent stress for the SCL as a result. If one were able to waive the linearization guidelines (i.e. assume the YY and XY components to be small), the prediction of failure by plastic collapse would therefore be less conservative. This may be clearly observed in the convergence plot of Figure 6-6.

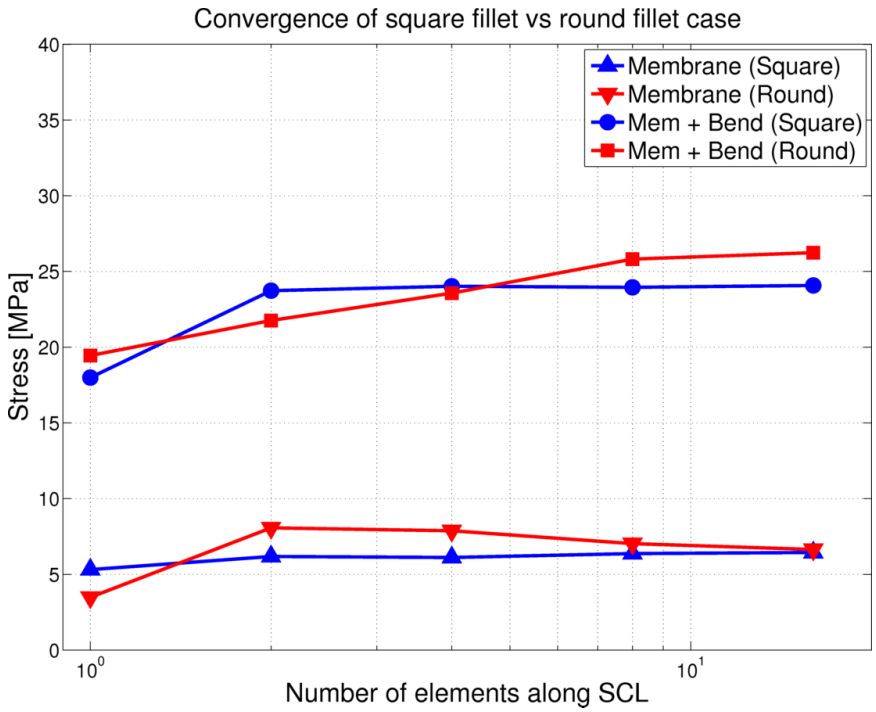

Figure 6-6: Comparison of convergence for the equivalent linearized stress of the round and square fillet cases

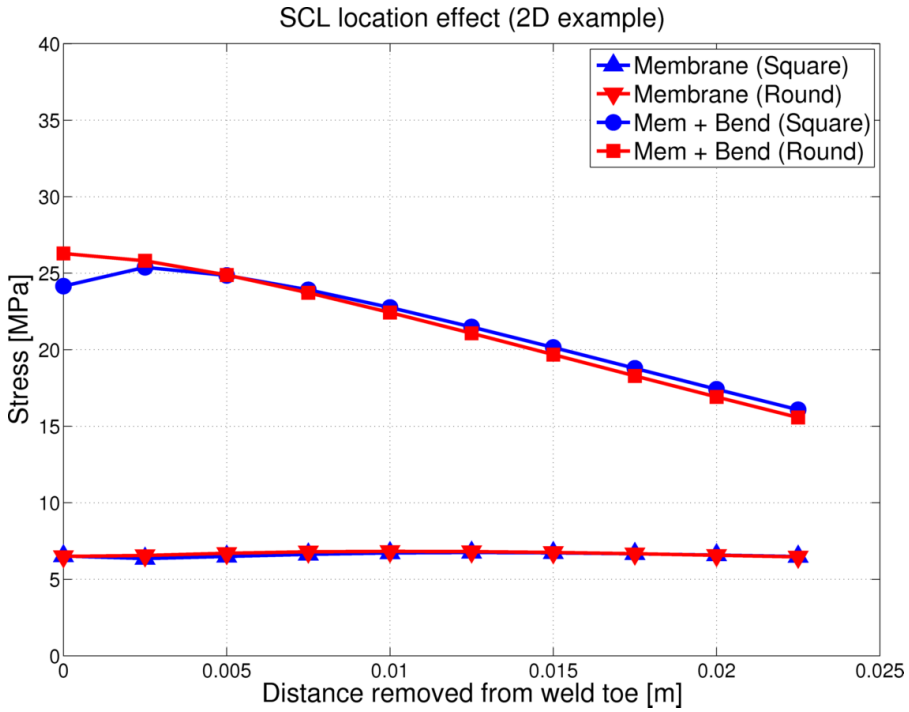

Figure 6-7: Equivalent linearized stress for SCLs located away from the weld toe for the example model

The linearization guidelines however strongly advise selecting a SCL perpendicular to the internal and external surfaces. It was therefore decided to investigate a few alternative configurations for the

square fillet case. To this end, the SCL was first positioned at locations away from the weld toe (i.e. the negative direction of the X-coordinate, see Figure 6-4). Equivalent stress results for this location effect are presented in Figure 6-7 for the round and square fillet cases. At the SCL locations away from the weld toe, the stress distribution is in accordance with the linearization guidelines for the square fillet, since the effect of the singularity is removed. The equivalent membrane plus bending stress for the round fillet case may be observed to decrease monotonically, whereas the stress in the square fillet case increases initially before steadily decreasing at greater distances. This increase is primarily due to a decrease in the linearized through-thickness stress upon adherence to the linearization guidelines. It would therefore seem advisable to evaluate a SCL slightly removed from the weld toe in this case, so as to obtain a more conservative solution. The round fillet would however provide the most conservative option overall at the weld toe. In addition, little effect on the equivalent membrane stress is noticeable, since it remains more or less uniform for both cases. Table 6-4 provides a comparison of the linearized results at the weld toe.

Table 6-4: Summary of the results pertaining to the 2D example

Weld profile	***Membrane [MPa]***		***Membrane + Bending [MPa]***	
Round fillet		6.494		26.29
Square fillet	(+ 0.4 %)	6.520	(-8.1 %)	24.16

As a further alternative, the SCL was also positioned diagonally across the junction formed by the side plate and tube sheet. This configuration can be considered to meet the linearization guidelines, since it complies with the component stress requirements at the surfaces. An illustration is provided in Figure 6-8, where a superimposed local coordinate system was used to evaluate the stress distribution. Results are presented in Figure 6-9 for the round and square fillet cases. Both the XX and ZZ components of stress may be observed to decrease non-monotonically. Linearization of these components would therefore violate the guidelines. Similarly, the through-thickness component (YY) does not increase monotonically. It does however meet the surface stress requirements, and may still be linearized if the resultant membrane stress is small.

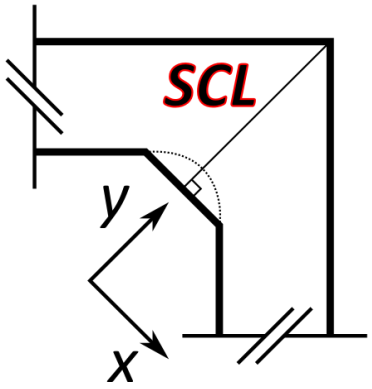

Figure 6-8: Illustration of a diagonal SCL and weld bead configuration

6.1.3 Concluding remarks

Care must be taken when implementing the method of linearization in the vicinity of a weld toe, so as to meet the necessary guideline requirements, especially when it is modelled as being sharp. This

makes the method unattractive for complex problems, since the most critical locations frequently go hand in hand with violation of the guidelines. In view of this, the ASME code [5] does offer two alternative approaches, including limit-load and elastic-plastic stress analysis. They are however outside of the scope of the present study. In future, these avenues could also be explored as a means for developing less conservative designs. This was for example illustrated by Diamantoudis and Kermanidis [19] for a cylinder-to-nozzle junction. A further alternative could be to implement linearization on a model using small strain plasticity. Doing so, singularities could be mitigated through forming small plastic zones, although this still implicates a potentially costly iterative routine for analysis.

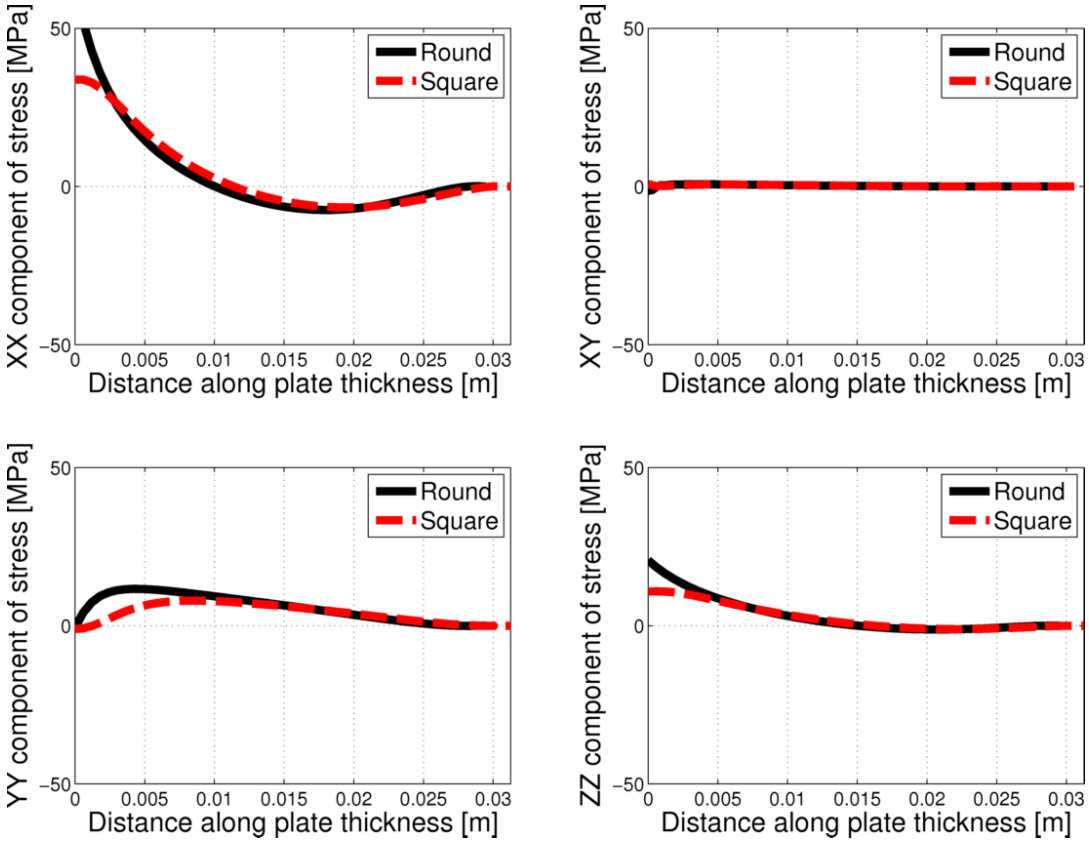

Figure 6-9: Component stress distribution for skewed SCL at junction of example model

6.2 Finite element model of the representative header box

In this section the details surrounding the finite element model of the example header box, excluding a nozzle attachment, are elaborated upon.

6.2.1 Geometry, boundary constraints and material properties

The header box geometry is convenient in the sense that symmetry may be enforced to reduce the size of the model. Observing Figure 3-1, symmetry may be invoked about the XZ and YZ plane. Depending on the nature of the loading and constraints, it would therefore be possible to evaluate a quarter-symmetry model. Although the operating pressure load allows for this, the same cannot be said for external loading associated with a nozzle attachment.

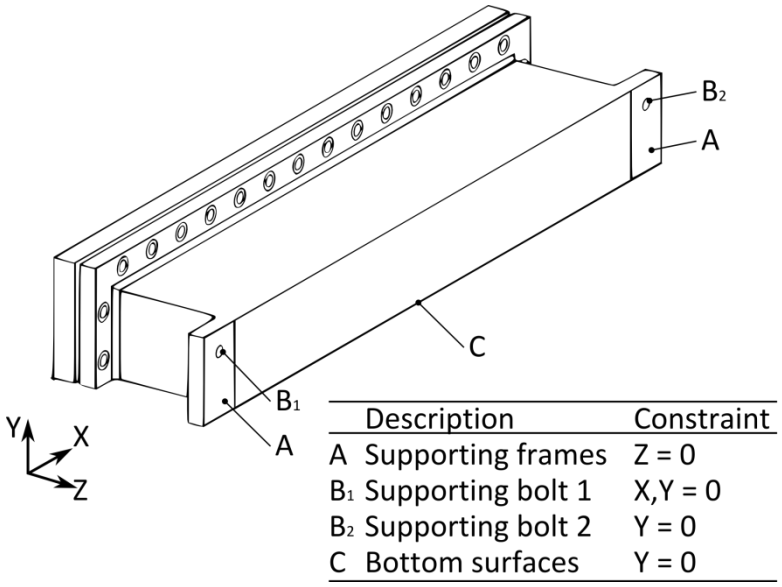

	Description	Constraint
A	Supporting frames	Z = 0
B_1	Supporting bolt 1	X,Y = 0
B_2	Supporting bolt 2	Y = 0
C	Bottom surfaces	Y = 0

Figure 6-10: Header box geometry, excluding nozzle attachment, and boundary constraints

Ultimately, it was decided to evaluate the header box as a half-symmetry model, split along the horizontal (XZ) plane (see Figure 6-10), since it allows for the preliminary investigation of nozzle attachment and loading subject to a few underlying assumptions dealt with in Chapter 8. This reduction also resulted in a manageable linear elastic model, which mitigated any requirements for further computational savings. To enforce half-symmetry, a displacement constraint is placed on all of the bottom surfaces lying within the XZ plane (set Y displacement to zero).

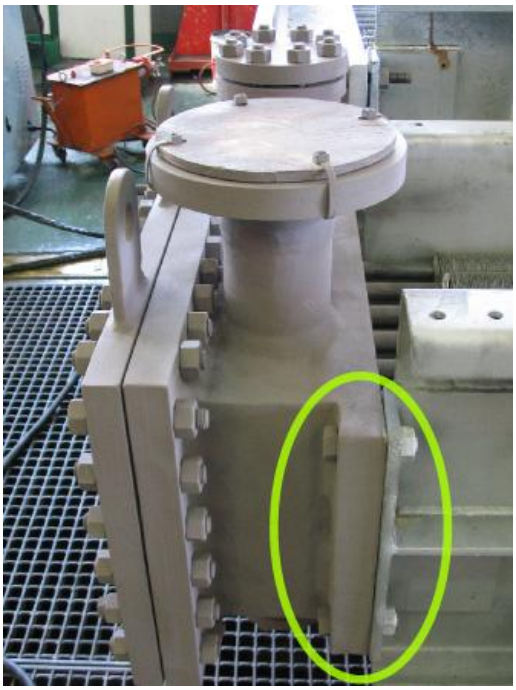

Figure 6-11: Example of header support attachment

The header box is supported by frames on either side that are connected by a number of cross members, also supporting the tube bundle. The header box is simply bolted onto these side frames as depicted in Figure 6-11. To represent this connection in the finite element model some simplifying

assumptions were made and enforced as displacement constraints. The vertical surfaces on either side of the tube sheet in Figure 6-10 were prohibited from moving along the Z-coordinate only. The bolt holes were furthermore held in position along the Y-coordinate, but left free to move relative to one another along the X-coordinate. The reasoning behind this is that very little support is provided against deformation along the X-coordinate by the side frames since the supporting cross members are spaced at large intervals. Importantly, this collection of constraints is also not in violation of the half-symmetry assumption.

6.2.1.1 Representation of the seam welds for the construction of the header box bonnet

A header box represents a collection of plates welded together in a specific form, as depicted in Figure 6-12. The representation of the corresponding weld beads in the finite element model were selected based upon consideration of the header box geometry in its manufactured state, as well as guidelines presented in the ASME code [5]. Details specific to the junctions formed by the flat plates of the header box bonnet are presented in Figure 6-13 [5].

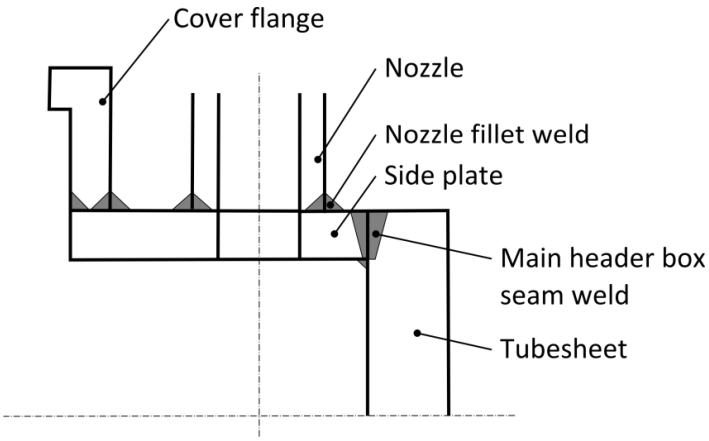

Figure 6-12: Cover type header box weld layout

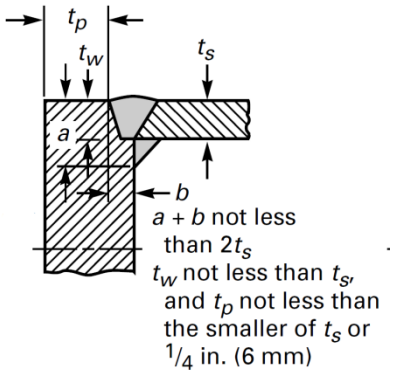

Figure 6-13: Corner junction representation of flat plates [5]

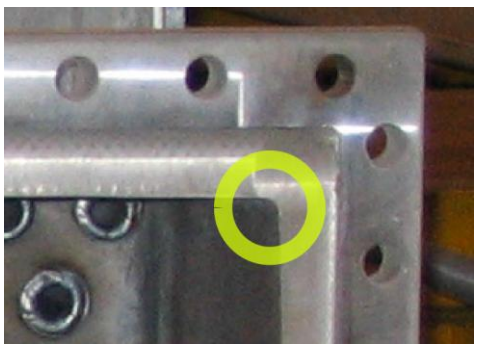

Figure 6-14: Typical internal corner junction

Although the weld bead in Figure 6-13 is ideally square, it is manufactured to be nearly flush with the plates in practice (see Figure 6-14). This is to say that the weld bead more closely represents a round fillet. To accommodate this smooth representation, it was decided to model the weld as being a round cut-out of the ideal square case (see Figure 6-8). In other words, material is removed so as to represent a smooth quarter circle, effectively weakening the junction formed by the flat plates. Not only does this serve the purpose of more closely representing the actual weld, it also mitigates

any influence of singularities in the finite element model. For this purpose, the typical throat thickness of the ideal case (6 mm) was utilised.

6.2.1.2 Material properties

This section serves as a summary of the range of materials used to model the header box, and their associated properties. Details are presented in Table 6-5.

Table 6-5: Material properties of the finite element model

Material	*E (GPa)*	*Poisson's ratio*	*Associated geometry*	*Assumed behaviour*
SA-193 B7	200	0.30	Bolts	Isotropic
SA-516 Grade 60 N	189	0.33	Bonnet and cover-plate	Isotropic
Reinforced graphite	0.95	0.30	Gasket	Isotropic

The characteristics of the bolt material were selected to be the same as for a study performed by Jeong et al. [20], and are typical of steel. Further properties of the header box bonnet and cover-plate material were identified from Section II of the ASME code [5], at the operating temperature of a typical header box. In this respect, it is important to note that an assumption of a uniform material property is used, in spite of the welded construction. This is justifiable, seeing as header boxes are subjected to extensive post-weld heat treatment, and the primary interest lies with the global behaviour of the structure.

Finally, the gasket material is assumed to be isotropic linear elastic. Seeing as a relatively large three-dimensional model is to be evaluated, it becomes difficult to take account of a non-linear material property, and further complex contact behaviour. The Young's modulus assigned for this purpose in Table 6-5 was identified from material data sheets typical of a reinforced graphite gasket [21]. Gaskets of this type are earmarked as having exceptional ranges of pressure and temperature applicability. Since no Poisson's ratio was available for this material, a value of 0.30 was selected and evaluated by means of a sensitivity study, the results of which may be observed in Section 6.2.4.2.

6.2.2 Modelling of the rectangular flange, bolted joints and gasket

To obtain a truly representative model, the header box geometry must be evaluated in its designed state. It is therefore required to adopt a modelling technique capable of adequately portraying a bolted joint in a three-dimensional environment. A study conducted by Jeong et al. [20] investigated four different approaches to address this problem, including: a solid bolt model; a coupled bolt model; a spider bolt model; and a no-bolt model. Of the four, the solid bolt model was found to most accurately predict the physical behaviour of an experimental structure. This bolt model however implies three-dimensional solid elements and surface-to-surface contact elements to represent a joint. It therefore imposes a substantial computational requirement. In light of the relatively large model to be evaluated for the header box geometry, it would be best to implement a more efficient technique. Jeong et al. [20] in fact recommend the use of the coupled bolt model for exactly this circumstance in view of results obtained for a static analysis, as is the case here.

6.2.2.1 Coupled bolt model

In this model, the stud of the bolt is represented by a single beam element, and the nodes corresponding to the head or nut are connected by means of a degree-of-freedom (DOF) coupling. An illustration is included in Figure 6-15, where the DOF coupling is achieved via rigid multi-point-constraints (MPCs).

For DOF coupling, the face of the nut is constrained in the longitudinal sense, i.e. the DOF normal to the flange face. This effectively approximates a scenario of zero friction between the nut and flange surface, whereby the flange is allowed to deform freely. It would be inadvisable to further constrain the concerned nodes within the plane of the flange face, since it would provide extra rigidity. To then also ensure that the stud remains at the centre of the bolt hole, it is restricted from relative motion within the nut-to-flange interface. Since three distinct motions are possible within a two-dimensional plane (two translations and one rotation), three DOF couplings are required to achieve this (see Figure 6-16).

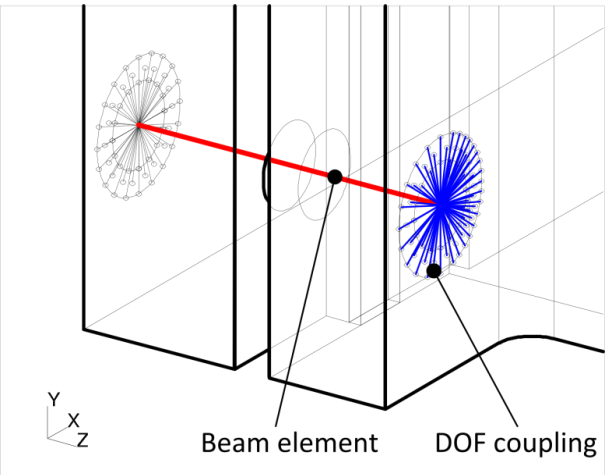

Figure 6-15: Coupled bolt model illustrated on the header box geometry

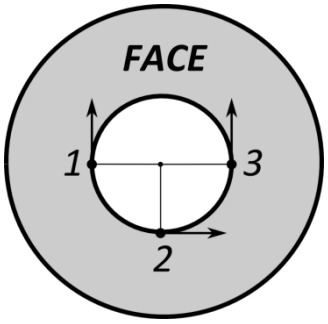

Figure 6-16: Constrained DOF to maintain stud in central position

6.2.2.2 Bolt pre-tension in the three-dimensional model

Two important features accounted for by the bolts include pre-tension and resistance to further tensile loading. In the coupled bolt model, pre-tension can be simulated by imparting an initial strain onto the beam element representing the stud. This may for example be achieved via the application of a temperature difference. However, since the equivalent stiffness of the header structure is complex, finding the correct temperature difference for a specific arrangement of bolts presents a nontrivial task. The fact that a linear elastic analysis will be performed however simplifies matters because the principle of superposition may be employed.

The location of the bolts for the example model may be observed in Figure 6-10, where each of the beam elements, representing the studs, must be subjected to the same pre-tension, i.e. axial stress. This implies that a distinct initial strain must be imparted to each bolt. The corresponding temperature differences may be solved for from an implicit expression involving a proportional relationship between the axial beam stress and concurrent temperature differences.

Generally, the normal strain in a body is predicted as being linearly proportional to an applied temperature difference. It is only when this body is met with restraint that the ensuing normal strain may be used to evaluate an axial stress via Young's modulus. For the header box, restraint implicates influences from all the other bolted joints, as well as the structure itself. What is more, any initial strain imparted to a bolt or collection of bolts also influences the resultant stress of the remaining bolts. Fortunately, the principle of superposition states that for a linear analysis, the net response at a given location caused by two or more stimuli is the sum of the responses caused by each stimulus individually. Therefore, the axial stress of a specific bolt may be ascribed to the sum of the influences of all of the bolts. Further noting that the influence of a bolt may be accepted as being linearly proportional to an applied temperature difference, the relationship shown in Equation (6-5) can be deduced. It is also important to note that since heat transfer characteristics can be considered irrelevant to the present study, each beam element may be provided with an arbitrary thermal expansion coefficient in the finite element model.

$$S_i = \sum_{j=1}^{N} C_{ij} \left(\Delta T\right)_j \tag{6-5}$$

The following applies:

S_i = Normal stress at bolt i
C_{ij} = Constant relating normal stress at bolt i to the temperature difference at j
$\left(\Delta T\right)_j$ = Temperature difference at bolt j
N = Total number of bolts

The coupling constants (C_{ij}) may be solved for via the discrete perturbation of the individual bolts, i.e. application of an arbitrary temperature difference, whereby the subsequent stress at bolt i may simply be divided by the perturbation temperature at bolt j. This can prove to be quite tedious for larger models, since as many analyses as there are bolts are required. Once all of the coupling constants have been identified, Equation (6-5) may be expressed in a collective form via matrix notation as in Equation (6-6). Hereafter, an arbitrary selection of axial bolt stresses may be solved for via matrix inversion as in Equation (6-7).

$$\{S\}_{N\times 1} = [C]_{N\times N} \{\Delta T\}_{N\times 1} \tag{6-6}$$

$$\{\Delta T\}_{N\times 1} = [C]^{-1}_{N\times N} \{S\}_{N\times 1} \tag{6-7}$$

6.2.2.3 Modelling assumptions for the gasket

In addition to the linear elastic material properties assigned to the gasket in Table 6-5, a state of permanent contact is assumed to exist between the gasket and header box structure. This is not expected to influence the global behaviour of the header box too greatly, since the gasket will in any case be shown to be completely sealed (under compression) for the example problem. Seeing as the model is relatively large, it would be difficult to take account of a non-linear material property, and

further complex contact behaviour. Under these circumstances, the application of bolt pre-tensioning would also be made substantially more difficult.

6.2.3 Mesh generation and adequacy of the results

6.2.3.1 Mesh generation

The header box geometry was meshed using ten-node tetrahedral (TET10) elements. Intuitively, it can be considered best-practice to implement three-dimensional solid elements because of the relatively thick plates used for the header box, especially when considering that a side plate length to thickness ratio of approximately six and a half may be identified from the example model. TET10 elements in particular have successfully been used in numerous studies, a noteworthy example of which is Choi et al. [22], where shape optimization of a perforated pressure vessel cover was performed using linearized constraints. This element type may also be considered particularly advantageous since it simplifies meshing, and allows for automatic implementation if care is taken.

With application to the example problem, two levels of mesh refinement were evaluated. For each case local refinement was also performed based on intuitive judgment of the stress distribution. This was achieved through simply imposing a smaller element edge length on the round fillet surfaces representing the seam welds of the bonnet. The element edge length for the two levels of refinement is illustrated in Table 6-6, the case of the finer mesh being half that of the coarse mesh.

Table 6-6: Element edge lengths for two levels of refinement

	Coarse mesh	*Fine mesh*
Seam weld surfaces	4.50 mm	2.25 mm
Header bonnet and cover-plate	20.00 mm	10.00 mm
Gasket	5.00 mm	2.50 mm

6.2.3.2 Gasket seating condition

It is important that bolt pre-tensioning be sufficient to seal the gasket for both the seating and operating conditions. To establish this, the method described in Section 6.2.2 was implemented in conjunction with observations from an example finite element design of a large rectangular flange (Batra, [12]). In this design [12], the whole of the gasket surface area is observed to be under compression at an adequately high level of stress.

For the example header box, the method of bolt pre-tensioning was implemented solely for the coarse mesh, since it provided results of sufficient accuracy for implementation on the fine mesh. It is also important to note that through observation of Figure 6-10, the layout of the bolts may be identified as being symmetrical about the YZ plane. This allowed the number of evaluations to construct a coupling matrix (see Equation (6-6)) to be halved by perturbing the bolts in pairs (located symmetrically about the vertical plane) and dealing with them in unison.

The axial stress of each of the bolts in the seated condition was uniformly set equal to the minimum recommended value for pre-tension of 172.4 MPa [12]. The beam elements representing the studs

of the bolted joints were furthermore modelled as having the major diameter (d_b = 19.05 mm) described in Table 3-1. This is in contrast to the current practice calculations of Chapter 4, where the root diameter is used. This increase in cross-section has the effect of generating a larger bending moment (M_{jw}). To compensate for this, appropriate adjustments are made for the results comparison in Chapter 7. It is also important to note that the increase in tension based on the major diameter would not result in the maximum recommended value, 413.7 MPa [12], being exceeded when applied to the root diameter.

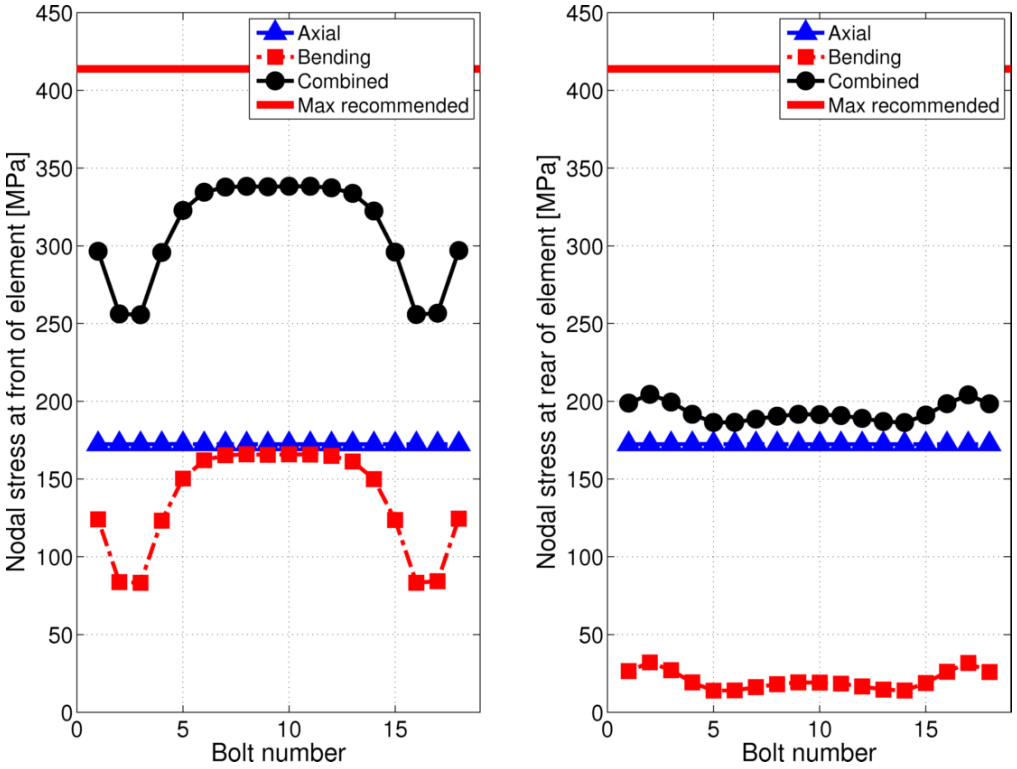

Figure 6-17: Bolt stress distribution in the coarse mesh subject to gasket seating load (pre-tension) only

The resultant axial and bending stresses experienced at either end of the beam elements representing each stud were subsequently extracted for the coarse mesh, and plots constructed (see Figure 6-17 and Figure 6-18). In the figures, the front end of the bolts is associated with the positive Z-coordinate in Figure 6-10, and the rear end with the opposite. The bolts are furthermore numbered in a clockwise fashion with reference to Figure 6-10. Bolt 1 and 2, and 17 and 18 are therefore oriented vertically on either side of the header box. The remainder are located horizontally at the top.

Upon inspection of the gasket seating results (see Figure 6-17) the axial stress experienced by each of the bolts can be identified as falling within a range of 0.04 % of the desired 172.4 MPa. This deviation is a consequence of using a limited number of digits for computing bolt temperatures. The addition of pressure loading (see Figure 6-18) can be observed to incur a small change in the uniform stress distribution of the bolts. The superimposed bending stress is a consequence of the rotation of the flange and the nature of the DOF coupling used for the bolt model. It was observed to vary linearly along the length of each bolt element upon further refinement. Knowing that an error is made by approximating the connection of the bolted joints to the header box in this manner an effort was made to establish some measure of sensitivity for the global stress distribution. To this

end, the beam elements were replaced with rod elements (capable of resisting tensile load only) so as to eliminate moment resistance. A comparison is presented in Section 6.2.4.1. The interim content relies on the original modelling technique.

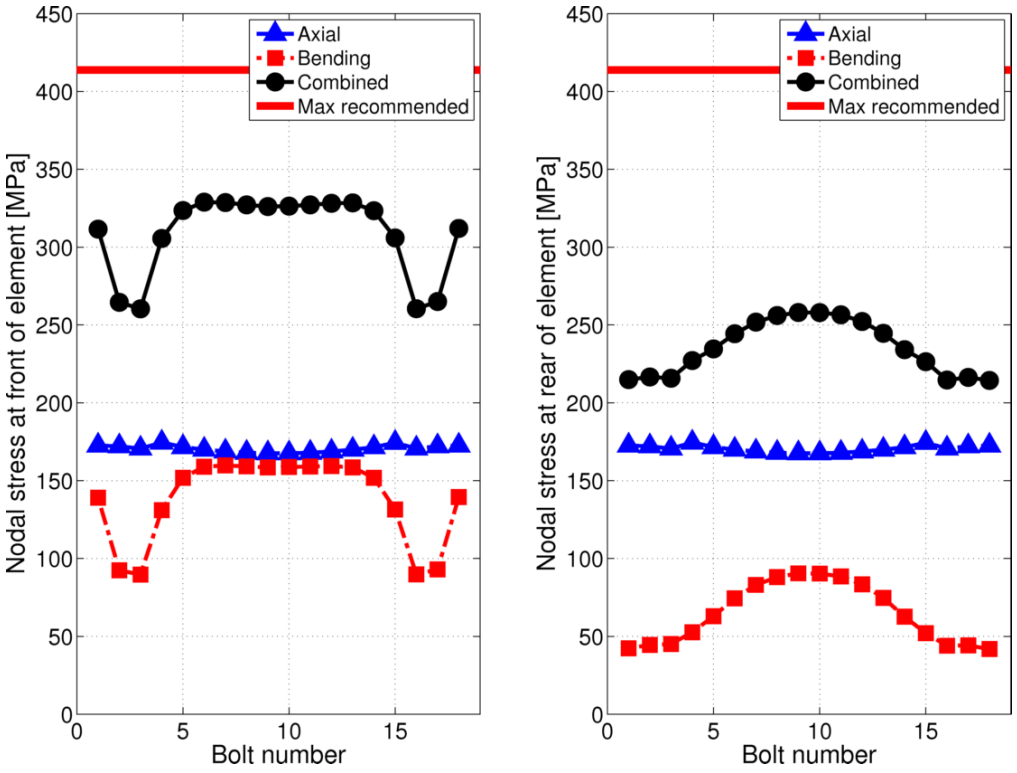

Figure 6-18: Bolt stress distribution in the coarse mesh subject to pre-tension and 1 MPa internal pressure loading

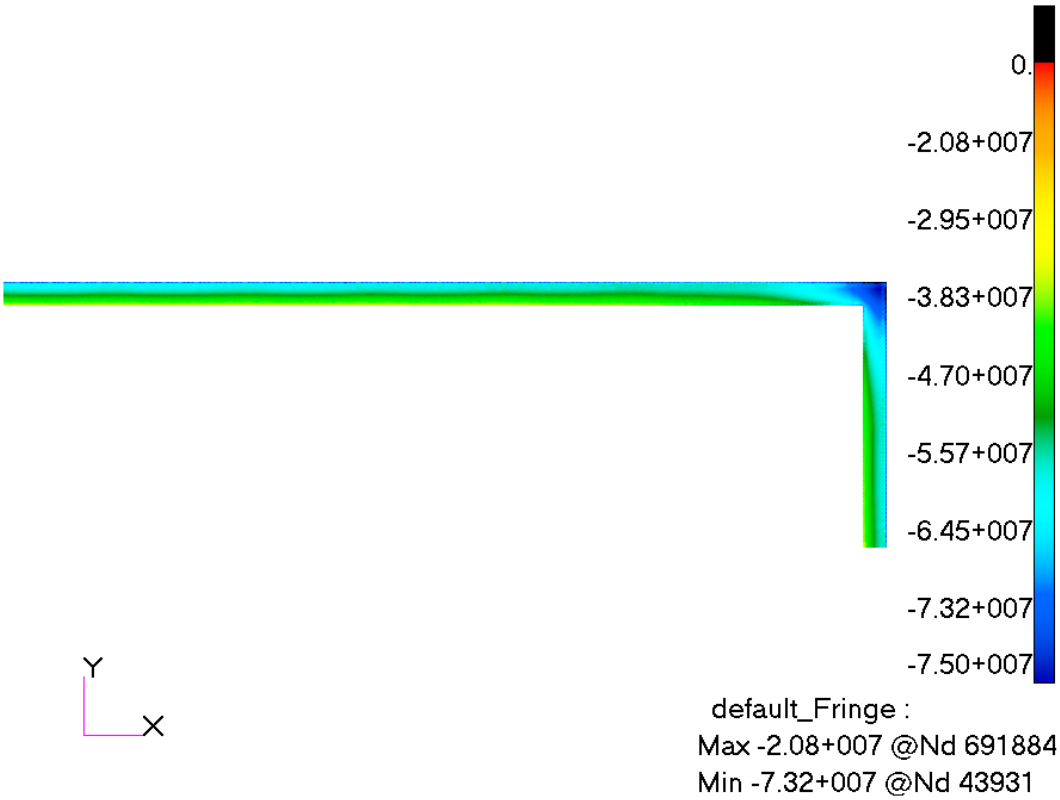

Figure 6-19: Quarter of the rectangular gasket in its seated condition

As suggested, the same temperature differences used for the coarse mesh were applied to the fine mesh, so as to save computational expense. This resulted in the axial stress of all of the bolts falling within 0.46 % of the minimum recommended pre-tension, which is adequate for drawing comparisons between the two levels of refinement. It may further be noted that far greater deviations from a uniform bolt preload distribution may be expected in reality due to the complications of bolt interaction.

The compressive stress imposed upon the gasket as a result of the gasket seating and operating conditions are also portrayed in Figures 6-19 and 6-20 respectively. For both cases, the whole of the gasket may be observed to be sealed, which supports the assumption of fixed contact. It may further be noted that in the seated condition, the circumference of the gasket is sealed at a stress above the minimum recommended value (y = 17.24 MPa from Table 3-1).

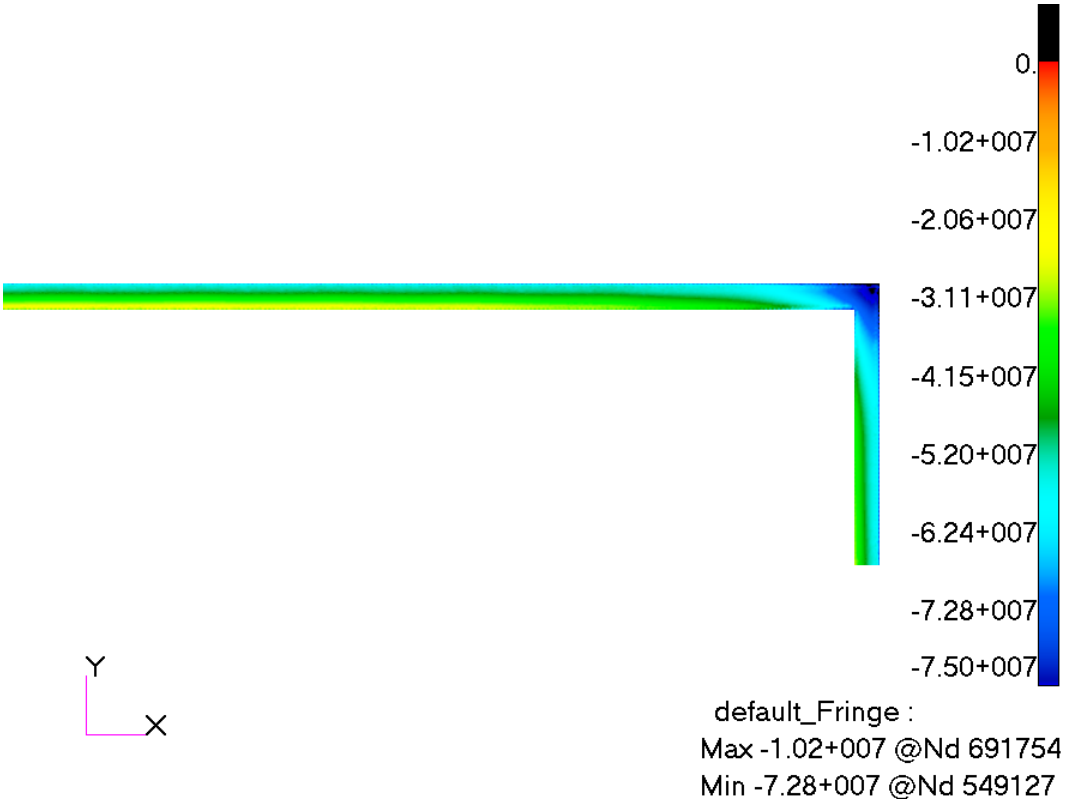

Figure 6-20: Quarter of the rectangular gasket subject to operating conditions

6.2.3.3 Mesh independence and header box stress distribution

In order to compare the results for the finite element model with that of the analytical methods in Chapters 4 and 5, it is necessary to extract and linearize the resultant global stress distribution appropriately. To do so, the normal component of stress corresponding to the global Z-coordinate for the side plate, and the global Y-coordinate for the tube sheet must be evaluated (see Figure 6-21). These components will be referred to as the hoop components.

For extraction, six uniformly spaced SCLs were identified along each of the plates at the centre of the header box's width. This is demonstrated by Figures 6-21 and 6-22, where linearization is performed by means of the Simpson's rule implementation. To ensure the accuracy of the linearized results, the

number of uniformly spaced points per SCL was first varied. Results for the linearized equivalent membrane plus bending stress of each SCL along the side plate may be observed in Table 6-7, with reference to the gasket seating condition. The guidelines for linearization were adhered to throughout, and since an equivalent value is being calculated all of the stress components contribute towards the result.

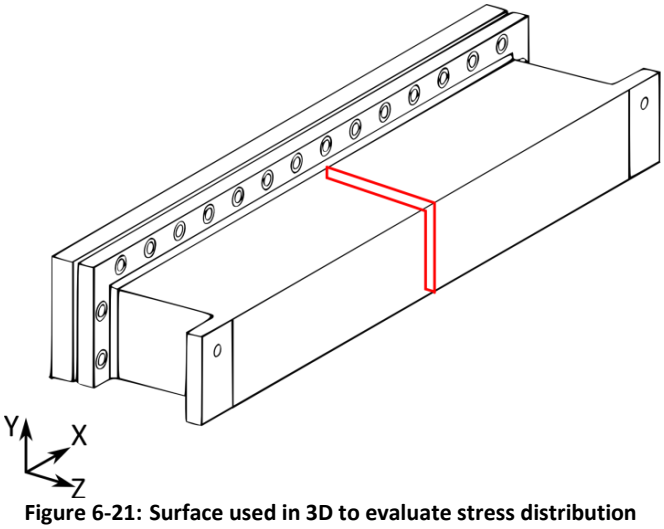

Figure 6-21: Surface used in 3D to evaluate stress distribution

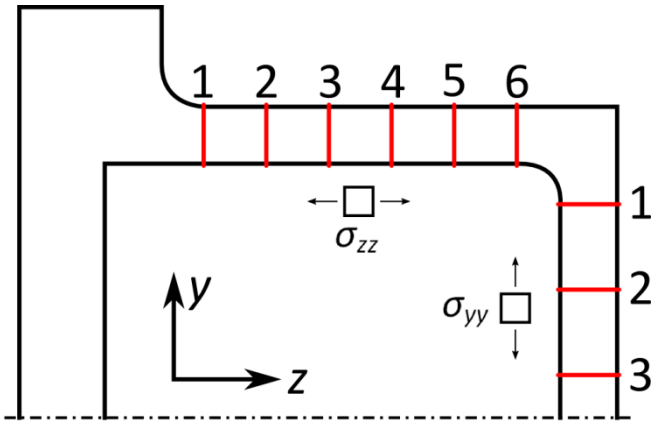

Figure 6-22: SCLs used for analogized hoop stress

From Table 6-7, convergence to a single decimal position may be observed for each of the SCLs at 15 points. As a precautionary measure, the number of points used in the analyses to follow was however selected to be 21.

Table 6-7: Maximum equivalent Von Mises stress [MPa] for each SCL along the side plate (coarse mesh)

SCL	*1*	*2*	*3*	*4*	*5*	*6*
9 points	74.0	54.2	39.3	24.9	10.0	7.3
15 points	73.9	54.2	39.3	24.9	10.0	7.3
21 points	**73.9**	**54.2**	**39.3**	**24.9**	**10.0**	**7.3**
27 points	73.9	54.2	39.3	24.9	10.0	7.3

To subsequently establish adequate refinement of the finite element model (i.e. convergence), the hoop components from the side plate and tube sheet were evaluated for two loading scenarios. The one scenario is for the gasket seating condition, whereby only bolt pre-tension is applied, and the

other scenario is for the operating condition, whereby a 1 MPa pressure load is superimposed on all of the internal surfaces. The linearized membrane and bending stress solutions for each of these cases may be observed in Figures 6-23 and 6-24 at both the coarse and fine refinement levels.

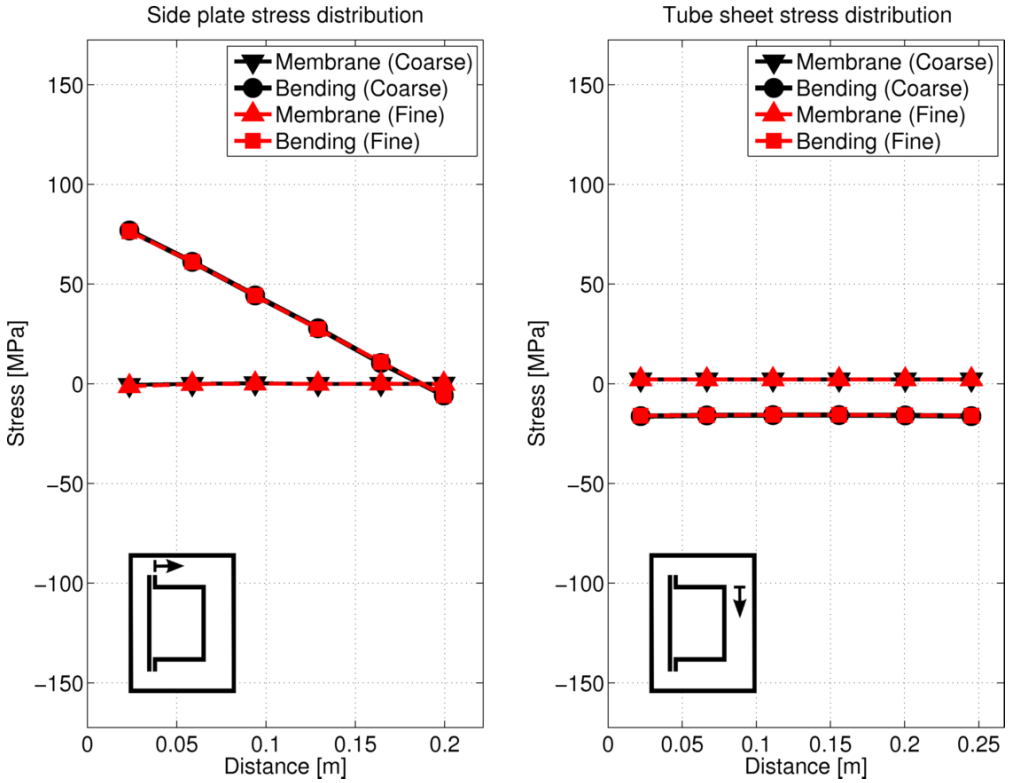

Figure 6-23: Hoop component stress distribution for gasket seating load

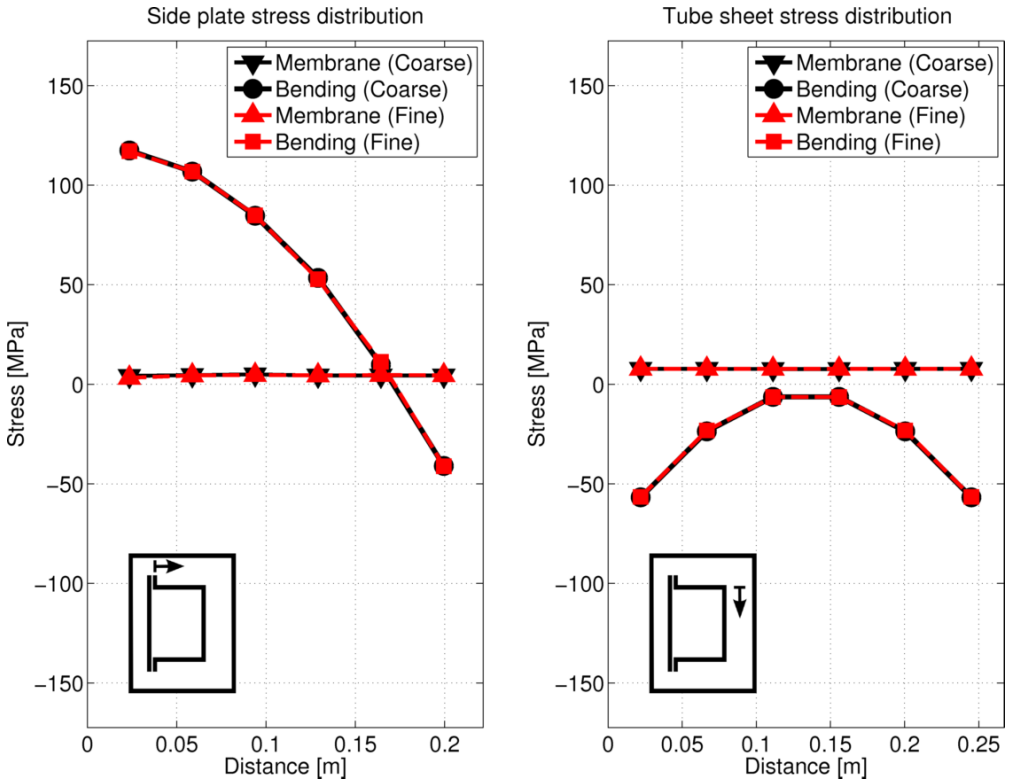

Figure 6-24: Hoop component stress distribution for superimposed 1 MPa pressure load

The good correspondence between the results in Figures 6-23 and 6-24 may, in part, be ascribed to the efficiency of the method of linearization since it relies upon the global stress response.

As a measure of convergence, the combined (membrane plus bending) stress resulting at SCL 1 on the side plate (see Figure 6-22) was also given closer inspection. Results are provided in Table 6-8. In both load cases, the percentage change in the result is below 1 %, which is acceptable for the intended comparisons.

Table 6-8: Comparison of linearized hoop bending stress component (σ_{zz}) at SCL 1 for two levels of mesh refinement

Loading condition	*Coarse mesh*	*Fine mesh*	*Percentage difference*
Gasket seating	76.85 MPa	76.43 MPa	**-0.54 %**
Operating	117.39 MPa	117.02 MPa	**-0.31 %**

6.2.4 Sensitivity studies

In this section, two aspects of the finite element model are investigated more closely. Namely: the moment resistance arising from the method of DOF coupling in the bolt model; as well as the value for Poisson's ratio given to the gasket material. It is important that their influence on the global stress distribution be examined.

6.2.4.1 Bolt coupling method

To gain understanding of the significance of the moment resistance presented by the coupled bolt model, it was decided to evaluate a scenario which disregards it, for comparison. In this approach, the beam element representing the stud of the bolt is replaced with a rod element capable of resisting tensile load only. It is further important to note that the method of bolt pre-tensioning remains valid for this approach, where the stud elements were loaded to the same pre-tension as before.

Table 6-9: Comparison of linearized stress (σ_{zz}) resulting at SCL 1 for two bolt modelling approaches

Stud element type	*Bending stress (MPa)*	*Percent difference (%)*
Gasket seating condition		
Moment-resisting beam	76.43	0.0 %
Rod element	82.47	+ 7.9 %
Operating condition		
Moment-resisting beam	117.02	0.0 %
Rod element	124.05	+ 6.0 %

Results for the linearized σ_{zz} bending stress at SCL 1 on the side plate (see Figure 6-22) may be observed in Table 6-9. This location presented the largest absolute difference in bending stress between the respective modelling cases. The rod element scenario may be observed to result in a higher bending stress for both of the loading conditions. The respective increases are within 8 % of the original bolt modelling case. Plots of the global stress distributions may also be observed in Figures 6-25 and 6-26.

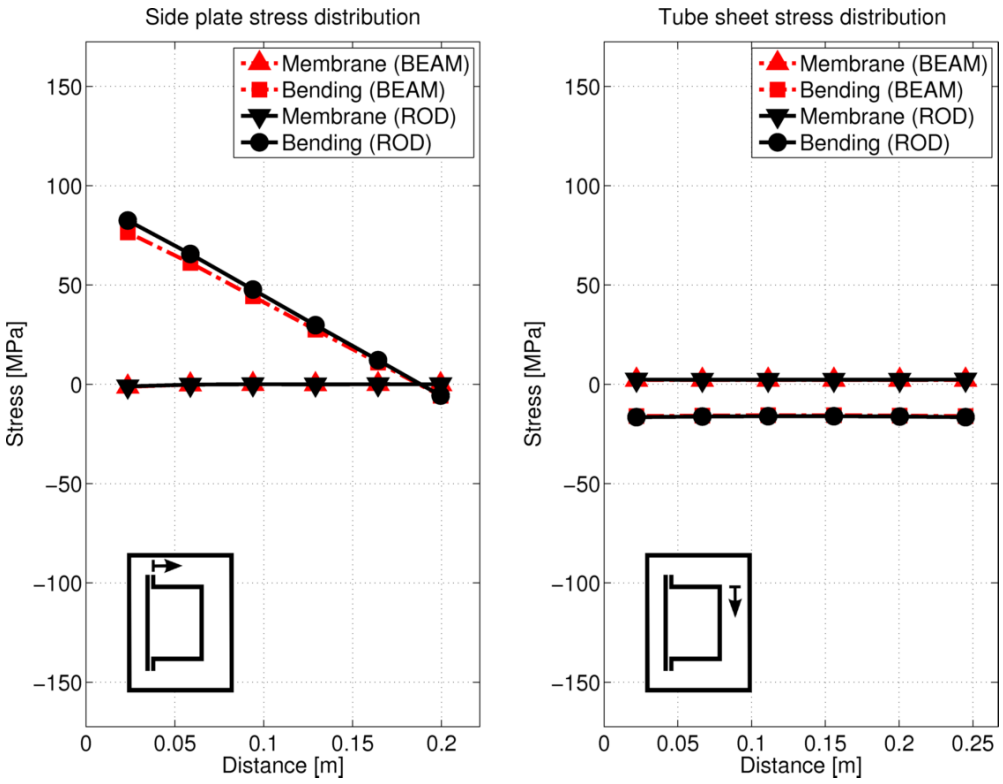

Figure 6-25: Global stress distribution for two different approaches to bolt modelling (seating condition)

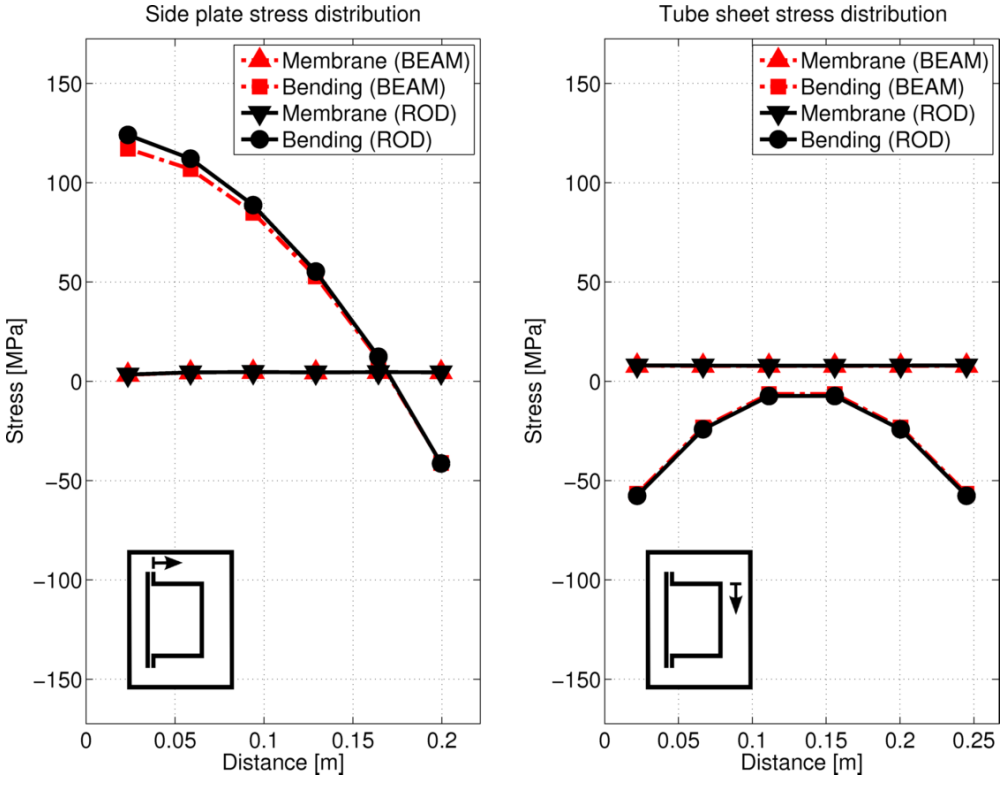

Figure 6-26: Global stress distribution for two different approaches to bolt modelling (operating condition)

6.2.4.2 Poisson's ratio and the gasket material

For the purposes of this section, the original bolt modelling technique (i.e. beam element representation) was implemented.

Table 6-10: Comparison of stress resulting at SCL 1 for varying Poisson's ratios

Poisson's ratio	*Bending stress (MPa)*	*Percent difference (%)*
Gasket seating condition		
0.01	77.39	+ 0.7 %
0.30	76.85	0.0 %
0.49	71.80	- 6.6 %
Operating condition		
0.01	119.96	+ 2.2 %
0.30	117.39	0.0 %
0.49	101.41	- 13.6 %

The global stress distribution was evaluated for three different values of Poisson's ratio assigned to the gasket (0.01, 0.30, and 0.49), in order to assess the sensitivity of the model to this material property. The lowest value of 0.01 approximates a scenario where the gasket would expand very little when compressed, whereas the highest value of 0.49 approximates incompressible behaviour (e.g. rubber). The original value of 0.30 is more characteristic of materials such as steels and rigid polymers. In the case of the header box, a stainless steel reinforced graphite gasket is used.

As in the previous section, results for the linearized bending stress at SCL 1 on the side plate are presented in Table 6-10. Overall bending stress distribution plots are also illustrated in Figure 6-27 and 6-28. From here, reducing Poisson's ratio from 0.30 to a value of 0.01 may be observed to have a smaller net effect than increasing it to 0.49. Importantly however, the increase in Poisson's ratio may be associated with a decrease in the absolute value of stress throughout the distribution. From Table 6-10, the lowest value of 0.01 furthermore only results in increases of 0.7 % and 2.2 % at SCL 1 for the respective load cases.

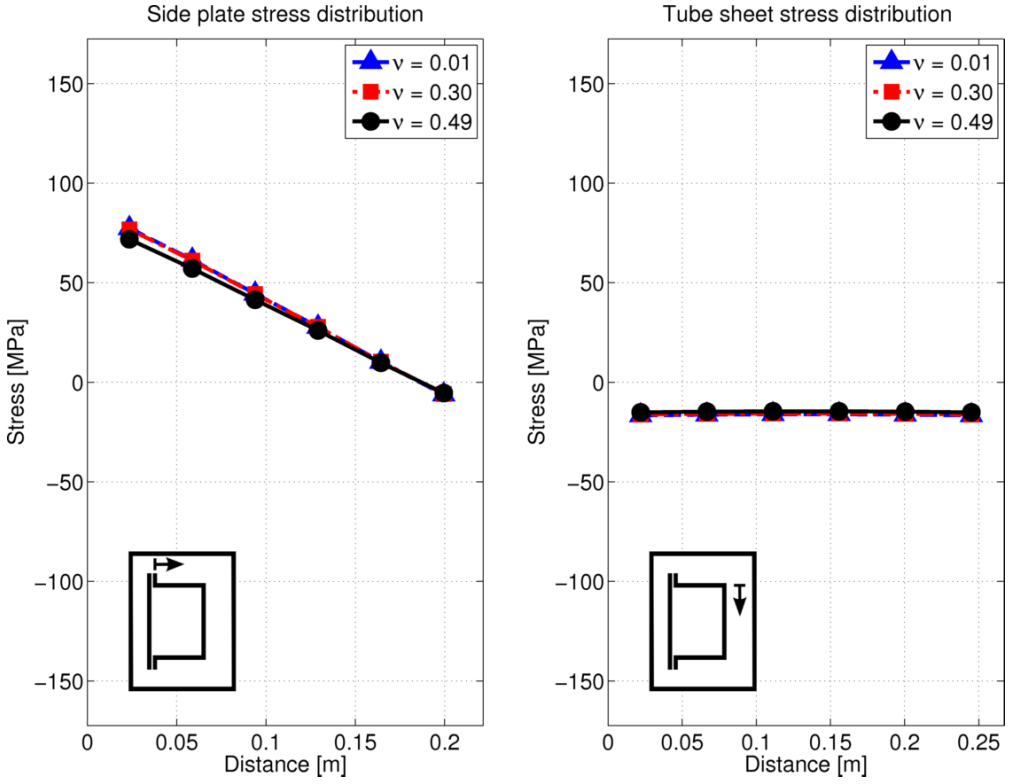

Figure 6-27: Bending stress distribution at varying Poisson's ratios for the gasket material (seating condition)

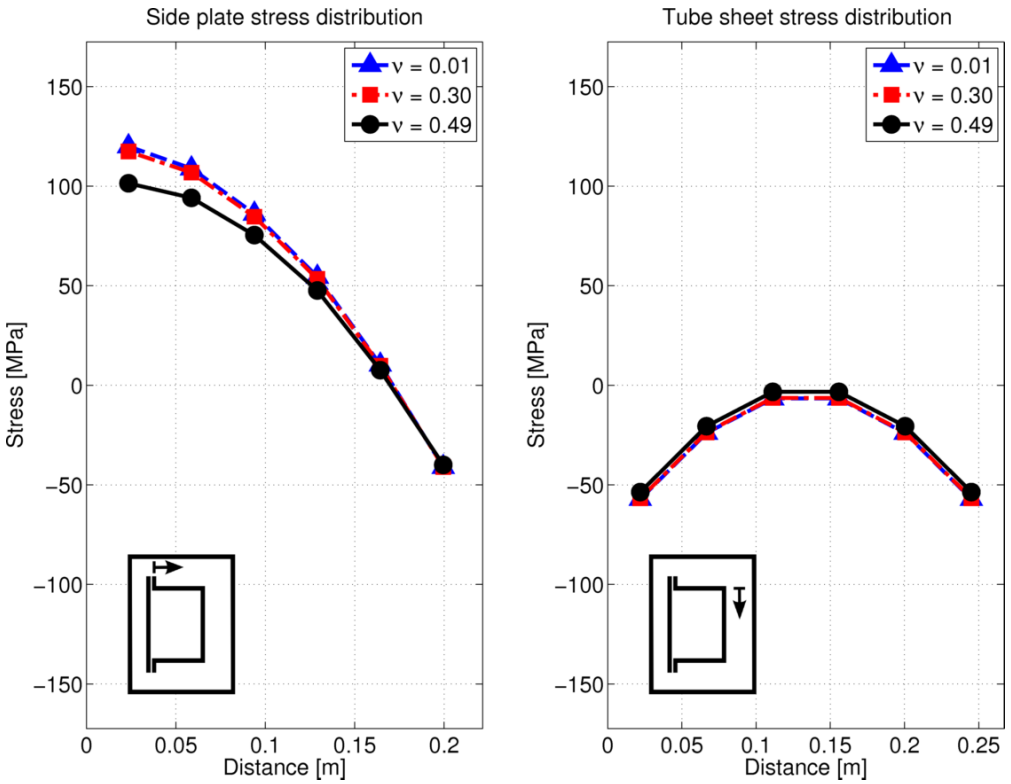

Figure 6-28: Bending stress distribution at varying Poisson's ratios for the gasket material (operating condition)

6.2.4.3 Concluding remarks

In the remainder of this document, the original bolt modelling technique incorporating moment resistance, as well as the Poisson's ratio of 0.30 is implemented. The results of the bolt modelling study indicated acceptable levels of variation. For higher accuracy one would have to model the bolts by means of solid elements with consideration of contact behaviour. Not only does this necessitate a substantial increase in computational expense, but obtaining a uniform distribution for bolt pre-tensioning would become highly complex. Similarly, the value for Poisson's ratio assigned to the gasket material could be observed to have little effect on the global stress distribution, especially for smaller values.

6.3 Observations on the significance of bolt modelling in a practical context

One of the most important features of a finite element model representing a cover-type header box is the large rectangular flange and the accompanying bolted joints, since they have a fundamental influence upon the behaviour of the header box. Unfortunately, design engineers from time to time make simplifying assumptions which fail to represent this appropriately. The purpose of the present section is to demonstrate the significance of full three-dimensional modelling in comparison with two flawed plane strain models.

6.3.1 Plane strain example models

Two scenarios which effectively ignore the influence of bolt loading are elaborated upon below. Note that half-symmetry is enforced in a similar manner to the three-dimensional model.

I. ***Built-in at the flange***: The thickness of the side plates is assumed small in comparison with the cover-plate and flange. The side plates are therefore modelled as being built-in, consequently prohibiting any rotation or translation of the flange joint. This conforms to the rigid frame solution presented on page 48, absent bolt loading of course (see Figure 6-29).

II. ***Unified flanges***: All of the plates are assumed large enough to nullify the influence of the bolted joints and further loading on the global response of the header box. The flanges are modelled as being uniformly joined, with no cognisance taken of the rectangular gasket (see Figure 6-30). This approach may also prove useful in scenarios where the gasket is aligned with the bolt holes (i.e. no bolt induced bending moment is generated).

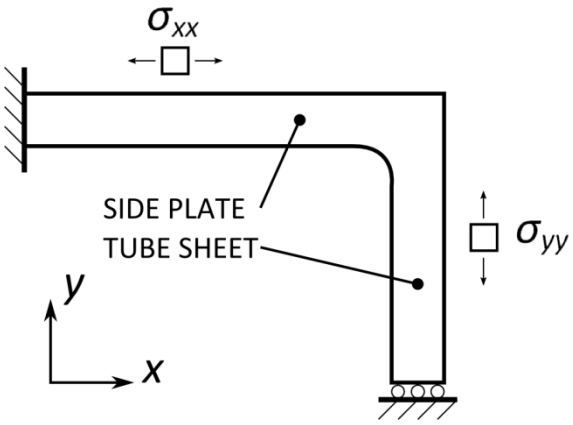

Figure 6-29: Plane strain, built-in at the flange

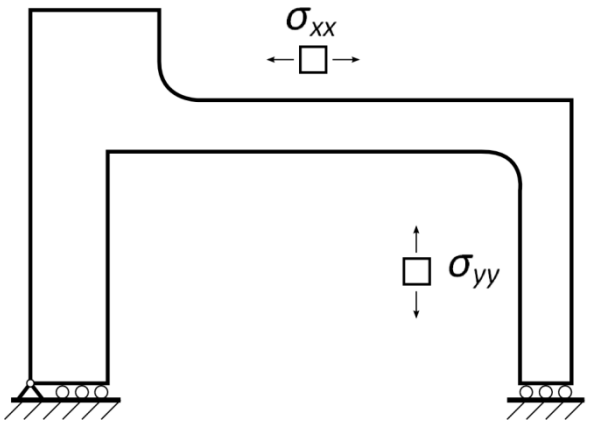

Figure 6-30: Plane strain, unified flanges

6.3.2 Finite element modelling and analysis

The primary characteristics of the finite element models developed for the plane strain examples are listed below.

- All dimensions conform to the representative design in Table 3-1. Since a plane strain analysis is being performed, the header box is effectively modelled as being very long.
- A uniform material property is assigned, as per the header box specifications in Table 6-5.
- Boundary constraints are enforced as per the illustrations in Figure 6-29 and 6-30.
- A 1 MPa pressure load is applied to all the internal edges.
- Eight-node quadrilateral elements were used at a refinement of 32 elements across the thickness of the side plate, twice that of the linearization example in section 6.1.

SCLs spaced at uniform intervals as in Figure 6-22 were evaluated, where the σ_{xx} component along the side plate and σ_{yy} component along the tube sheet were linearized. Results are presented in Figure 6-31, and are compared with the results for the three-dimensional model in Section 6.3.3.

6.3.3 A brief comparison with the three-dimensional model

Since the example plane strain models do not take account of bolts, the contribution of pressure loading alone was extracted from the three-dimensional model for comparison. This is computed by subtracting the gasket seating condition results in Figure 6-23 from the superimposed condition in Figure 6-24. Plots comparing the results for the respective models are provided in Figure 6-32.

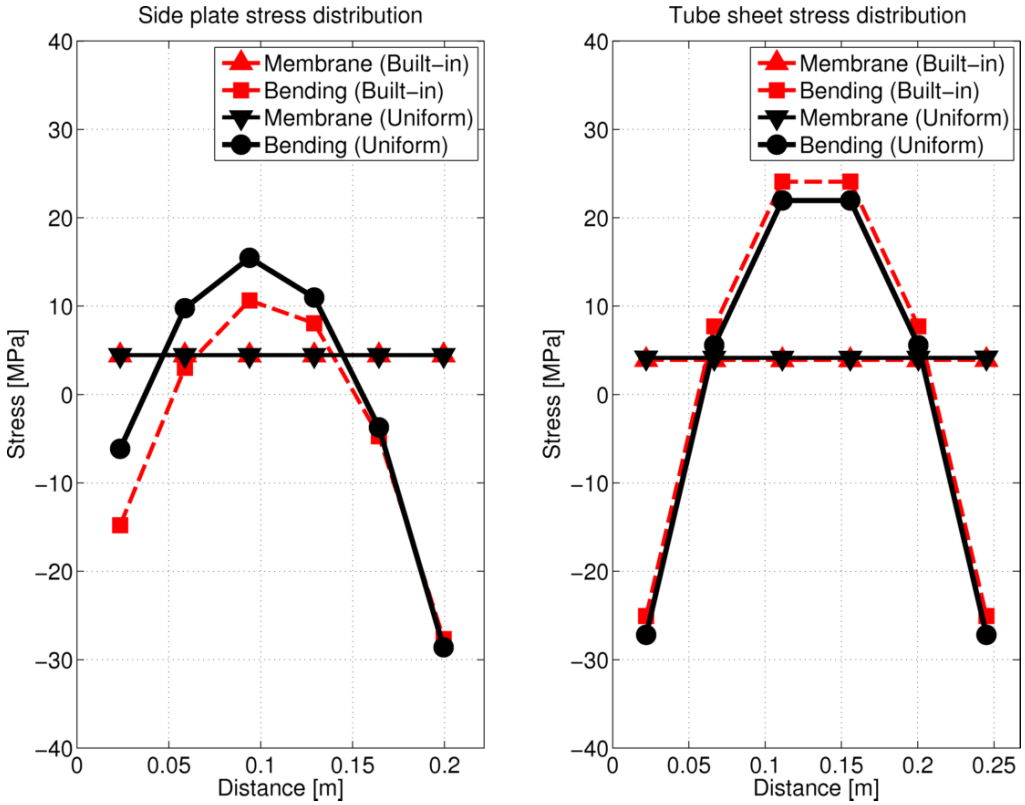

Figure 6-31: Illustration of the membrane and bending stress distributions of the example plane strain models

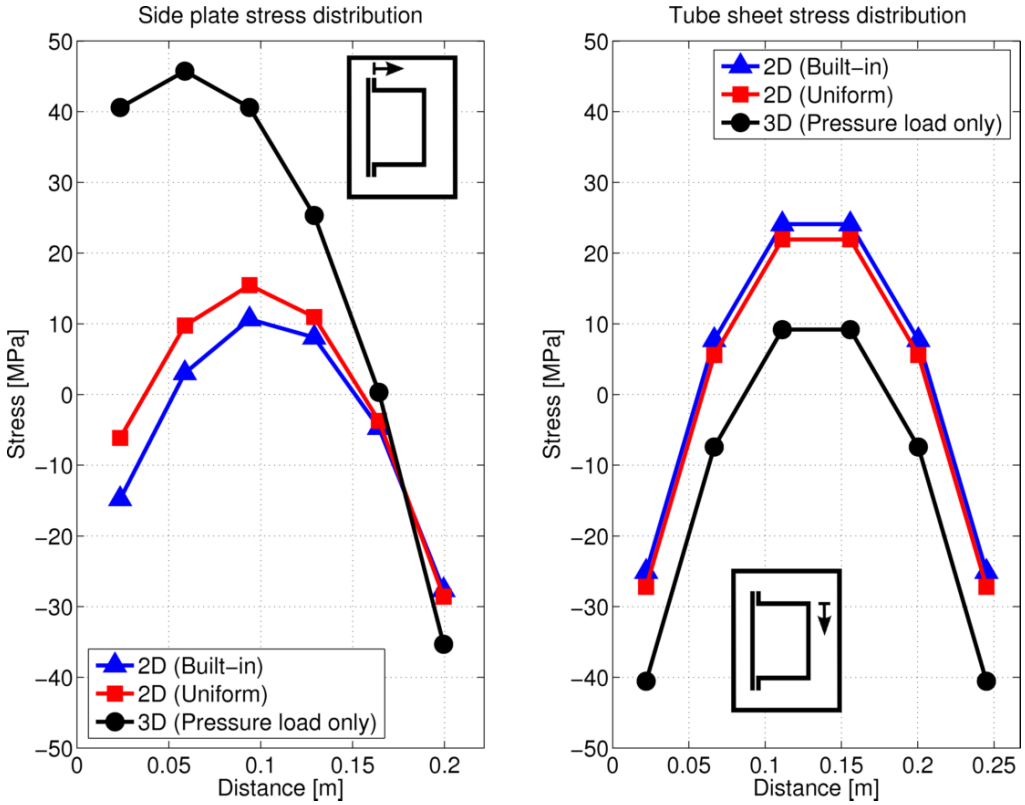

Figure 6-32: A comparison of the bending stress resulting from pressure loading only

The peak bending stress for either of the plane strain models is predicted to occur in the side plate at the joint with the tube sheet. Both cases predict a stress of approximately 28 MPa. The three-

dimensional model predicts a value of 35.3 MPa at the same location, resulting in a difference of about 26 %.

Nearer to the junction with the flange a significant difference exists between the three-dimensional model and the plane strain ones. In this vicinity the plane strain models predict a bending stress of opposite orientation to the three-dimensional model. If bolt loading were to be included into the three-dimensional model, the bending stress would be approximately 117 MPa right at the junction with the flange. The plane strain models on the other hand, would have predicted values of – 6 MPa and – 15 MPa respectively. Consequently, a less conservative result is obtained with the plane strain models.

7 Results comparison and discussion

The header box bonnet's stress distribution is plotted, and used as a tool for comparison between the rigid frame models and the three-dimensional FEM in Section 7.1. In Section 7.2 an additional investigation for the flanged rigid frame model is included. In this case, the bending resistance of the bolt coupling method in the FEM is considered. The capabilities for failure quantification and prediction of each approach are considered in Section 7.3, when the current design approach is also taken into account. Both design by rule, and design by analysis are considered.

7.1 Comparison of the rigid frame models and finite element model

In Figures 7-1 through 7-3 the stress distributions for the respective rigid frame models are plotted in comparison with the finite element model, where it is important to note that the rigid frame results were adjusted appropriately for the increased bolt loading mentioned in Section 6.2 (calculation based on major instead of root diameter of bolt). The results presented in the plots correspond to the case of operating load; pressure loading is therefore superimposed.

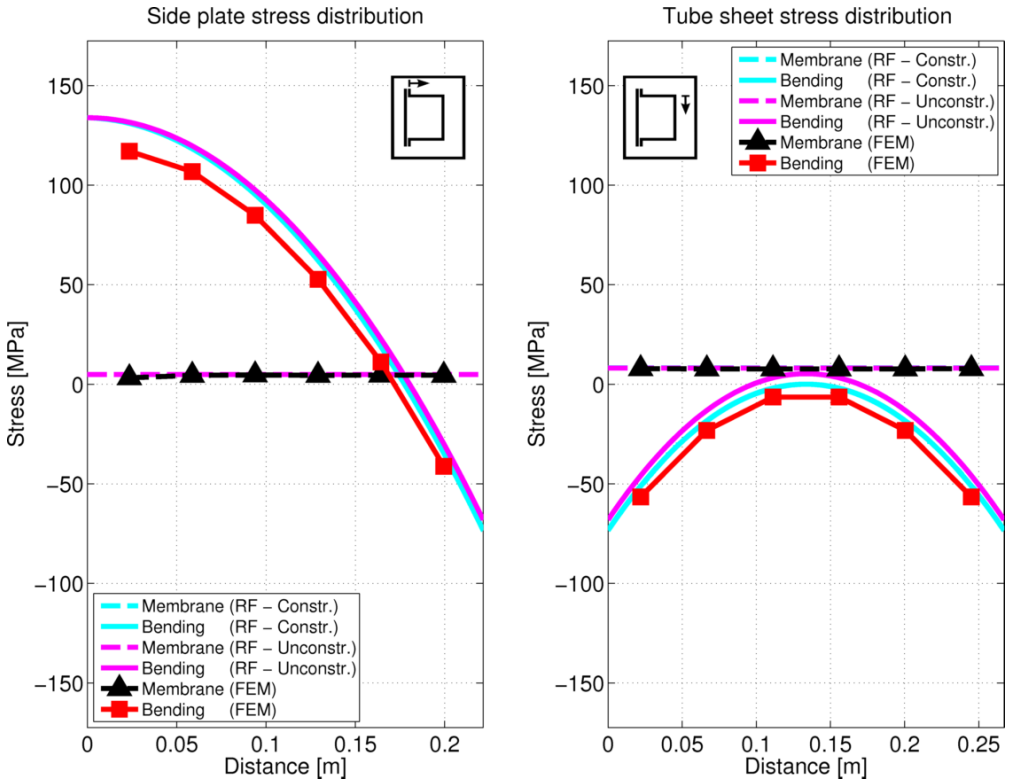

Figure 7-1: Stress distribution of the flanged frame models compared to the FEM for operating load

The resultant membrane and bending stress are presented separately in each of the stress distribution figures. From the FEM solution, the bending stress can be identified to be substantially more significant than the membrane stress. Because of this, the discussions to follow are based on bending stress results, unless stated otherwise.

From the graphs, reasonable correspondence between the finite element model and the flanged frame models and simple frame models having hinged supports can be identified (see Figures 7-1

and 7-2, respectively), whereas the simple frame models having built-in supports provide a visibly poorer result (see Figure 7-3). It therefore becomes a matter of selecting between the two former cases for the most accurate solution. With this in mind, stress distributions for these cases were also evaluated subject to the individual application of each of the load sources, i.e. bolt and pressure loading. Results are presented in Figures 7-4 through 7-6. It may be noted that in the case of bolt loading only, the simple frame model (hinged supports) provides the same support reactions as the flanged frame model. This follows from the expressions provided in Chapter 5. Coincidentally, the resultant stress distribution in the side plate and tube sheet is also equivalent for the two. As a result of this, the contribution of bolt loading is only presented in Figure 7-4. The rigid frame models can therefore be distinguished by the case of pressure load only. Throughout Figures 7-4 to 7-6, the unconstrained rigid frame models can be observed to provide poor correspondence with the FEM. Of the two remaining rigid frame models having constrained supports, the flanged frame model can subsequently be concluded to provide a visibly superior approximation of the finite element model.

In Table 7-1, bending stress results from Figures 7-4 through 7-6 are presented, where only the rigid frame models having constrained supports are considered. The locations used to extract the bending stresses correspond to the ends of the FEM plots for the side plate and tube sheet. In the case of the tube sheet, the result is the same at either end due to symmetry.

Table 7-1: Bending stress result comparison for the two rigid frame models having constrained supports, and FEM

Plate	***Side plate***		***Tube sheet***
Location on plate	**Junction to flange**	**Junction to tube sheet**	**Junction to side plate**
Bolt loading only			
Simple frame (hinged)	92.4 MPa	-6.4 MPa	-18.8 MPa
Flanged frame	92.4 MPa	-6.4 MPa	-18.8 MPa
FEM	**76.4 MPa**	**-5.8 MPa**	**-16.0 MPa**
Pressure loading only			
Simple frame (hinged)	13.9 MPa	-26.4 MPa	-27.8 MPa
Flanged frame	38.6 MPa	-28.2 MPa	-32.3 MPa
FEM	**40.6 MPa**	**-35.3 MPa**	**-40.6 MPa**

As previously noted, the results for the simple frame model and flanged frame model are identical in the case of bolt loading only. For pressure loading however, the flanged frame model provides closer correspondence. At the junction to the flange in the case of pressure loading, the flanged frame model for example predicts a value 2 MPa lower than the FEM, whereas the simple frame model predicts a value 16 MPa lower. The lack of correlation for bolt loading is further investigated in Section 7.2.

It may be concluded that the flanged frame model having constrained supports provides the best approximation of the FEM.

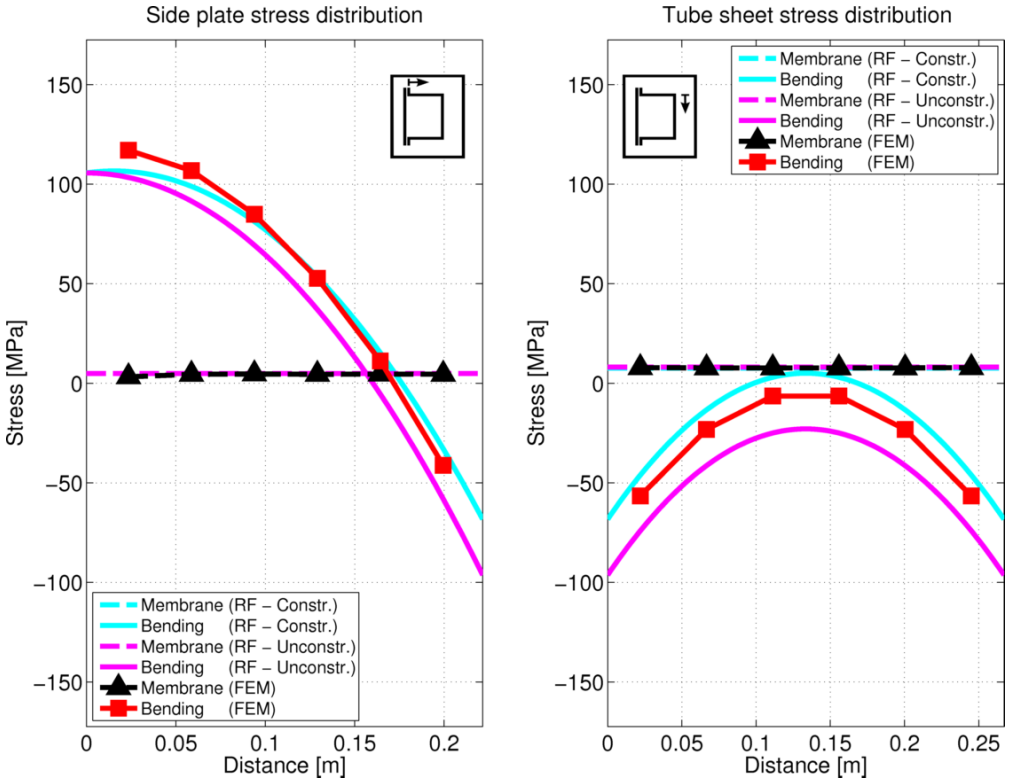

Figure 7-2: Stress distributions for the simple frame models having hinged supports compared to the FEM for operating load

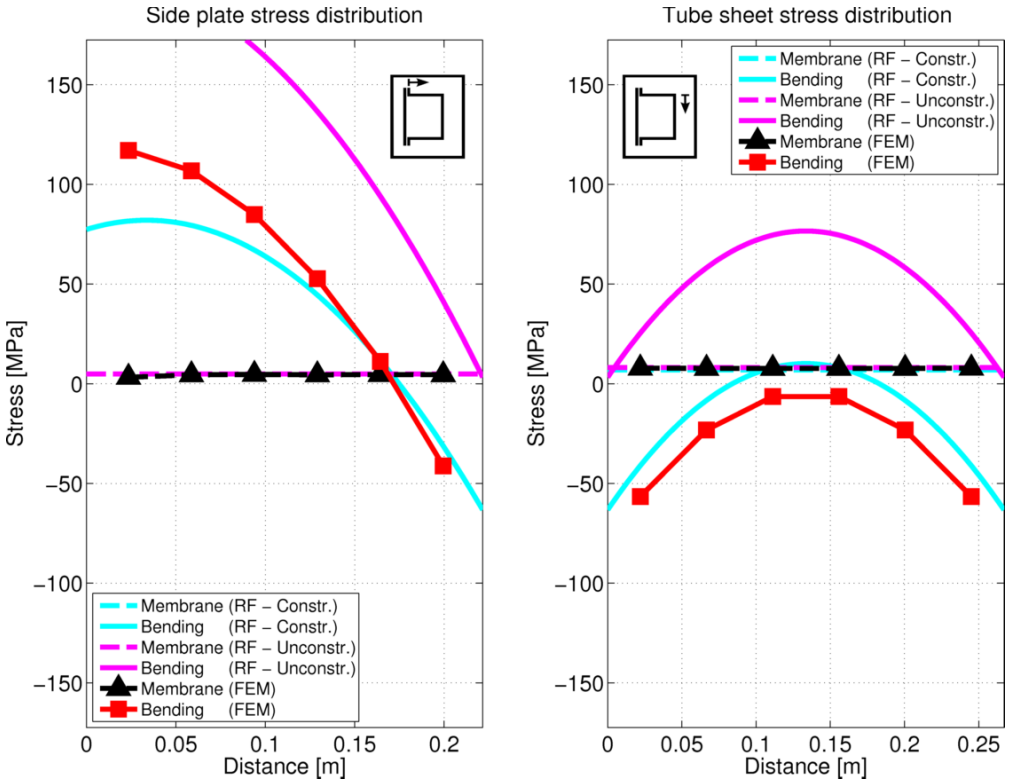

Figure 7-3: Stress distributions for the simple frame models having built-in supports compared to the FEM for operating load

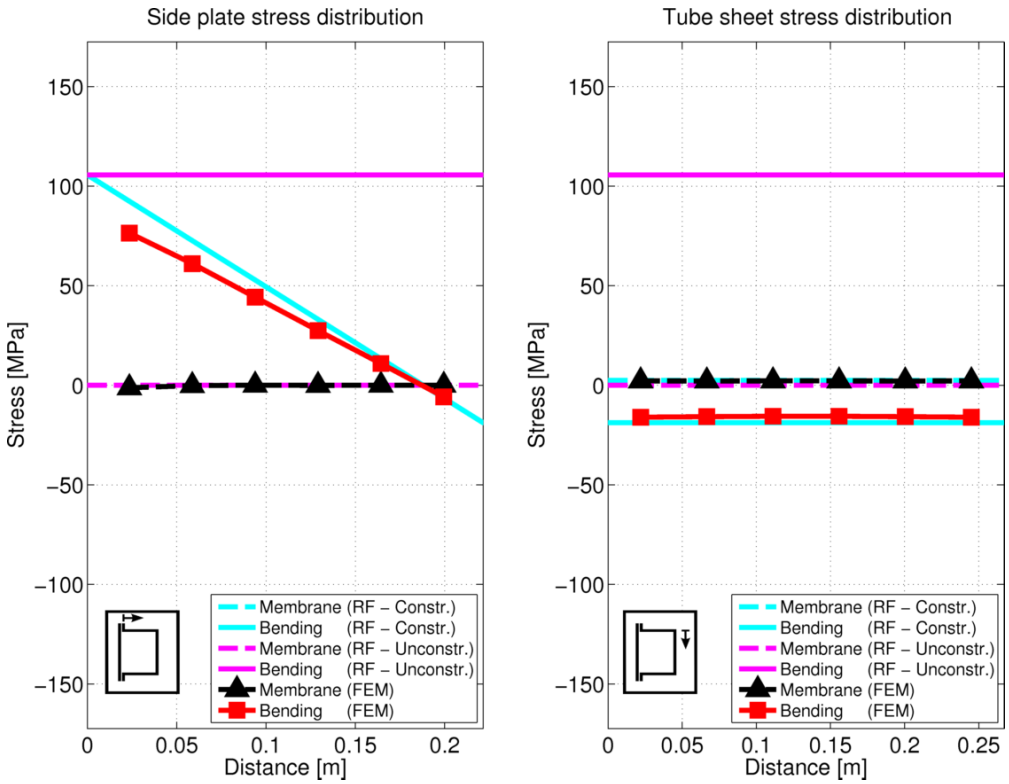

Figure 7-4: Stress distributions for the flanged frame models compared to the FEM for gasket seating load only. Note that the simple frame model gives identical results

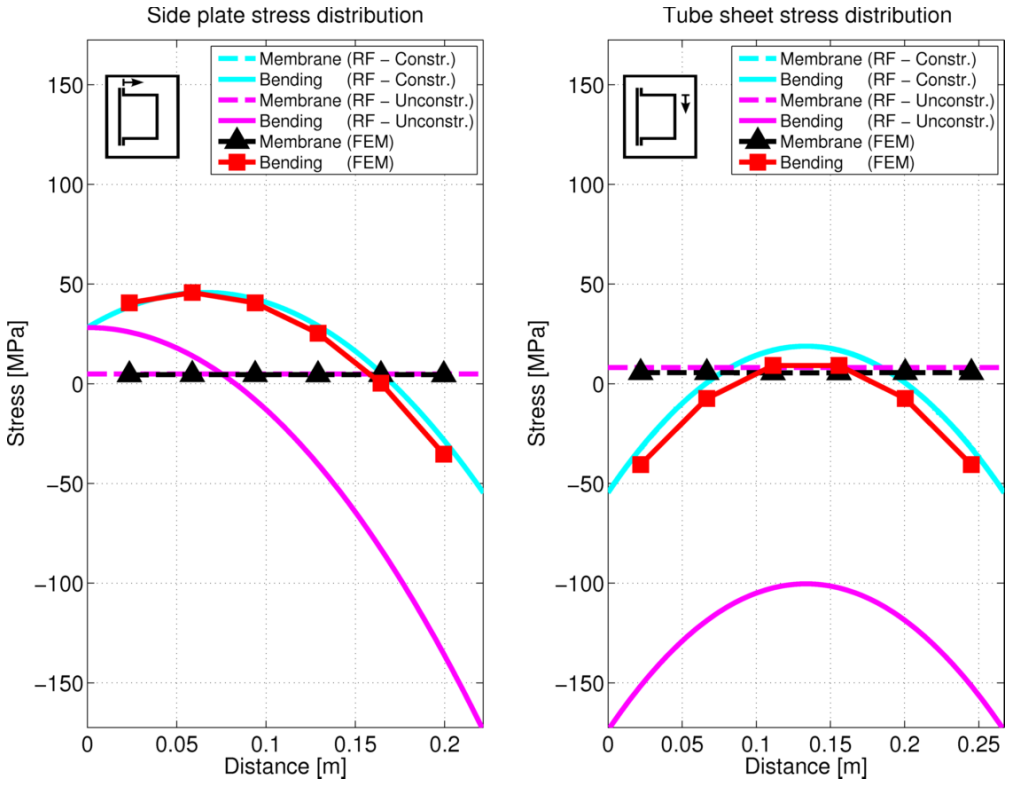

Figure 7-5: Stress distributions for the flanged frame models compared to the FEM for pressure load only

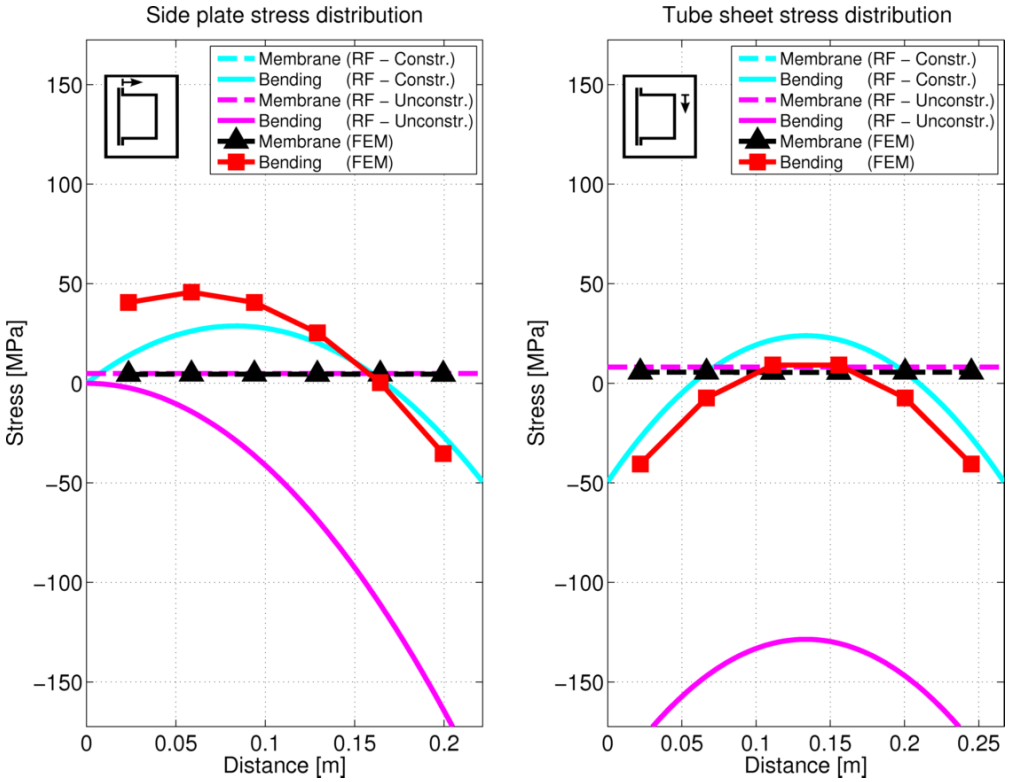

Figure 7-6: Stress distributions for the simple frame models having hinged supports compared to the FEM for pressure load only

7.2 Effect of including bolt bending moment in rigid frame model

It was previously mentioned that the coupled bolt model offers resistance to the rotation of the flange. As a result of this, a further bending moment is applied to the header box bonnet, in addition to the tensile load from bolt pre-tension. To include this into the flanged frame model, a bolt bending moment was extracted from the finite element model. This was done by extracting the bending moments of the two beam elements located at the centre of the header box length, with reference to the node coupled with the header box bonnet, and averaging them, similar to the bending stress at the front of the elements 9 and 10 as portrayed by Figure 6-17. This was done for the gasket seating condition only, with the result being as follows on a per unit length basis:

$$\left(M_{jw}\right)_{\text{flange rotation}} = -1\ 406.2\ Nm/m. \qquad \textbf{(7-1)}$$

This bending moment is roughly 16 % of the one calculated for pre-tension alone (M_{jw}). It is included into the flanged frame model through appropriate modification of the bolt loading scenario, with Figure 7-7 and 7-8 being subsequently obtained. These figures correspond to the cases of gasket seating and operating load, and compare favourably to Figures 7-4 and 7-1. The contribution of pressure loading alone remains unaffected.

To illustrate the level of improvement in correspondence upon including the bending moment of Equation (7-1), bending stresses are once again presented in Table 7-2 for gasket seating in the same manner as for Table 7-1. At the junction to the flange, the bending stress is now within 7.7 % of the FEM, instead of 21 % previously.

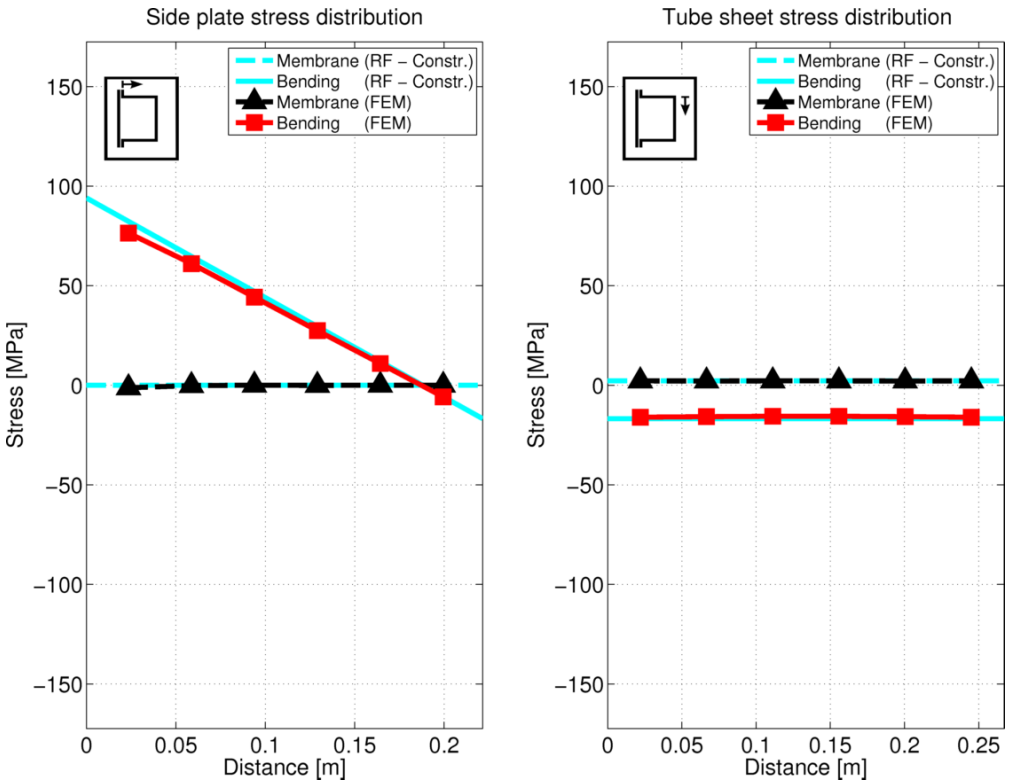

Figure 7-7: Improved gasket seating condition represented by the constrained rigid frame model including flange arms (note improvement compared to Figure 7-4)

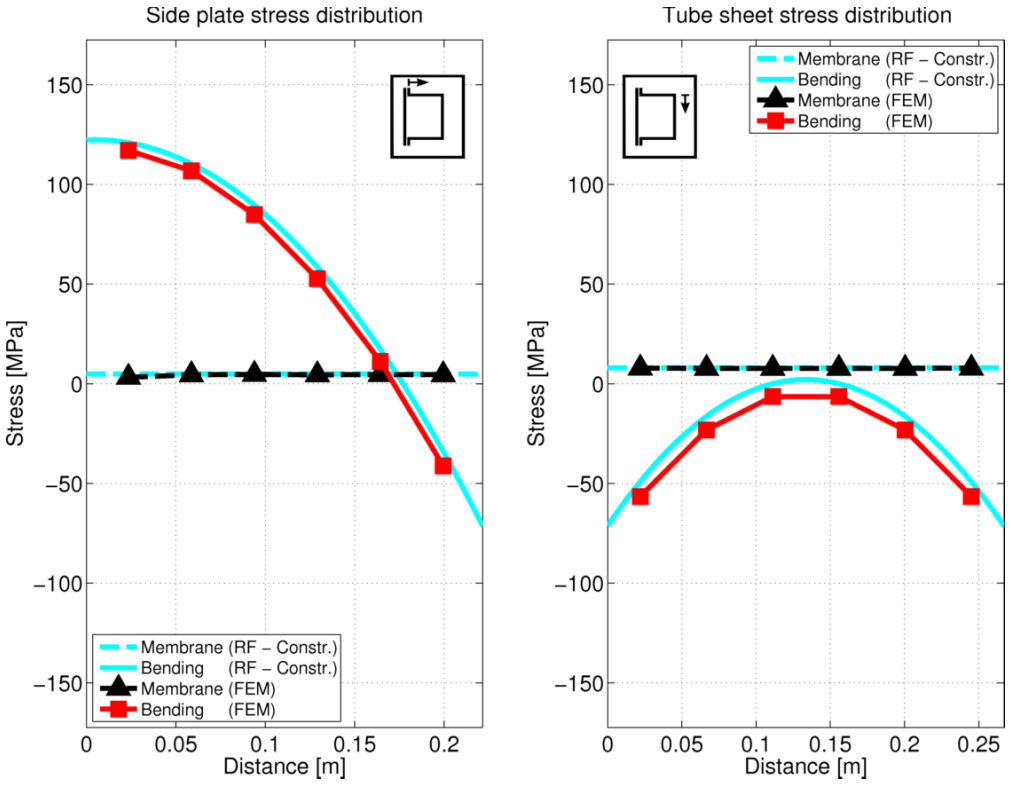

Figure 7-8: Improved overall stress distribution resulting from the constrained rigid frame model including flange arms

Table 7-2: Bending stress results comparison for the inclusion of an additional bending moment

Plate	***Side plate***		***Tube sheet***
Location on plate	**Junction to flange**	**Junction to tube sheet**	**Junction to side plate**
Bolt loading only			
Flanged frame (Original)	92.4 MPa	-6.4 MPa	-18.8 MPa
Flanged frame (Incl. additional moment)	82.3 MPa	-5.7 MPa	-16.7 MPa
FEM	**76.4 MPa**	**-5.8 MPa**	**-16.0 MPa**

7.3 Results comparison in the context of failure quantification

In this section, the results for the current design approach, flanged frame model (constrained supports) and finite element model are evaluated subject to failure criteria. Both design by rule and design by analysis are discussed.

7.3.1 Design by rule comparisons (analogous to current design approach)

Seven locations throughout the header box were selected for the purposes of comparison, including the six locations used for the current design approach, as well as an additional location in the side plate (see Figure 7-9). The six locations from the current design approach are:

1. junction formed by the flange and side plate (across the thickness of the flange);
2. centre of the cover-plate;
3. centre of the tube sheet;
4. junction formed by the tube sheet and side plate (across the thickness of the tube sheet);
5. junction formed by the tube sheet and side plate (across the thickness of the side plate);
6. and the centre of the side plate.

The additional location from the side plate is:

7. junction formed by the flange and side plate (across the thickness of the side plate).

Linearized stress results were extracted from the finite element model for each of the locations in a manner analogous to what was done in Section 6.2.3.3. For the case of the current design approach, calculations were however only performed for its original six locations, whilst for the rigid frame model only locations 1 and 3 through 7 (header box bonnet) were evaluated. Location 1 is available since the flanged frame model is being used. It should also be noted that the locations at the end of the tube sheet (4), side plate (5 and 7), and flange (1) were evaluated right at the point where the adjoining curves meet (i.e. the far left and right locations on the curves of Section 7.1). The bolt bending moment was furthermore modified for the aforementioned increase in loading. For the current design approach, the total bolt load was calculated by the conventional Equation (4-18), whereas for the rigid frame solution it was calculated by Equation (4-19) (i.e. as in Section 7.1).

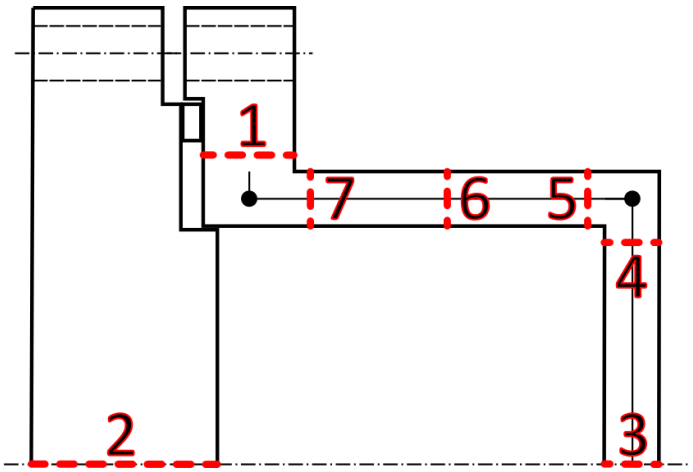

Figure 7-9: Layout of locations used for design by rule comparison

Figure 7-10 illustrates the absolute membrane and bending stress at the selected locations. The FEA results are plotted with 20 % bands denoted by blue rectangles, where the horizontal red lines represent the exact values.

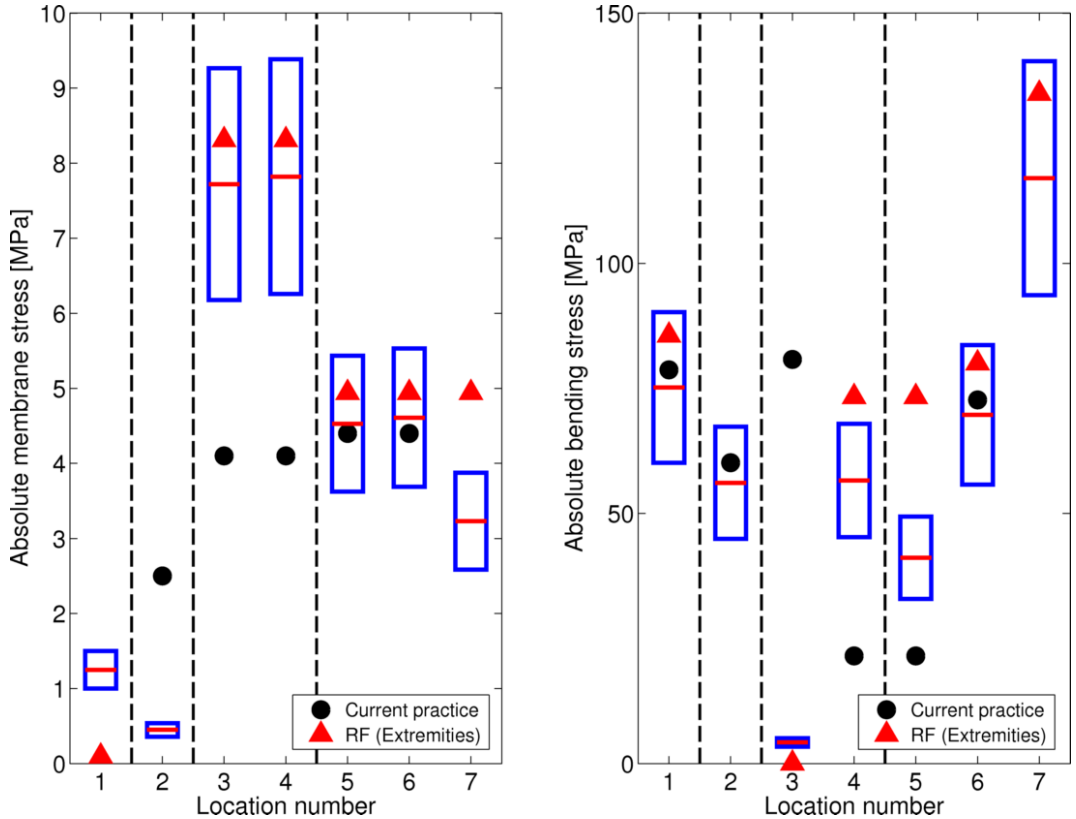

Figure 7-10: Comparison of design by rule results. The FEM results are plotted with 20 % bands. Dotted vertical lines are superimposed on the plot to denote the different regions, namely the flange (1), cover-plate (2), tube sheet (3 and 4), as well as the side plate (5 through 7). Notice the different scale of the vertical axes of the plots

Stress results are used to design the thickness of the flange, cover-plate, tube sheet, and side plate respectively. In Sections 7.3.1.1 through 7.3.1.4 each of these cases is evaluated. It is further important to note that designs are carried out based on allowable values set for membrane, bending

and combined stresses. The stresses applicable to each case are summarized in Tables 7-3 through 7-6.

7.3.1.1 Design of the flange

In Table 7-3 the results for location 1, which is used in the design of the flange, are presented. It is only at this location that current design practice computes a shear stress, bending stress and a subsequent Tresca value for the combined stress. On the other hand, in the cases of the FEM and rigid frame solution, the combined stress is computed as the aggregate of the membrane and bending components. Based on the FEM results, bending stress has the greatest contribution towards the combined stress, which dictates the flange thickness. In this respect, the rigid frame model provides a conservative solution of 86.2 MPa in comparison to the FEM's 76.4 MPa. The current design approach results in a slightly lower conservative solution at 82.7 MPa.

Table 7-3: Design by rule results comparison for the design of the flange

Location	***1***			
Stress	**Shear [MPa]**	**Membrane [MPa]**	**Bending [MPa]**	**Combined [MPa]**
Rigid frame model	5.2	0.1	85.6	86.2
FEM	**5.7**	**1.3**	**75.2**	**76.4**
Current approach	12.7	N/A	78.7	82.7
Allowable	*58.95*	*117.9*	*176.85*	*176.85*

7.3.1.2 Design of the cover-plate

The rigid frame model is only intended for the design of the header box bonnet. With respect to the cover-plate, the current design approach may be observed to provide a conservative solution in comparison with the FEM, where the bending stress is of greatest significance.

Table 7-4: Design by rule results comparison for the design of the cover-plate

Location	***2***			
Stress	**Shear [MPa]**	**Membrane [MPa]**	**Bending [MPa]**	**Combined [MPa]**
Rigid frame model	N/A	N/A	N/A	N/A
FEM	**N/A**	**0.5**	**56.1**	**56.6**
Current approach	N/A	2.5	60.1	62.2
Allowable	*58.95*	*117.9*	*176.85*	*176.85*

7.3.1.3 Design of the tube sheet

Locations 3 and 4 are used in the design of the tube sheet. The current design approach predicts the most critical location to be at its centre (3). At this location it predicts a bending stress of 80.8 MPa. This is conservative in comparison to the FEM, which calculates a value of 4.3 MPa at the same location. According to the FEM results, the most critical location is at the junction with the side plate (3), where it predicts a bending stress of 56.6 MPa only. The rigid frame model also identifies this location as the most severe with a bending stress of 73.3 MPa. It subsequently follows that if the rigid frame model were used, a critical combined stress of 81.6 MPa would dictate the thickness of the sheet, instead of the 84.9 MPa predicted by the current approach. The result would still have

been conservative in comparison with the FEM. This discrepancy is due to the inherent conservatism of the current design approach, which adopts a simply supported beam model of the tube sheet.

Table 7-5: Design by rule results comparison for the design of the tube sheet

Location	***3***			
Stress	**Shear [MPa]**	**Membrane [MPa]**	**Bending [MPa]**	**Combined [MPa]**
Rigid frame model	N/A	8.3	0.1	8.4
FEM	**N/A**	**7.7**	**4.3**	**12.0**
Current approach	N/A	4.1	80.8	84.9
Location	***4***			
Stress	**Shear [MPa]**	**Membrane [MPa]**	**Bending [MPa]**	**Combined [MPa]**
Rigid frame model	N/A	8.3	73.3	81.6
FEM	**N/A**	**7.8**	**56.6**	**64.4**
Current approach	N/A	4.1	21.5	25.6
Allowable	*58.95*	*117.9*	*176.85*	*176.85*

7.3.1.4 Design of the side plate

Table 7-6: Design by rule results comparison for the design of the side plate

Location	***5***			
Stress	**Shear [MPa]**	**Membrane [MPa]**	**Bending [MPa]**	**Combined [MPa]**
Rigid frame model	N/A	4.9	73.3	78.2
FEM	**N/A**	**4.5**	**41.2**	**45.7**
Current approach	N/A	4.4	21.5	26.0
Location	***6***			
Stress	**Shear [MPa]**	**Membrane [MPa]**	**Bending [MPa]**	**Combined [MPa]**
Rigid frame model	N/A	4.9	80.0	85.0
FEM	**N/A**	**4.6**	**69.7**	**74.3**
Current approach	N/A	4.4	72.7	77.1
Location	***7***			
Stress	**Shear [MPa]**	**Membrane [MPa]**	**Bending [MPa]**	**Combined [MPa]**
Rigid frame model	N/A	4.9	133.9	138.9
FEM	**N/A**	**3.2**	**117.0**	**120.2**
Current approach	N/A	N/A	N/A	N/A
Allowable	*58.95*	*117.9*	*176.85*	*176.85*

A total of three locations are presented for the design of the side plate, where the junction with the flange (7) is not evaluated by current design practice. It is at this location that the FEM and rigid frame model predicts the most critical stress to exist. They respectively predict a bending stress of 117 MPa and 133.9 MPa. The rigid frame model is therefore conservative in comparison. From the two remaining locations evaluated by the current approach, the centre of the side plate (6) results in the largest stress. At this location, a bending stress of 72.7 MPa is found. It subsequently follows that a combined stress of 77.1 MPa would be calculated at this point, governing the thickness of the plate. This is not conservative in comparison to the result for the FEM at the junction, in which case a

value of 120.2 MPa can be found. In contrast, the rigid frame model does produce a conservative solution of 138.9 MPa.

7.3.1.5 Concluding remarks

Based on the results, the header box design problem is primarily influenced by bending stress, where the results for the rigid frame model showed the best correspondence with the FEM. These results were furthermore conservative in comparison.

For the design of the tube sheet, the current design approach could be observed to provide a conservative solution based on stress results at a different critical location to the FEM. This discrepancy is an inherent result of the simply supported beam modelling approach for the sheet. Similarly, the FEM results indicated a different result to the current approach for the side plate. The junction with the flange (7) was identified to be most critical (FEM), a location which is not evaluated by the current design approach. It was furthermore observed that the combined stress computed by the current approach for the side plate was not conservative in comparison to the FEM. It should however be noted that in almost all cases a nozzle attachment is included onto a side plate. In such a case, the combined stress at the centre of the plate is generally multiplied by a factor of two (current approach). If this factor were to be included, the current design approach would have provided a combined stress of 154.2 MPa. In Chapter 8, this result is compared against design by analysis results for the inclusion of a nozzle attachment. In addition, if this factor were to be incorporated into the rigid frame model, it may be noted that, as in the current approach, it also provides a conservative solution in comparison with the FEM at the centre of the side plate (85.0 MPa for the rigid frame, in comparison with 77.1 MPa for the current approach).

7.3.2 Design by analysis comparisons

Design by analysis was first introduced on page 9 for linear elastic FEA, where the method of linearization, stress classification, and failure criteria were discussed. Appropriate linearization has particular importance, because it may produce non-conservative results for heavy-wall structures (e.g. cylinders having diameter-to-thickness ratios of below eight [5]) due to misinterpretation of nonlinear characteristics. Stress categorization can also be challenging for complex geometries, and may necessitate significant knowledge and judgement. Moreover, the allowable limits for both local failure and plastic collapse failure were presented. For the purposes of this section, only the plastic collapse failure criterion will be implemented. As in the case of the current design approach, it also requires the computation of a membrane, bending and combined value. Local failure on the other hand entails the calculation of the sum of principal stresses.

Design by analysis gives you the freedom to evaluate any conformant SCL within a three-dimensional stress field. With this in mind, the same seven failure locations as in the design by rule comparisons (see Section 7.3.1) are evaluated in Section 7.3.2.1, whilst in Section 7.3.2.2 a number of additional locations are studied. Only the operating condition is implied for these evaluations, so as to be consistent with the current design calculations. The influence of bolt loading and pressure loading will therefore be dealt with simultaneously.

7.3.2.1 Current design failure locations

A number of examples of appropriate stress categorization are provided in the ASME code [5], which may be used for reference. From these examples, the case of a flat head connection (i.e. a circular plate attached to a cylinder) can be identified as most relevant to the current design failure locations (see Figure 7-9). Details for this example are provided in Table 7-7.

Table 7-7: Stress categorization in a flat head [5]

Vessel component	Location	Origin of stress	Type of stress	Classification
Flat head	Centre region	Internal pressure	Membrane	P_m
			Bending	P_b
	Junction to shell	Internal pressure	Membrane	P_L
			Bending	Q [see note]
Note: If the bending moment at the edge is required to maintain the bending stress in the centre region within acceptable limits, the edge bending is classified as P_b (otherwise, it is classified as Q).				

From the design locations portrayed in Figure 7-9, locations 2, 3 and 6 correspond best with the centre region of a flat plate. For the header box problem, membrane and bending stress results at these locations are categorized as primary. The remaining locations are analogized to the junction formed by a flat plate and shell. For a flat head connection, the membrane stress at the junction is classified as local whilst bending stress is classified as Q (i.e. has bearing on fatigue analysis). However, if the bending stress at the junction is pivotal to maintaining an acceptable bending stress at the centre region it should be evaluated as primary. As a result of the dominance associated with bending stress in the header box problem, shown in Section 7.1, this exception is especially relevant. Bending stress results for the header box problem at junction locations 1, 4, 5 and 7 are categorized as primary.

In summary, each of the failure locations is considered to represent a primary bending stress. In addition, the centre locations (2, 3 and 6) have primary membrane stresses, whereas the junction locations (1, 4, 5 and 7) have local membrane stresses. The plastic collapse failure criteria [5] are once again included in Equations (7-2) through (7-4). From these equations, it can also be inferred that maximum conservatism is implied when selecting the bending stresses (locations 2, 3 and 6) as being primary. If they were omitted, restrictions would only be placed on the membrane stresses.

$$P_m \leq S \tag{7-2}$$

$$P_L \leq 1.5S \tag{7-3}$$

$$\left(P_L + P_b\right) \leq 1.5S \tag{7-4}$$

For the calculation of a membrane plus bending equivalent stress, as required by Equation (7-4), it was decided to add the linearized membrane and bending stress tensors, prior to the computation of a Von Mises equivalent. Table 7-8 illustrates the results for all of the locations. Best judgment was implemented in accordance with the guidelines for linearization. It follows from the results, that all of the design allowable limits are met, where the membrane stress seems to be of little significance. The most critical location is at 7 with regard to the membrane plus bending equivalent stress.

Table 7-8: Design by analysis results for the respective failure locations [MPa]

Point of failure	1	2	3	4	5	6	7
Membrane	10.36	1.25	7.15	7.90	12.78	8.37	5.14
Allowable	176.85	117.9	117.9	176.85	176.85	117.9	176.85
Membrane + Bending	68.68	50.00	10.82	52.09	39.18	66.01	107.46
Allowable	176.85	176.85	176.85	176.85	176.85	176.85	176.85

In order to further compare the level of conservatism for the respective approaches of current design practice, flanged rigid frame model and design by analysis, the combined stress at each location was also evaluated as a fraction of the allowable (see Figure 7-11). In general, design by analysis provides a less conservative solution than the design by rule cases. This may be ascribed to the contribution of the full three-dimensional stress state to an equivalent result, whereby the supporting effect of the end plates is for example also included. However, in the case of the side plate the current design approach once again does not provide a conservative solution in comparison with design by analysis, which also predicts location 7 to be critical.

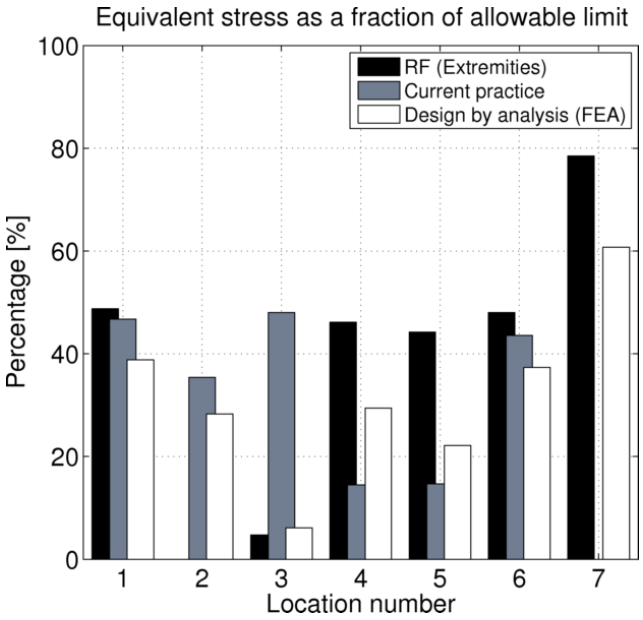

Figure 7-11: Comparison of results for current design practice, flanged rigid frame model, and design by analysis

7.3.2.2 Additional failure locations

To properly evaluate the full breadth of the header box FEM, it is important to consider a variety of possible failure locations, especially those exhibiting higher levels of equivalent stress. From a Von Mises stress distribution plot of the header box, see Figure 7-12, we observe that the peak equivalent stress occurs at the junction formed by the end plate, side plate and flange. A number of SCLs were therefore investigated in this vicinity. The results for two SCL configurations at this junction are illustrated in Table 7-9. One is of an SCL projected across the thickness of the flange plate, whereas the other is projected across the thickness of the end plate. Since these SCLs are located at the junction formed by the end plate and flange, membrane stress results are considered to be local, whereas bending stress results are considered to be primary. Interestingly, the stress resulting across the flange plate in this case is of greater severity than that of location 1 in the current design locations. The membrane stress is roughly 22 MPa higher, and the combined

equivalent stress is about 49 MPa higher. The combined stress is 10 % larger than the peak value at location 7 in Table 7-8. As a result of this, current design practice's evaluation of location 1 no longer provides a conservative solution for the flange thickness in comparison (82.7 MPa vs. 117.99 MPa). From the perspective of design by analysis, the results presented in Table 7-9 are however acceptable, since the membrane and combined equivalent stresses are below their respective allowable limits.

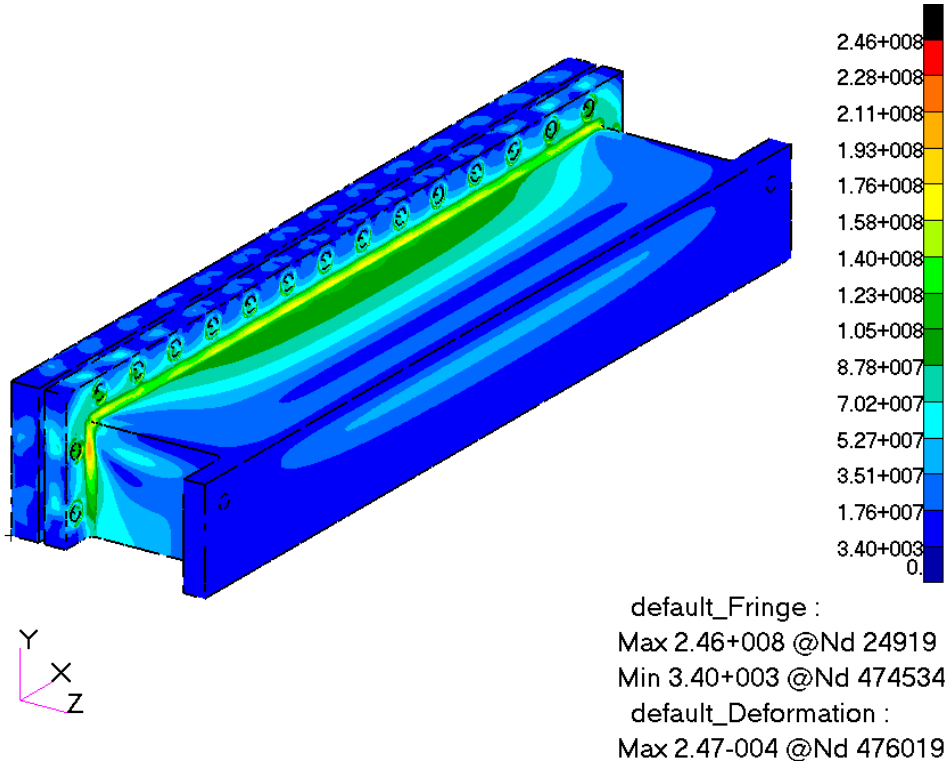

Figure 7-12: Equivalent Von Mises stress plot superimposed on true scale deformation of 3D header box subject to bolt pre-tension and 1 MPa pressure loading

Table 7-9: Additional locations selected for design by analysis evaluation and associated stresses

Location of SCL	Membrane [MPa]	Membrane + Bending [MPa]
A. End plate	28.22	93.90
B. Flange plate	33.28	117.99

It was further attempted to evaluate SCLs projected from the rounded fillet surfaces through the thickness at numerous locations, similar to Figure 6-8. As in the 2D example case of Section 6.1.2, these were however generally observed to contradict the linearization guidelines.

7.4 Concluding remarks

In this chapter, results for the current design approach, a number of rigid frame models and a finite element model were compared.

Through evaluation of the header box bonnet's stress distribution, the flanged frame model having constrained supports could be shown to provide the best correspondence of all of the rigid frame

models with the FEM results. These stress distributions could furthermore be noted to be dominated by bending stress, where a significant contribution results from the gasket seating condition. This is due to the semi-confined gasket arrangement of the flanged construction, whereby the bolts are placed at an offset to the gasket. It can therefore be concluded that the stress could be reduced by means of an improved flanged construction, for example, if the gasket were centred over the bolt holes (i.e. non-confined). However, although this construction would be beneficial from a structural design perspective, it is not ideal from an operational perspective. This design is generally associated with a higher likelihood of leakage [4].

Further design by rule comparisons showed the current design approach to provide conservative solutions for the design of the flange, tube sheet and cover-plate thicknesses in comparison with the FEM. It must however be noted that in the case of the side plate, this would only be the case if the nozzle efficiency factor were included. The critical stress predicted by the current approach here is 77.1 MPa, in comparison with 120.2 MPa for the FEM. The flanged rigid frame model on the other hand did provide conservative results for the flange plate, side plate and tube sheet in comparison with the FEM. In general, these results were also less conservative than the current design approach and provided better correspondence with the FEM.

Design by analysis was finally also implemented on the header box FEM. At the locations used for the design by rule comparisons, design by analysis provided less conservative solutions than the current design approach in most instances. Once again, only the results for the side plate were not conservative. The rigid frame model on the other hand did provide a conservative solution for its intended use on the tube sheet, side plate and flange. In addition, it presented an opportunity for less conservative design in the case of the tube sheet.

Two additional locations were evaluated by design by analysis at the junction formed by the side plate, end plate and flange. The results in this vicinity are more dependent on the thickness of the end plate. In this case, the end plate (17 mm) is thinner than the side plate and tube sheet (27 mm). The location is also difficult to evaluate using SCLs, and it would be more appropriate to use nonlinear FEA. Although the results for the two SCLs were observed to be well below the allowable limits, it is recommended that the design of the end plate thickness, and the evaluation of complex locations such as this junction, be studied further in future. One possible workaround could be to design the end plate to the same thickness as the side plate.

In Chapter 8 to follow, the influence of a nozzle attachment will be investigated more closely by means of design by analysis. This design approach is necessary due to the inherently complex three-dimensional stress response.

8 Analysis of the nozzle attachment

In this chapter, two aspects of the four inch nozzle attachment of the example header box are investigated, namely nozzle placement and external loading. The placement of the nozzle is looked at by evaluating two configurations, whereby the nozzle is respectively positioned at the centre (see Figure 8-1) and end (see Figure 8-2) of the side plate. Since the size of the nozzle generally dictates the width of the side plate, it can realistically only be moved along its length. External nozzle loading requirements are presented in API 661 [1], where the orientation of prescribed loads and their effect on the stress response is looked at more closely. Design by analysis was adopted throughout this investigation for its superior capability in dealing with three-dimensional behaviour via FEM.

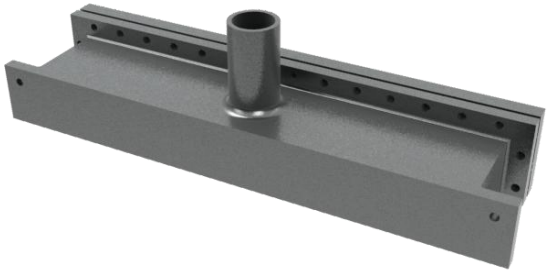

Figure 8-1: Illustration of nozzle attachment at the centre of the side plate

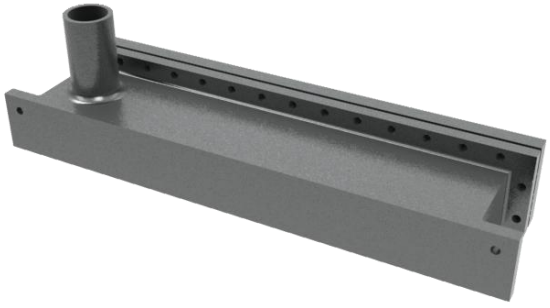

Figure 8-2: Illustration of nozzle attachment at the end of the side plate

This chapter starts off by discussing the modifications made to the existing finite element model, and the details surrounding its analysis. Subsequently, stress results for a number of loading conditions are presented, including the seating condition, operating condition (i.e. bolt pre-tension and pressure) and the operating condition with nozzle loading superimposed. Additional attention is given to the influence of nozzle load orientation. Finally, a few concluding remarks are made.

8.1 Modelling and analysis specifics

In this section, details surrounding the geometric representation of the header box including a nozzle attachment, the application of nozzle loading, and extraction of results from the finite element model are elaborated upon. As for the original finite element model, both a coarse and fine 10-noded tetrahedral element mesh was generated. In this case, care was taken to achieve an appropriate number of elements through the thickness of the nozzle wall.

8.1.1 Geometrical representation

To represent the header box including a nozzle attachment, the original finite element model of Chapter 6 was only slightly modified. In this half symmetry model, the nozzle was included as a cylinder penetrating the side plate, where a corrosion allowance of 3 mm was once again removed on the internal surface. With the application of half symmetry, it is implied that equivalent nozzle

attachments subject to mirrored external loading exist on either of the header box side plates. Since the goal of the current investigation is only to gain insight into the effect of the nozzle attachment, the approach provides sufficient detail. In addition, the communication of the nozzle load from one side of the header box to the other will be shown to be small in Section 8.2.

A further important aspect is the representation of the welded junction at the base of the nozzle. A number of acceptable nozzle attachment welds are represented in the ASME code [5] specifically under Part UHT of Division 1. This section considers pressure vessel components which have been heat treated. From inspection of an existing header box design, the construction of a typical nozzle attachment weld may be portrayed as in Figure 8-3, an example of which may be observed in Figure 6-11. As was discussed in Section 6.1.2, a number of complications however arise when modelling a weld bead as square. In an effort to avoid this, an alternative construction was selected from the code (see Figure 8-4). In this case, a smooth transition is made from the flat side plate to the nozzle. It is also easier to radiograph for defects, although it may be more expensive to manufacture.

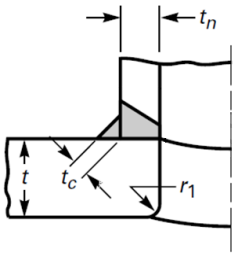

Figure 8-3: Example nozzle attachment

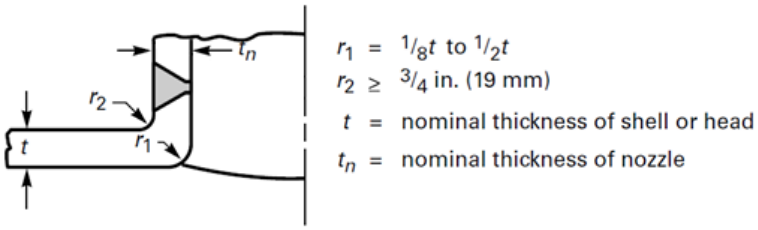

Figure 8-4: Alternative nozzle attachment

With reference to Figure 8-4, the larger fillet radius (r_2) was selected as 19 mm, the minimum allowable. Subsequently setting the smaller fillet radius (r_1) to the minimum available value, a scale representation of the junction may be observed in Figure 8-5. Because of the relative size of this fillet, it was decided to discard it (i.e. model a sharp corner) so as to lessen the computational requirement.

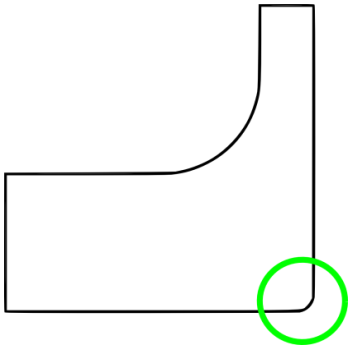

Figure 8-5: Depiction of the small material influence associated with the internal fillet at the base of the nozzle

The positioning of the nozzle along the width of the side plate was chosen to adhere to ergonomic requirements regarding the bolted joints. It should further be noted that quarter symmetry is lost once the nozzle is positioned at an off-centre location along the header box length. It therefore becomes necessary to evaluate each of the stud elements independently.

8.1.2 External load implementation

Nozzle loading in the finite element model results from the operating pressure and requirements outlined in API 661 [1] (see Section 2.2). The operating pressure generates a normal force at the end of the nozzle based on its internal cross section, whilst a collection of external forces and moments are prescribed in API 661 [1]. To implement these forces and moments in the FEM, a collection of MPCs were generated at the tip of the nozzle, similar to the case of the bolted joints. A central node is coupled in all degrees of freedom to the nodes on the face of the nozzle, effectively creating a rigid body, where the necessary loads are applied to the central node.

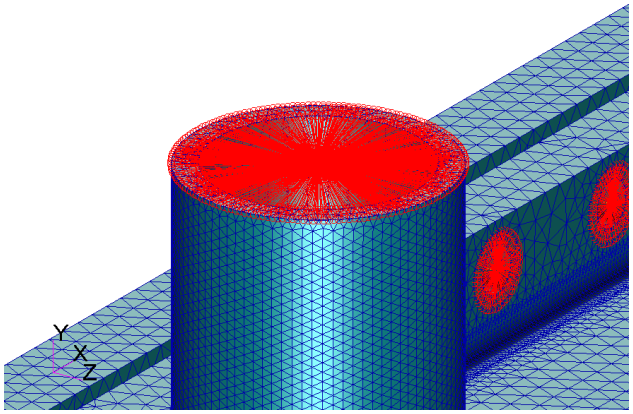

Figure 8-6: Illustration of the MPC created at the end of the nozzle for load implementation

8.1.3 Results extraction and classification

The region of interest upon superimposing a nozzle and its accompanying load requirements can be expected to correspond with the nozzle base. It is therefore necessary to obtain a comprehensive view of the results here. To do so, two planes were selected for evaluating stresses as highlighted in Figure 8-7 (see red surfaces). These planes allow for linearization across the thickness of the nozzle wall and side plate respectively. Curves A and B on the fringe of the model can furthermore be used as a reference for identifying the starting point of an SCL associated with each of these planes.

Upon processing the results of an analysis, linearization is performed on a number of uniformly spaced SCLs around the circumference of the nozzle. The local coordinate system in Figure 8-7 is referred to in this respect, where the blue arc denotes the origin and orientation of the angle (θ) associated with individual SCLs. Identifying a number of results around the circumference in this manner simplifies the identification of critical locations, and allows conclusions to be drawn on aspects such as loading orientation.

As in Chapter 7, only failure by plastic collapse was evaluated with design by analysis, where the guidelines for linearization were followed throughout. The ASME code [5] also provides a few examples for stress classification at the root of a nozzle. The one that is most appropriate for the header box problem is summarized in Table 8-1. A membrane stress is classified as local, whilst a bending stress is classified as primary. Stress attributable to restrained free end displacements of attached piping are to be excluded from this approach. The origins of nozzle loading are however

broader than this, and can for example be associated to the dead weight of piping and attachments, as well as the flow of process fluid. It is therefore sensible to view the external loads presented in API 661 [1] in the same light.

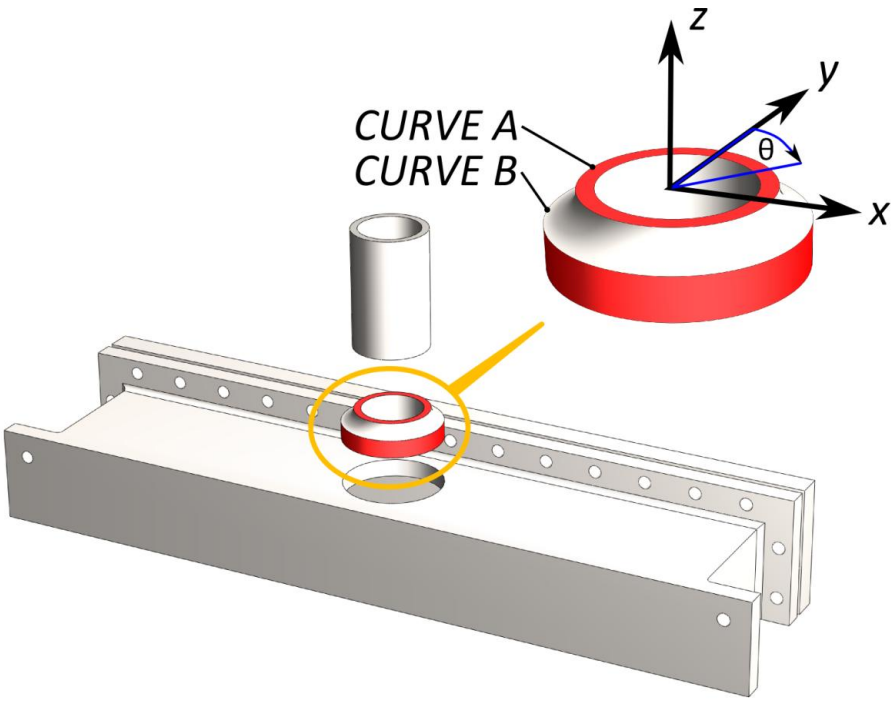

Figure 8-7: Illustration of the planes selected for nozzle stress evaluation

Table 8-1: Nozzle stress classification, adapted from [5]

Vessel component	Location	Origin of stress	Type of stress	Classification
Nozzle		Pressure and external loads and moments, excluding those attributable to restrained free end displacements of attached piping.	Membrane	P_L
			Bending	P_b

8.2 Stress evaluation under basic loading

In this section a preliminary investigation of the stress at the root of the nozzle is performed subject to three loading scenarios, as outlined below. The results furthermore correspond to the more refined finite element model.

A. Bolt pre-tension,
B. Bolt pre-tension with superimposed pressure loading,
C. Bolt pre-tension with superimposed pressure loading and assumed API nozzle loading.

For the assumed API nozzle loading, the coordinate system presented in Figure 2-5 is used in conjunction with the corresponding prescribed forces and moments.

In Sections 8.2.1 and 8.2.2, results for each of the nozzle placements are discussed. Figures 8-8 through 8-13 illustrate the linearized stress results around the circumference of the nozzle at its base. For each of these graphs, the horizontal axis corresponds to the angle of rotation θ described in Figure 8-7, where twelve uniformly spaced SCLs were evaluated (increments of 30°). The limits of the vertical axes correspond to the allowable limits from the ASME code [5].

As further motivation for investigation of the stress results at the root of the nozzle, refer to Appendix C. In Figures C-1 through C-4 the equivalent stress distribution throughout the header box may be observed for the sole application of the assumed API nozzle loading. The stress diminishes quickly upon moving away from the nozzle root, dropping below 10 % of the maximum local value at the root within a distance of one nozzle diameter along the header box length. This also supports the implementation of half symmetry, seeing as little of the nozzle load is communicated to either side of the header box.

8.2.1 Nozzle placed at the centre of the side plate

Figures 8-8 and 8-9 respectively represent the membrane and membrane plus bending (combined) equivalent stress results for positioning the nozzle at the centre of the header box length. Each of the graphs in the figures corresponds to the SCL planes shown in Figure 8-7. For loading scenarios A and B, the combined equivalent stress for an SCL originating on curve B (Figure 8-7), and stretching across the thickness of the side plate is most critical. Upon superposition of the API nozzle loading (case C) however, an SCL originating on curve A and stretching across the thickness of the nozzle wall becomes most critical.

The maximum combined equivalent stress results for the loading cases are presented in Table 8-2 for the uniformly spaced SCLs of Figures 8-8 and 8-9. In the instance of curve A, the API nozzle loading is responsible for an increase of 32.2 % over loading scenario B. In the case of curve B, this increase is 12.8 %. Overall, a rise of 20.38 % occurs as criticality switches from curve B to A.

Table 8-2: Most critical equivalent membrane plus bending stress results at nozzle root [MPa]

Location	0°	30°
Loading scenario	**Curve A**	**Curve B**
[A]	49.82	62.85
[B]	98.33	107.60
[C]	(+32.2 %) 130.00	(+12.8 %) 121.40

8.2.2 Nozzle placed at the end of the side plate

Figures 8-10 and 8-11 illustrate the results for placing the nozzle at the extreme left, as viewed in Figure 8-2. Comparing this to the results for the centrally placed nozzle, it provides a supportive effect leading to a reduction in stress. At this location, the effect of gasket seating and pressure is especially reduced. To illustrate the extent of the change, the peak combined equivalent stress results for the respective nozzle placements are summarized in Table 8-3. In this case, the combined equivalent stress of an SCL originating at curve B, and stretching across the side plate thickness consistently stays most critical.

Table 8-3: Comparison of peak equivalent membrane plus bending stress results [MPa] for different nozzle placements

Loading scenario	Curve A (centre)	Curve A (far end)	Curve B (centre)	Curve B (far end)
[A]	49.82	(-55.8 %) 22.00	62.85	(-27.7 %) 45.44
[B]	98.33	(-50.9 %) 48.28	107.60	(-33.0 %) 72.07
[C]	130.00	(-45.5 %) 70.81	121.40	(-31.8 %) 82.75

As a result of the reduced influences of bolt pre-tension and pressure, the relative effect of the API nozzle loading does however become more prominent. For example, the peak value on curve A increases by 46.7 % from loading scenario B to C, whilst for curve B it increases by 14.8 %. Compare this to 32.2 % and 12.8 % respectively, for the centrally placed nozzle.

As a matter of completeness, the assumed nozzle loading was also mirrored so as to illustrate what the effect would have been if the nozzle were placed at the far right of the header box. This follows from the symmetry associated with placing the nozzle at either end. Results are presented in Figure 8-12 and 8-13, where an insignificant change in peak values may be observed.

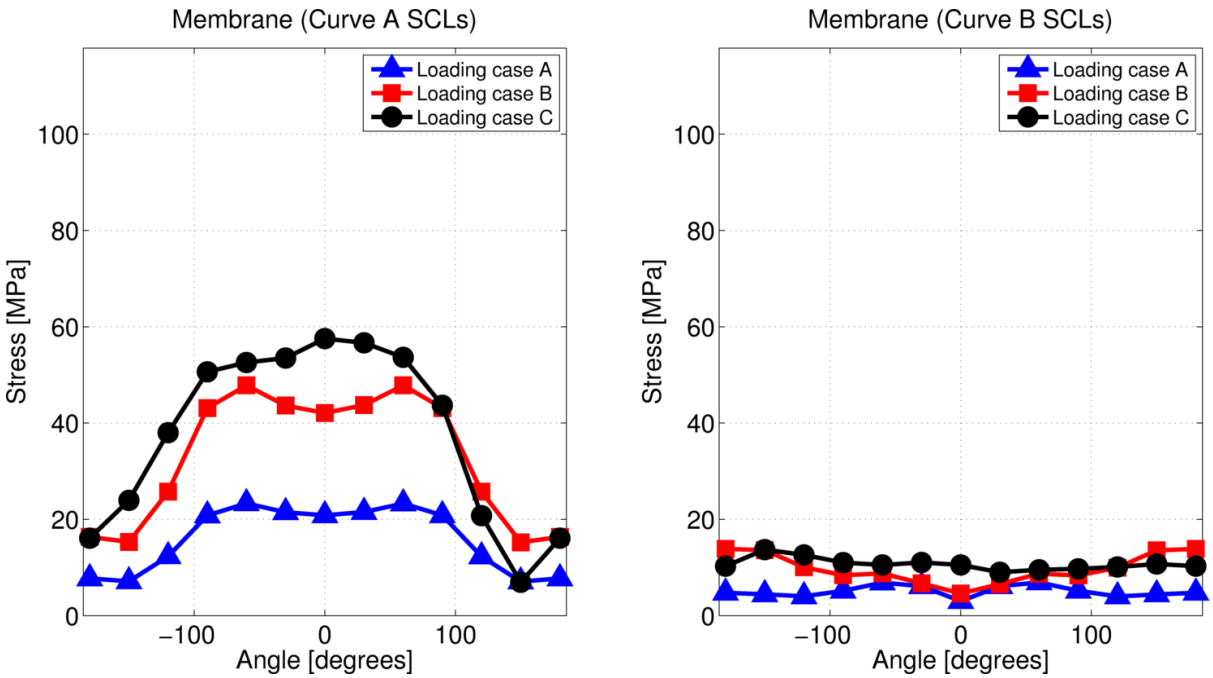

Figure 8-8: Membrane equivalent linearized stress around the circumference of the nozzle base, nozzle positioned at the centre of the side plate length

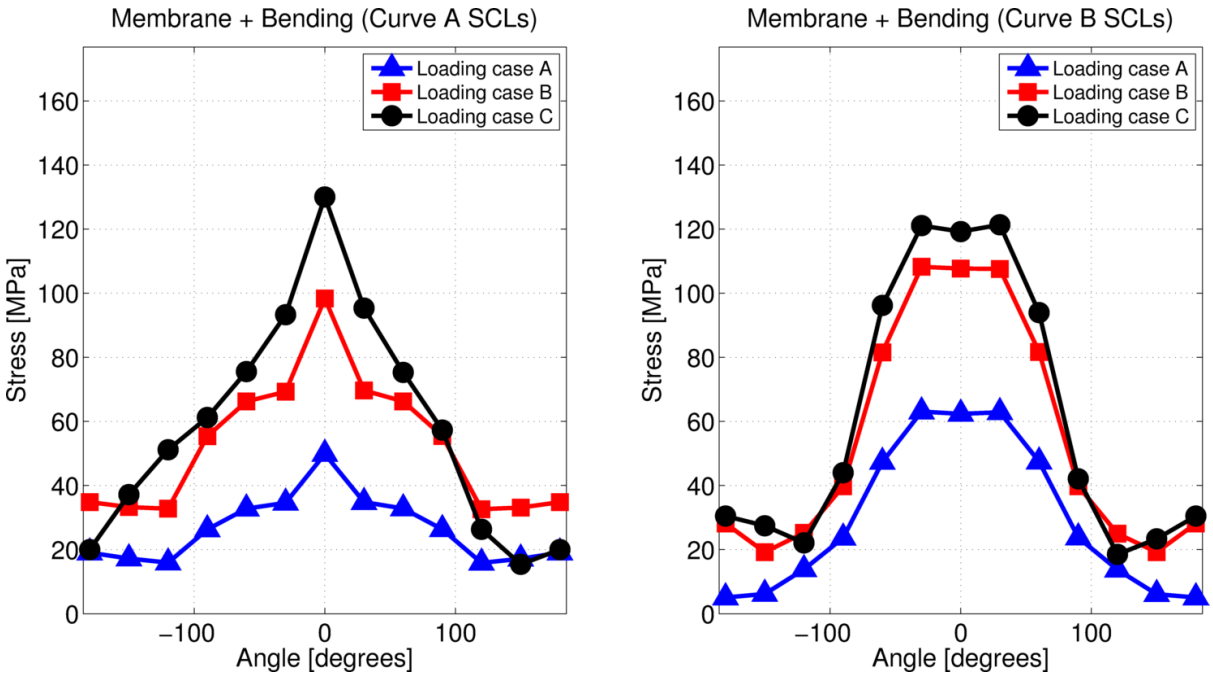

Figure 8-9: Membrane plus bending equivalent linearized stress around the circumference of the nozzle base, nozzle positioned at the centre of the side plate length

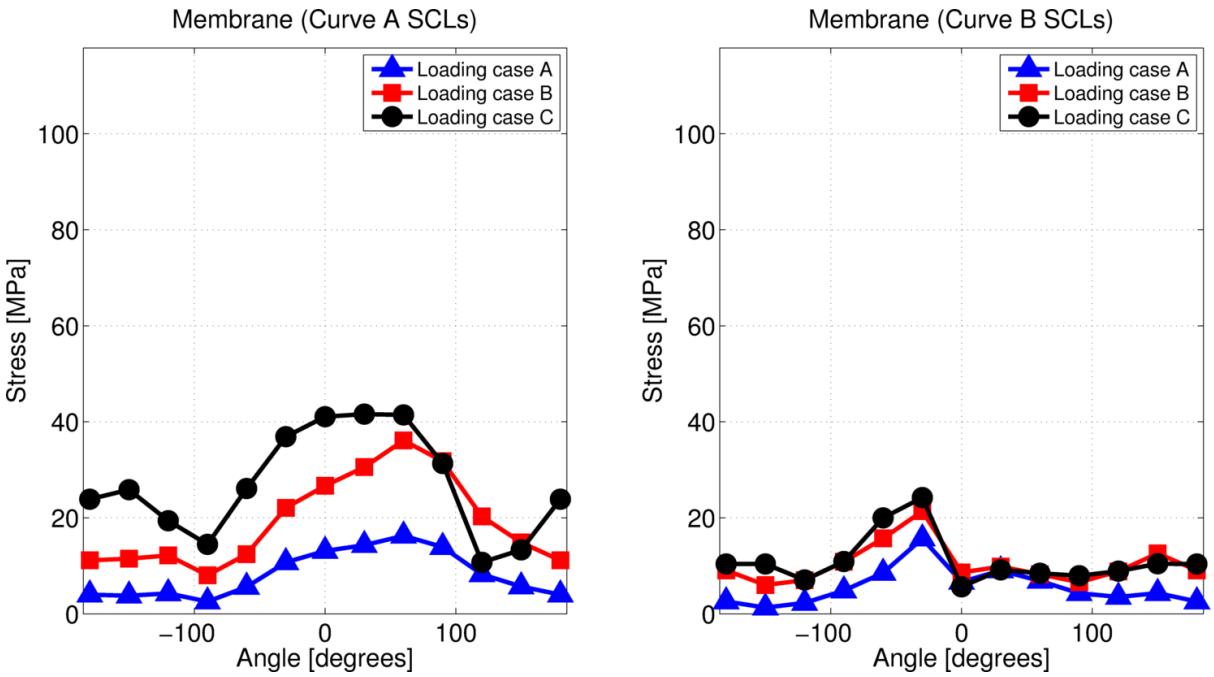

Figure 8-10: Membrane equivalent linearized stress around circumference of nozzle base, nozzle positioned at the end of the header box

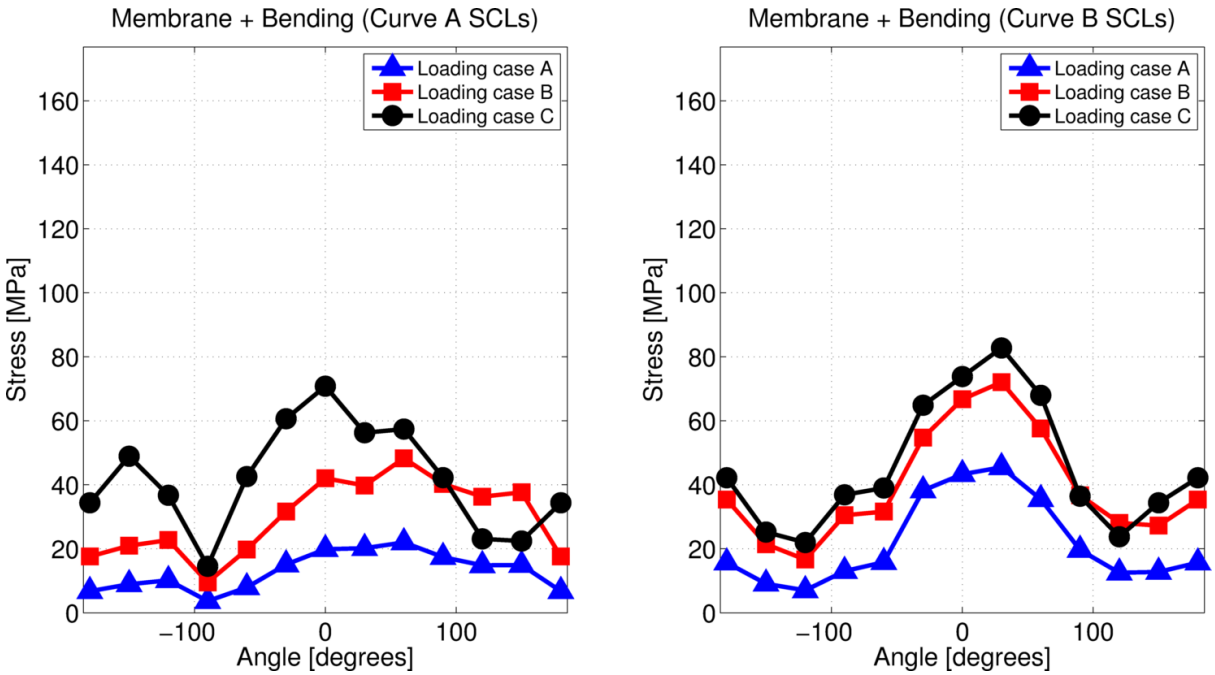

Figure 8-11: Membrane plus bending equivalent linearized stress around the circumference of the nozzle base, nozzle positioned at the end of the header box

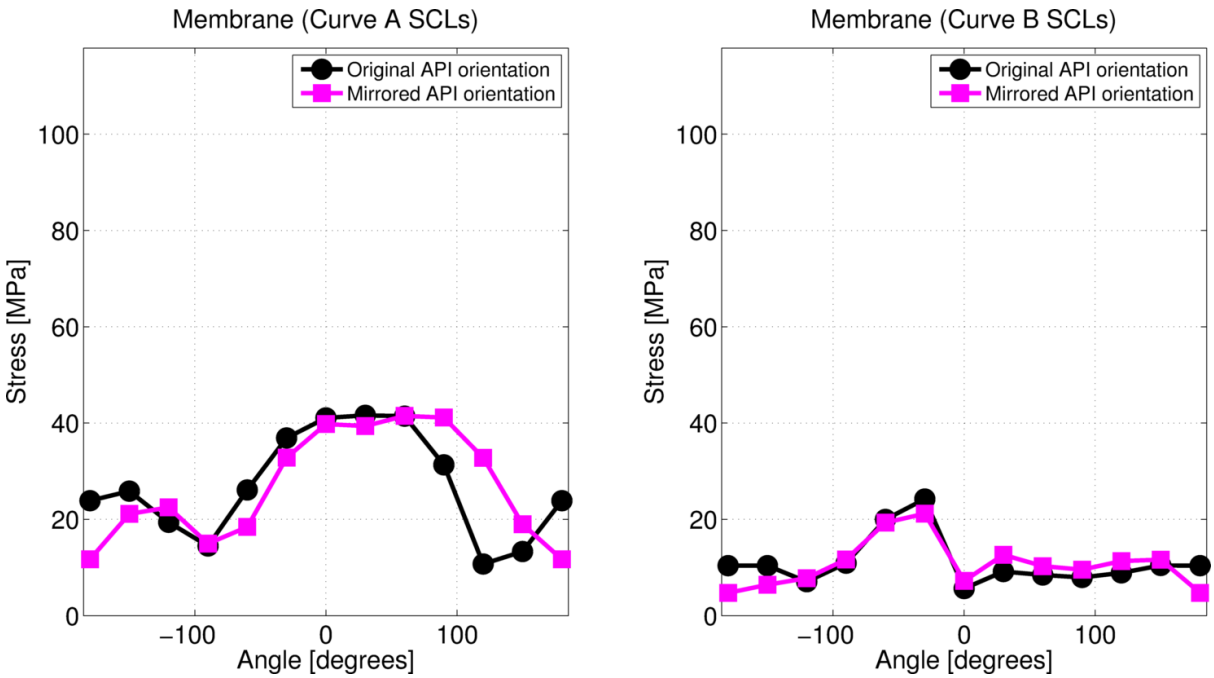

Figure 8-12: Comparison of the equivalent membrane linearized stress results for the end nozzle placement with reference to API load mirroring

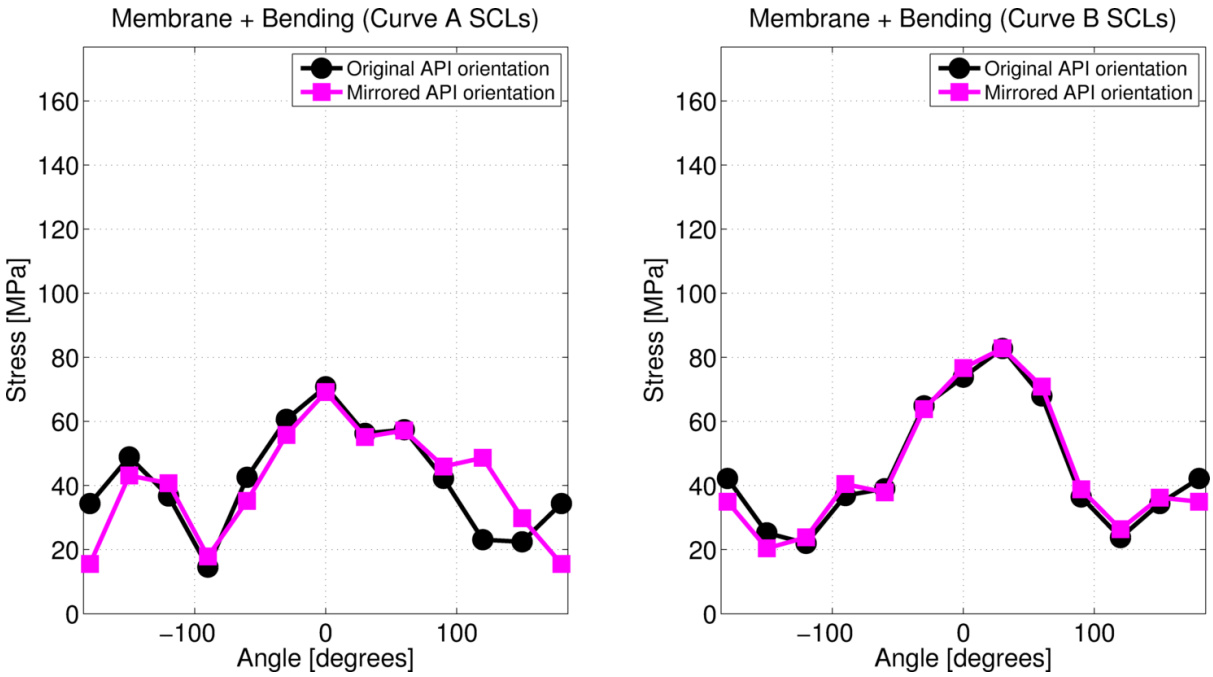

Figure 8-13: Comparison of the equivalent membrane linearized stress results for the end nozzle placement with reference to API load mirroring

8.2.3 Concluding remarks

The assumed nozzle loading resulted in a noticeable increase in stress at the root of the nozzle when added to the bolt pre-tension and pressure loading. It may however be noted that alternative orientations for nozzle loading may result in an even greater influence. The theme of Section 8.3 is therefore to identify a worst case nozzle loading configuration. In light of the fact that the centrally placed nozzle has been shown to produce more severe results, only this configuration is investigated.

8.3 Nozzle load orientation

To identify the worst-case nozzle loading orientation, the failure by plastic collapse criterion is once again implemented. The goal is to identify the nozzle loading scenario resulting in the greatest linearized membrane plus bending equivalent stress at the root of the nozzle, in combination with bolt pre-tension and pressure. To this end, the existing results of Section 8.2.1 will first be inspected to infer a nozzle loading orientation having the greatest additive effect (see Section 8.3.1). This orientation is further investigated by means of optimization in Section 8.3.2, whereupon results are discussed in Section 8.3.3.

For the purposes of this study, the nozzle loading of API 661 [1] is reconfigured to have maximum effect. Forces acting within the plane representing the face of the nozzle are considered separately from the forces normal to the face. The vector sum of the X and Y components of force and moment given in API 661 [1] can realistically be enforced in an arbitrary orientation around the circumference

of the nozzle, whereas the Z components can either act in the positive or negative sense. Figures 8-14 and 8-15 respectively illustrate the loading configurations of the forces and moments. Note that the right-hand rule is followed for the moment loads. With this representation, the orientation of worst case loading becomes a function of four variables, namely: the angles (θ_1 and θ_2) to which the respectively summed X and Y components of force and moment load must be oriented; as well as the scaling factors β_1 and β_2 which determine whether the Z components must be applied in the positive or negative orientation ($-1 \leq \beta_1, \beta_2 \leq 1$).

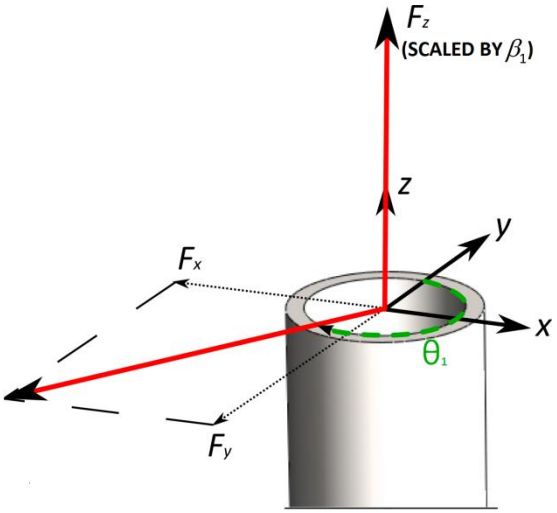

Figure 8-14: Forces imposed as part of nozzle loading

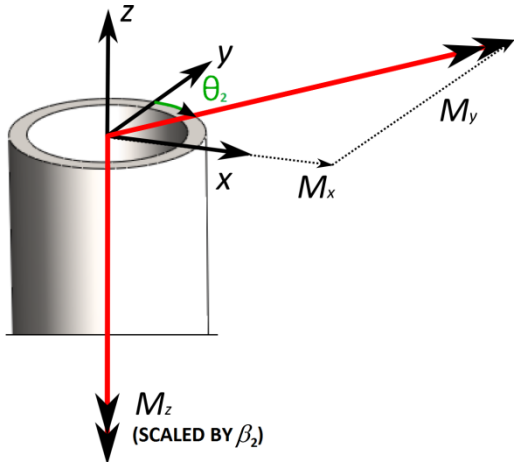

Figure 8-15: Moments imposed as part of nozzle loading

8.3.1 Identification by inspection of existing results

Von Mises equivalent stress values are evaluated for the failure by plastic collapse criteria. It therefore proves difficult to make inferences on the method by which bolt pre-tension and pressure loading act to induce stress at the nozzle root. By rather looking at stress components, and identifying those of greatest significance, an argument can be made as to which nozzle load orientation provides the best supporting effect (i.e. increases significant components).

Figures 8-16 and 8-17 illustrate the linearized component stresses for the critical SCLs identified in Section 8.2.1 (see Table 8-2) subject to the superimposed loading of bolt pre-tension, pressure, and assumed API nozzle loading. It must however be stressed that the same SCLs proved critical for the instance of bolt pre-tension and pressure only. The contributions of bolt pre-tension, pressure and nozzle loading are furthermore shown independently in the figures, where the notation of the components correspond to the local coordinate system described in Figure 8-7. In Figure 8-17, the SCL across the side plate is seen to be dominated by bending stress. This is to be expected given the results of Chapter 7. In Figures 8-16, the membrane and bending components are however more comparable. In this case the SCL stretches across the nozzle wall.

An inference for a severe nozzle loading case can be made with respect to the results in Figure 8-16. By analogizing the nozzle to a cantilever beam, we can deduce the loading configuration of Figure

8-18 to have a substantial effect, in view of the relatively significant meridional stress component, and the location of the SCL. In this case, the force F_{xy} and moment M_{xy} act together in creating a bending stress at the root of the nozzle. A similar configuration can be speculated for the case of Figure 8-17. As a means for the rigorous identification of a worst-case nozzle loading, optimization is however implemented in Section 8.3.2. The configuration of Figure 8-18 is used as a starting point in identifying a worst-case membrane plus bending equivalent stress for respective cases of curve A and B at the root of the nozzle (see Figure 8-7).

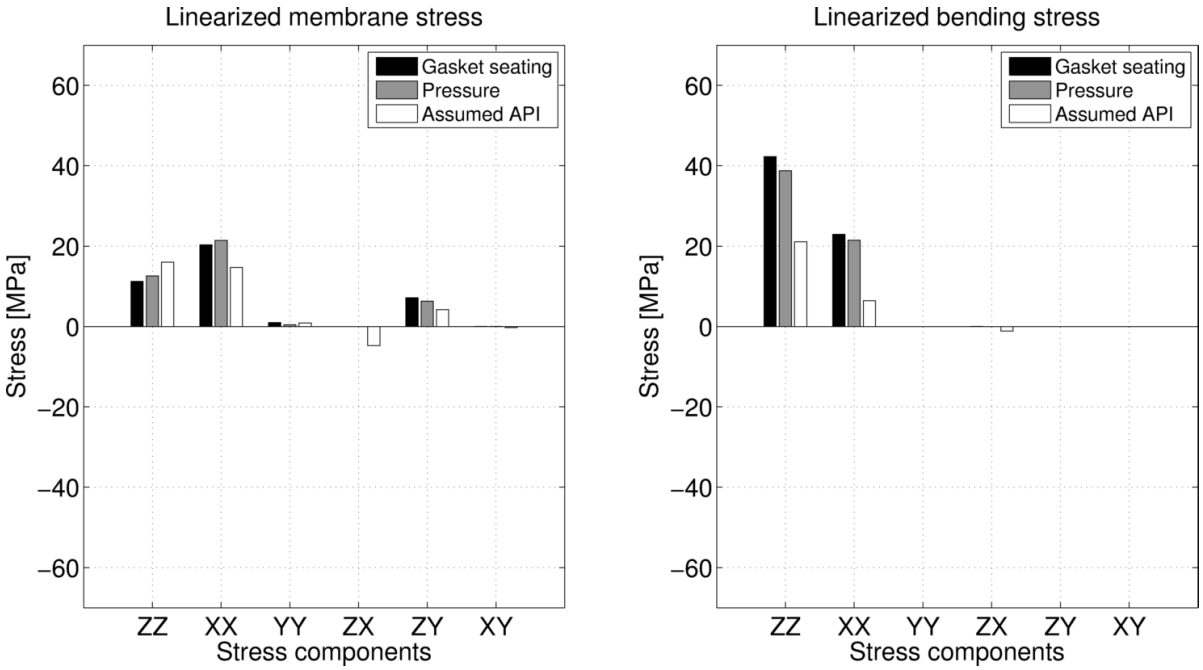

Figure 8-16: Component stress evaluation on curve A for most severe SCL (note that the stress components are as follows: ZZ – Meridional, XX – Hoop, YY – Through thickness, ZX – Torsion, ZY and XY – Shear)

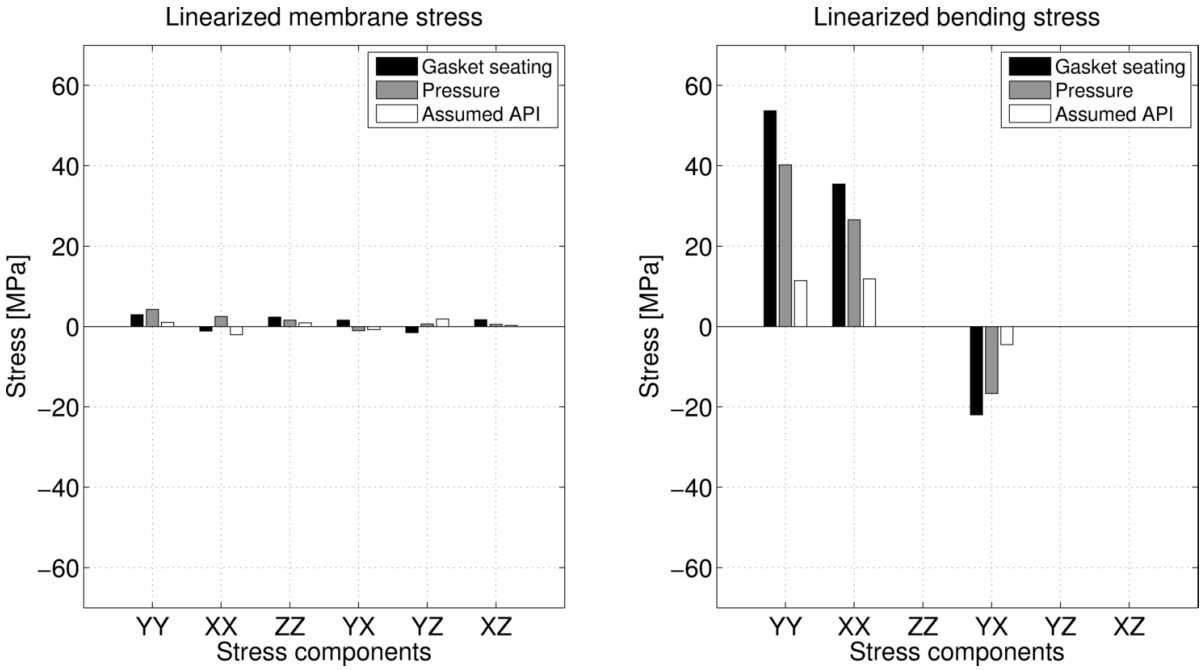

Figure 8-17: Component stress evaluation on curve B for most severe SCL (note that the stress components are as follows; YY – Meridional, YY – Hoop, ZZ – Through thickness, YX – Torsion, YZ and XZ – Shear)

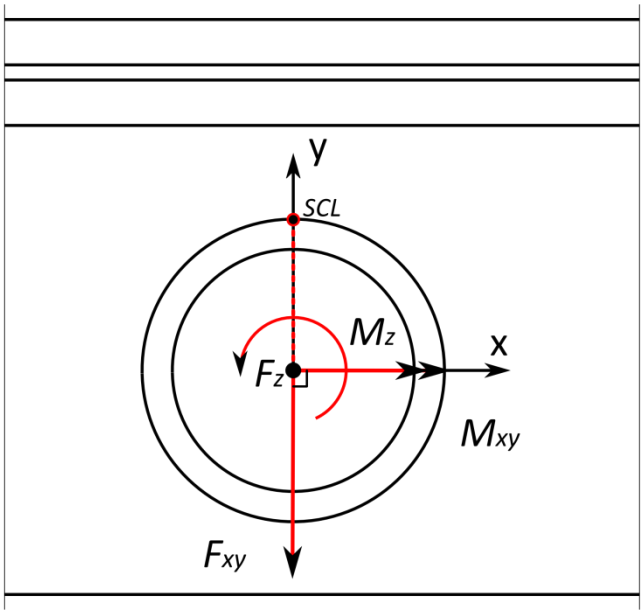

Figure 8-18: Top view of a deduced severe nozzle loading configuration

8.3.2 Additional optimization study

In this section, worst case nozzle load orientations are respectively identified for SCLs corresponding to the planes of curve A and B in Figure 8-7 by means of optimization. For each of these planes a total of twelve uniformly spaced SCLs are evaluated around the circumference of the nozzle. The variables which are optimized include the two angles (θ_1 & θ_2), and two scaling factors (β_1 & β_2) illustrated in Figures 8-14 and 8-15.

The objective is to maximize the maximum combined equivalent stress resulting from the twelve SCLs for the case of each plane (note that the stresses resulting at each of the SCLs is denoted by σ_i, where i = 1, 2, ..., 12). A summarized mathematical expression for the optimization problem is illustrated below.

$$\underset{\text{w.r.t. } \underline{\theta},\underline{\beta}}{\text{maximize}} \quad f = \max\left(\sigma_i\right)$$

$$\text{where} \quad \sigma_i = f\left(\underline{\theta},\underline{\beta}\right) \quad i = 1,2,\ldots,12$$

$$\underline{\theta} = \left[\theta_1,\theta_2\right]^T \in \mathbb{R}^2$$

$$\underline{\beta} = \left[\beta_1,\beta_2\right]^T \in \mathbb{R}^2$$

subject to the constraints:

$$-1 \le \beta_1 \le +1$$

$$-1 \le \beta_2 \le +1$$

To further clarify the use of the angles and scaling factors, the vector expressions for the overall force and moment applied to the nozzle are given by Equations (8-1) and (8-2).

$$\underline{F} = \left(F_{xy} \times \sin\theta_1\right)\hat{e}_x + \left(F_{xy} \times \cos\theta_2\right)\hat{e}_y + \left(F_z \times \beta_1\right)\hat{e}_z \quad \textbf{(8-1)}$$

$$\underline{M} = \left(M_{xy} \times \sin\theta_1\right)\hat{e}_x + \left(M_{xy} \times \cos\theta_2\right)\hat{e}_y + \left(F_z \times \beta_1\right)\hat{e}_z \quad \textbf{(8-2)}$$

The MATLAB optimization toolbox [23] was used to find the optimal load configuration via the function `fmincon`. This function allows for the constrained optimization of a multivariable function via a number of algorithms. In the case of the present study, the method of sequential quadratic programming (SQP) is adopted. As the name implies, this method requires a quadratic programming (QP) sub problem to be solved at successive iterations.

To allow automatic evaluation of a certain nozzle loading configuration in MSC.Patran [17,18] and MSC.Nastran [17,18], Patran Command Language (PCL) was utilised. In this approach, an existing MSC.Patran database containing the finite element model of the header box is edited, analyzed and used for results extraction. This entire process is run from the command line by means of a session file. By editing this session file in MATLAB [23], the nozzle loads may be altered as required for each objective function evaluation. Simply put, this session file opens an existing database of the header box, creates an appropriate nozzle loading, analyzes the model, and interpolates twelve uniformly spaced SCLs originating on curve A or B. Once the interpolated results have been generated, they are returned to MATLAB [23] for post-processing (i.e. linearization is performed and the objective stress value is calculated).

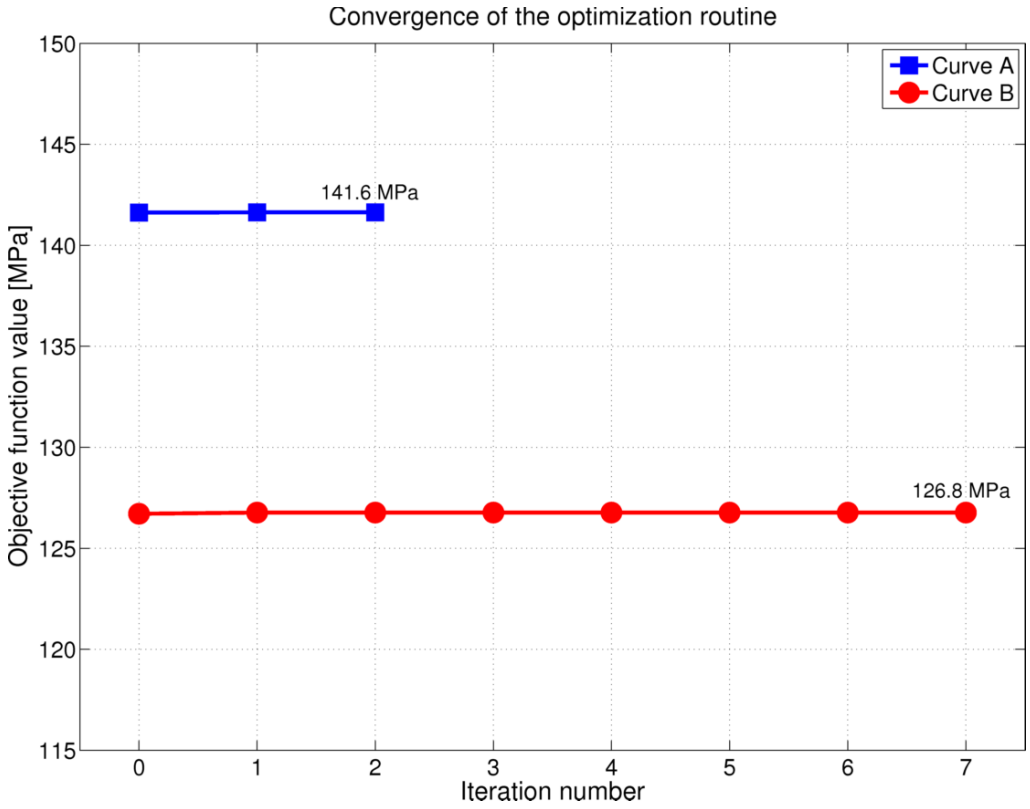

Figure 8-19: Convergence of the optimization routine based on combined stress at the root of the nozzle (coarse mesh)

The coarse mesh configuration was used for optimization. It allows for faster function evaluations without significant reduction in accuracy. Convergence of the optimization routine is furthermore based on the absolute change in the objective function value per iteration (tolerance of 10^{-3} MPa). Selecting the initial guess as the intuitive configuration of Figure 8-18, the convergence graphs illustrated in Figure 8-19 were obtained for optimization based on curve A and B. The corresponding optimal orientation variables are further summarized in Table 8-4.

Table 8-4: Optimized variables for nozzle loading orientation (coarse mesh)

Variables	Initial guess	Optimized variables	
		Curve A	*Curve B*
θ_1	180°	180.7°	183.4°
θ_2	90°	91.8°	95.5°
β_1	1.0	1.0	1.0
β_2	-1.0	-1.0	-1.0

There is little difference between the optimized and initial orientation variables for both cases. The scaling factors β_1 and β_2 remain unchanged, having the greatest impact when respectively directed in their positive and negative orientations. The angles θ_1 and θ_2 on the other hand vary by a few degrees from the initial guess. As expected, these angles furthermore differ by approximately 90°, so as to allow the bending efforts of F_{xy} and M_{xy} to complement one another. In Section 8.3.3 to follow, stress results for the optimal orientation variables are presented for the fine mesh.

8.3.3 Results

The nozzle load orientations of Table 8-4 were superimposed upon the gasket seating and pressure loading conditions for application to the refined finite element model. Peak results for the corresponding equivalent membrane plus bending stresses are included in Table 8-5, and are given priority over membrane-only results due to their superior criticality. The peak results for the optimized orientations are within 0.05 % of the initial guess result for curve A, and 0.06 % for curve B. Since these differences are small, the initial guess orientations are sufficient for further study. Results for this scenario are furthermore compared in Figure 8-20 against those of loading case C in Figure 8-9.

Table 8-5: Peak membrane plus bending results [MPa] at root of the nozzle

Associated curve	Nozzle load orientation case		
	Initial guess	*Optimized (Curve A)*	*Optimized (Curve B)*
Curve A	142.267	142.275	142.200
Curve B	126.897	126.930	126.970

The increase in peak stress at the nozzle root for the addition of nozzle loading to bolt pre-tension and pressure is summarized in Table 8-6. In the case of curve A, optimal loading results in a rise of 44.7 %, whereas the originally assumed API loading provides a rise of 32.2 %. On the other hand, increases of 17.2 % and 12.1 % respectively result for curve B.

Table 8-6: Comparison of the peak stress [MPa] results at the root of the nozzle for a number of loading scenarios

Loading scenario	Curve A	Curve B
1 (See note)	98.33	108.25
2 (See note)	(+32.2 %) 130.00	(+12.1 %) 121.35
3 (See note)	(+44.7 %) **142.27**	(+17.2 %) **126.90**

Note. The loading scenarios are:
1 - Superimposed bolt pre-tension and pressure;
2 - Superimposed bolt pre-tension, pressure and assumed API nozzle load;
3 - Superimposed bolt pre-tension, pressure and optimized nozzle load.

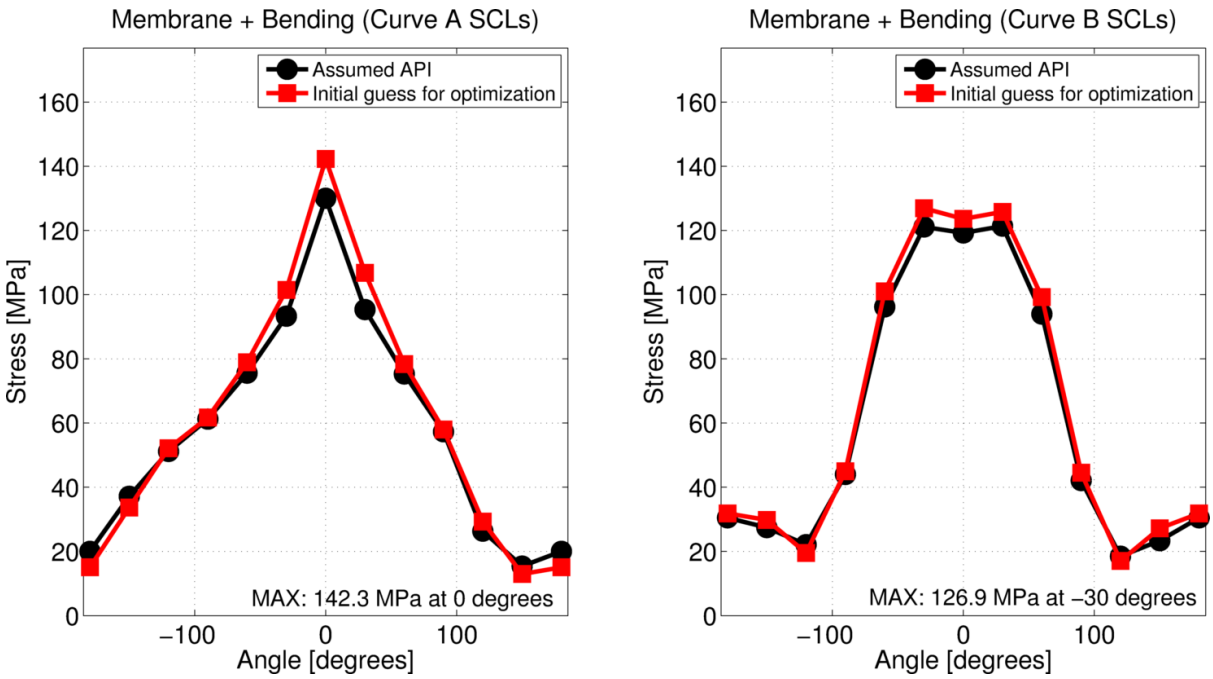

Figure 8-20: Comparison of combined equivalent stress at nozzle root for two nozzle loading scenarios with superimposed bolt pre-tension and pressure

8.3.4 Concluding remarks

From the results, it can be concluded that nozzle loading has a significant influence on the stress resulting at the root of the nozzle, where it is important to implement it with the correct orientations. In this case, the SCL located at zero degrees (refer to θ in Figure 8-7), and stretching across the thickness of the nozzle wall was shown to be most critical. It is furthermore interesting to note the manner in which the corresponding worst-case nozzle loading is implemented. The most significant forces and moments typically orient themselves in such a manner so as to lie in a symmetry plane at the centre of the header box length. This is conducive towards two-dimensional analysis and supports the development of an alternative design by rule approach. The rigid frame model can therefore be modified to include an approximate representation of these loads.

8.4 Comparison of the design approaches in view of a nozzle attachment

In this section, the nozzle loading results are discussed in the light of the current design approach and rigid frame solution. The design of the side plate and nozzle wall thicknesses is emphasized.

8.4.1 Design of the side plate

A summary of results for the side plate is presented in Table 8-7 for the current design approach, rigid frame solution and design by analysis. It is important to once again note that the bolt pre-tension calculation for the FEM was based on the major bolt diameter (see Section 6.2.3). This necessitated the adjustment of the results for the current design approach and rigid frame solution in Chapter 7. In the case of the current design approach, an acceptable stress of 154.3 MPa is calculated. Note that the allowable is 176.85 MPa. This result is also conservative in comparison to the design by analysis case, which implicates worst-case nozzle loading.

Table 8-7: A summary of numerous combined stress results for the design of the side plate

Design approach	Stress [MPa]	Total bolt load calculation	Location	Nozzle consideration
Current design approach	154.3	Eqn. (4-18)	Centre	Efficiency factor E_n
Rigid frame model	170.0	Eqn. (4-19)	Centre	Efficiency factor E_n
Rigid frame model	138.9	Eqn. (4-19)	Junction to flange	None
Design by analysis (FEA)	**126.9**	**-**	**-**	**-**

Similarly, the rigid frame model provides conservative results. With nozzle loading excluded, the stress predicted at the junction to the flange is 138.9 MPa, whereas the stress at the centre of the side plate is 170.0 MPa (including E_n).

8.4.2 Design of the nozzle wall thickness

In Chapter 4, the thickness of the nozzle wall was seen to be dictated by the requirements of API 661 [1], where minimum values are presented. These minimum values typically correspond to the largest schedule number (a form of strength classification) in piping standards such as ASME B36.10M [10]. For this selection, the addition of nozzle loading resulted in an acceptable stress of 142.3 MPa. This also proved to be the most critical result at the root of the nozzle.

9 Concluding remarks

The present study dealt with the design of removable cover-plate header boxes for air-cooled heat exchangers. It was intended to perform a critical evaluation of a design process currently adopted in industry via finite element analysis of an example configuration.

The current design approach is illustrated in Chapter 4 at the hand of the example design. In this approach, the header box is viewed in a two-dimensional perspective, whereby each of the constituent plates is represented via a simply supported beam. As an alternative means for predicting the stress response of the header box bonnet, rigid frame theory was subsequently investigated in Chapter 5. Hereby, the plates comprising the header box bonnet may be dealt with collectively. Finally, in Chapter 6, the details surrounding a finite element model were elaborated upon.

In Chapter 7, numerous results in the absence of a nozzle attachment were compared for design by rule, as well as design by analysis. Upon investigation of a number of rigid frame configurations, a variant incorporating flange arms and having constrained supports was seen to provide reasonable correspondence with the FEM results. This served the purpose of providing some assurance in the FEM, as well as advancement towards the development of an alternative method for design by rule. Upon drawing further comparisons, the current design approach was observed to provide conservative solutions at most failure locations in comparison with the FEM. However, for the design of the side plate, conservatism only results once the nozzle efficiency factor is included. The rigid frame model on the other hand provided conservative results throughout. In addition, the results for the tube sheet were less conservative than for the current design approach. Further results for design by analysis presented an opportunity for even less conservative design, and allowed for a broader investigation of the stress results.

In Chapter 8, a single nozzle attachment was investigated by means of FEM. Placing the nozzle at the centre of the header box was shown to have the greatest severity. Nozzle loading was further shown to have a marked influence on the results at the root of the nozzle, where a worst-case configuration was identified. Importantly, both the current design approach and rigid frame solution illustrated conservative results in comparison to design by analysis for the FEM.

In general, the current design approach may be concluded to provide a conservative solution, whereas rigid frame modelling presents an opportunity for more effective design, since it provided closer correspondence with the FEM.

10 Suggestions for further work

As an ultimate outcome, the development of a rigorous design by rule approach should be pursued. It would provide for a structured manner towards carrying out header box designs. Before this may be achieved however, improved understanding of a number of aspects is required. A couple of examples are the influence of partition plates as well as perforations on the tube sheet. The question arises whether these aspects may be addressed and incorporated into the rigid frame model presented in the present body of work in addition to nozzle loading.

In all likelihood, partition plates would not have a significant influence when the header box is of a long enough length for it to be appropriate to consider a plane strain model, since the partition plate and removable cover are disconnected. The manner in which it interacts with the end plates however remains in doubt, and could prove challenging to deal with in a design by rule approach. What is more, a pressure difference may be introduced across the partition plate as a result of distinct pressures in each of the compartments.

The perforations to be included for a tube sheet on the other hand effectively represent a reduction in stiffness. The ASME code [5] does offer an approach whereby the perforations are discarded, and a solid plate of effective stiffness properties is modelled instead. Since a statically indeterminate problem is solved for in the rigid frame model, which is typically displacement controlled, Young's modulus features in the calculation. It should therefore not be an infeasible task for the tube sheet segment to be given an effective stiffness value.

It may also have been noted that for a centrally placed nozzle the worst case loading should be oriented in a manner which complements a two-dimensional interpretation of the header box. This characteristic may be used advantageously by altering the rigid frame model to incorporate approximate representations of nozzle loading. Doing so would allow for the header box bonnet's stress distribution to be investigated, whereby particularly important locations such as at the junction to the flange may be evaluated. Ideally one would like to establish a rigid frame solution which may be characterized as being conservative under all circumstances. Further developing an alternative method for evaluating stress results associated with the nozzle wall may prove particularly challenging.

Finally, results extraction via the linear elastic design by analysis method can be tedious, as it is not suited to comprehensively consider many of the locations which are of concern, such as the corner junction formed by the flange, end plate and side plate. It would therefore be interesting if a nonlinear design method could be conducted, e.g. limit-load and elastic plastic methods. The results for such an investigation may be compared with the linear elastic results to establish a design characterized by an even lower level of conservatism.

11 Bibliography

[1] API, *Air-Cooled Heat Exchangers for General Refinery Service*, 6th ed. Washington D.C.: API Publishing Services, 2006.

[2] Detlev G. Kröger, *Air-cooled heat exchangers and cooling towers: thermal-flow performance evaluation and design*. Tulsa: PennWell Corporation, 2004.

[3] Michael J. Nee, *Heat exchanger engineering techniques: process, air conditioning, and electronic systems*. New York: ASME Press, 2003.

[4] I.F. Lombaard, Personal communciation, June 4, 2010.

[5] ASME, *2007 ASME Boiler & Pressure Vessel Code, Section VIII, Rules for construction of Pressure Vessels, 6th Edition*. New York: The American Society of Mechanical Engineers, 2007.

[6] Engineering Systems. (2009) Optivessel Version 2.0 [Build 0080]. Mechanical engineering design software.

[7] National Nuclear Security Administration. (2005, September) SG100 Revision 2 - Design and Development Guide for NNSA Type B Packages. [Online]. http://www.doeal.gov/nnsaota/SafetyGuides/SG100Revision2/SG100Revision2.htm

[8] Department of labour, Republic of South Africa, Occupational health and safety act, 1993 (Act No. 85 of 1993), Pressure vessel regulations.

[9] J. L. Hechmer and G. L. Hollinger, *3D stress criteria guidelines for application*. New York: Welding research council, inc., 1998.

[10] ASME, *Welded and seamless wrought steel pipe: ASME B36.10M-2004*. New York: The American Society of Mechanical Engineers, 2004.

[11] Tubular Exchanger Manufacturers Associated, inc., *Standards of tubular exchanger manufacturers association.*, 5th ed. New York: Tubular Exchanger Manufacturers Association., 1968.

[12] Bharat Batra, "Design of a large rectangular flange," in *11th International Conference on Pressure Vessel Technology*, Vancouver, 2006.

[13] Joseph E. Shigley, Charles R. Mischke, and Richard G. Budynas, *Mechanical Engineering Design*, 7th ed. Singapore: McGraw-Hill Education (Asia), 2004.

[14] Charles, Head Norris, John, Benson Wilbur, and Senol Utku, *Elementary structural analysis*, 3rd ed. New York: McGraw-Hill, 1976.

[15] William Griffel, *Handbook of formulas for stress and strain*. New York: Frederick Ungar Publishing Co., 1966.

[16] R. C. Hibbeler, *Mechanics of Materials; SI Second Edition*. Singapore: Prentice Hall, 2005.

[17] MSC.Software Corporation, Advanced Patran, PAT302 Course Notes, 2007.

[18] MSC.Software Corporation, Linear Static, Normal Modes, and Buckling Analysis Using MSC.Nastran and MSC.Patran, NAS120 Course Notes, 2006.

[19] A.Th. Diamantoudis and Th. Kermanidis, "Design by analysis versus design by formula of high strength steel pressure vessels: a comparative study," *International Journal of Pressure Vessels and Pipiping*, pp. 43-50, 2004.

[20] Kim Jeong, Yoon Joo-Cheol, and Kang Beom-Soo, "Finite element analysis and modeling of structure with bolted joints," *Applied mathematical modelling*, pp. 895-911, 2007.

[21] JJ Williams (Gaskets) Ltd. (2010, November) Reinforced graphite gaskets. [Online]. http://www.jjwilliams.co.uk/graphite.htm

[22] Woo-Seok Choi, Tae-Wan Kim, and Ki-Seong Seo, "Shape optimization of a perforated pressure vessel cover under linearized stress constraints," *Nuclear Engineering and Design*, pp. 2468-2472, 2008.

[23] MathWorks. (2008, March) Matlab Optimisation Toolbox User's Guide Version 4.0. Document.

[24] M Qadir and D Redekop, "SCF analysis of a pressurized vessel-nozzle intersection with wall thinning damage," *International Journal of Pressure Vessels and Piping*, pp. 541-549, 2009.

[25] Henry H. Bednar, *Pressure vessel design handbook*. New York: Van Nostrand Reinhold Company Inc., 1981.

[26] Haofeng Chen and Alan R.S. Porter, "Structural integrity assessment of superheater outlet penetration tubeplate," *International Journal of Pressure Vessels and Piping*, pp. 412-419, 2009.

[27] J.G. Williams, R.E. Anley, D.H. Nash, and T.G.F. Gray, "Analysis of externally loaded bolted joints: Analytical, computational and experimental study," *International Journal of Pressure Vessels and Piping*, pp. 420-427, 2009.

[28] T. Aseer Brabin, T. Christopher, and B. Nagaswara Rao, "Finite element analysis of cylindrical pressure vessels having a misalignment in a circumferential joint," *International Journal of Pressure Vessels and Piping*, pp. 197-201, 2010.

[29] Jan A. Snyman, *Practical mathematical optimization, an introduction to basic optimization theory and classical and new gradient-based algorithms*. Pretoria, South Africa: Springer, 2005.

[30] ESTEQ Engineering, ASME Patran Plug-in, 2006, Source code for an ASME Utility to perform interpolation and linearization in Patran.

[31] Pressure Vessel Engineering Ltd. (2010) The Nuts and Bolts of Stress Linearization (With an Educational and Functional Stress Linearization Utility). [Online]. http://www.pveng.com

[32] Richard L. Burden and J. Douglas Faires, *Numerical Analysis*, 8th ed. Belmont, USA: Thomson Brooks/Cole, 2005.

[33] Schalk Kok, "Rapid heating and cooling of pressure vessels through optimal temperture control: a general methodology," University of Pretoria, Pretoria, South Africa, Masters Thesis 1996.

Appendix A: Additional details of the rigid frame models

A.1 Comparative plots for the unconstrained flanged frame model

Figure A-1 illustrates the maximum combined stress from a FEM solution of the unconstrained flanged frame model, superimposed upon a deformation plot. In Figure A-2, this solution is furthermore compared to the analytical solution discussed in Section 5.1.2.

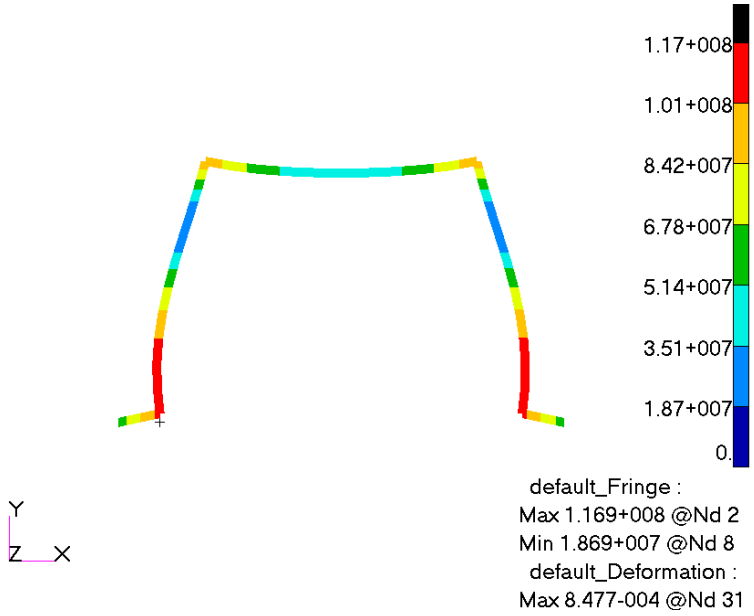

Figure A-1: Maximum combined stress for unconstrained hinged supports (deformation scaled by a factor of 100)

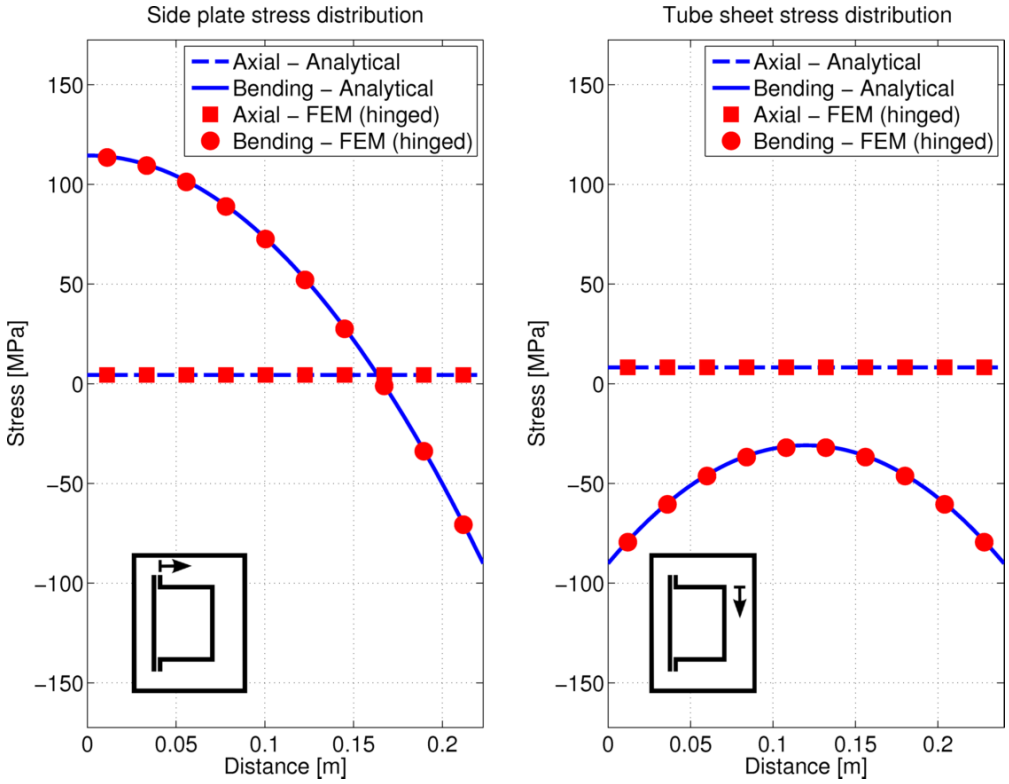

Figure A-2: Stress distribution for the unconstrained flanged rigid frame model

A.2 Simple frame models

In this section the details of the simple rigid frame models, which exclude flange arms, are elaborated upon.

A.2.1 Constrained hinged supports model

- ***Solution to the bolt loading problem***

As for the equivalent flanged frame model in Section 5.1.1, it is necessary to introduce a "dummy" load so as to evaluate two statically determinate problems. In this case, the reaction force H_2 is used, as illustrated by Figure A-3 and A-4 for the case of bolt loading.

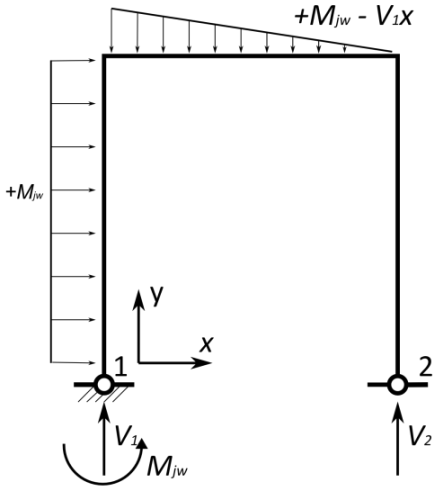

Figure A-3: Bending moment diagram A

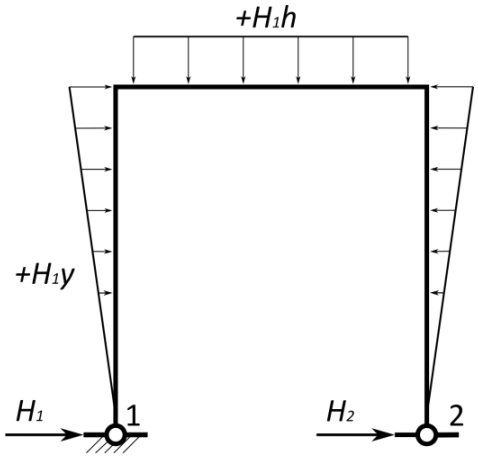

Figure A-4: Bending moment diagram B

Once the reaction forces for each case have been identified, the theory of elastic energy may be enforced to identify the reaction forces by means of an overall displacement requirement. This derivation is included below, with an explicit expression for H_1 being provided in Equation (A-1). The remaining reaction forces (V_1, V_2 and H_2) may be identified from equilibrium.

$$t_A + t_B = 0$$

$$\left[\frac{1}{EI_1}\int_0^h M_{jw} y\,dy + \frac{1}{EI_2}\int_0^L (M_{jw} - \frac{M_{jw}}{L}x)h\,dx\right] + \left[2\int_0^h \frac{H_1 y^2}{EI_1}dy + \int_0^L \frac{H_1 h^2}{EI_2}dx\right] = 0$$

$$H_1 = \frac{M_{jw}\left[-h^2/2I_1 - hL/2I_2\right]}{2h^3/3I_1 + Lh^2/I_2} \qquad \textbf{(A-1)}$$

- ***Solution to the pressure loading problem***

The solution to the case of pressure loading follows by the same technique as for bolt loading above. An expression for H_1 for this scenario is once again provided in Equation (A-2).

$$H_1 = \frac{Ph^4/4I_1 + PLh^3/2I_2 - PL^3h/12I_2}{2h^3/3I_1 + Lh^2/I_2} \quad \textbf{(A-2)}$$

- ***Superimposed solutions compared to 1D FEM***

Figure A-5 illustrates the maximum combined stress from a FEM solution superimposed upon a deformation plot, whereas Figure A-6 compares it with the analytical solution.

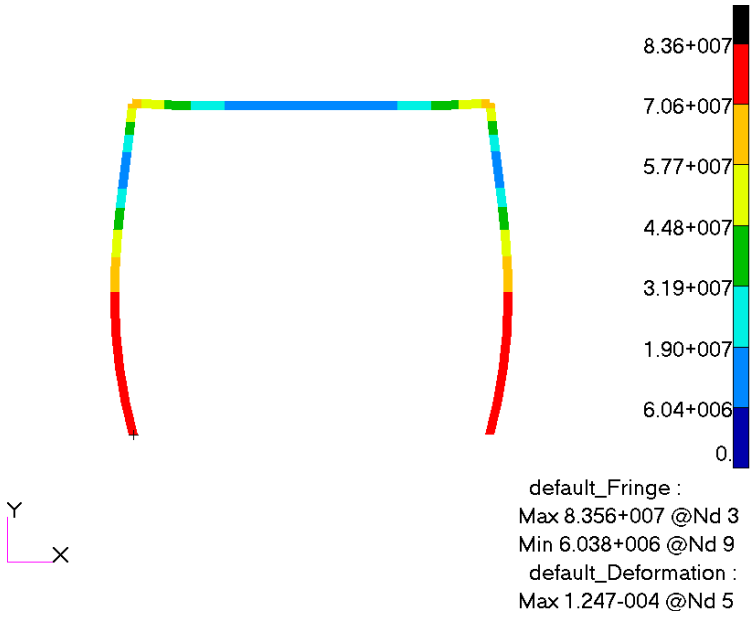

Figure A-5: Hinged supports maximum combined stress (deformation scaled by a factor of 100)

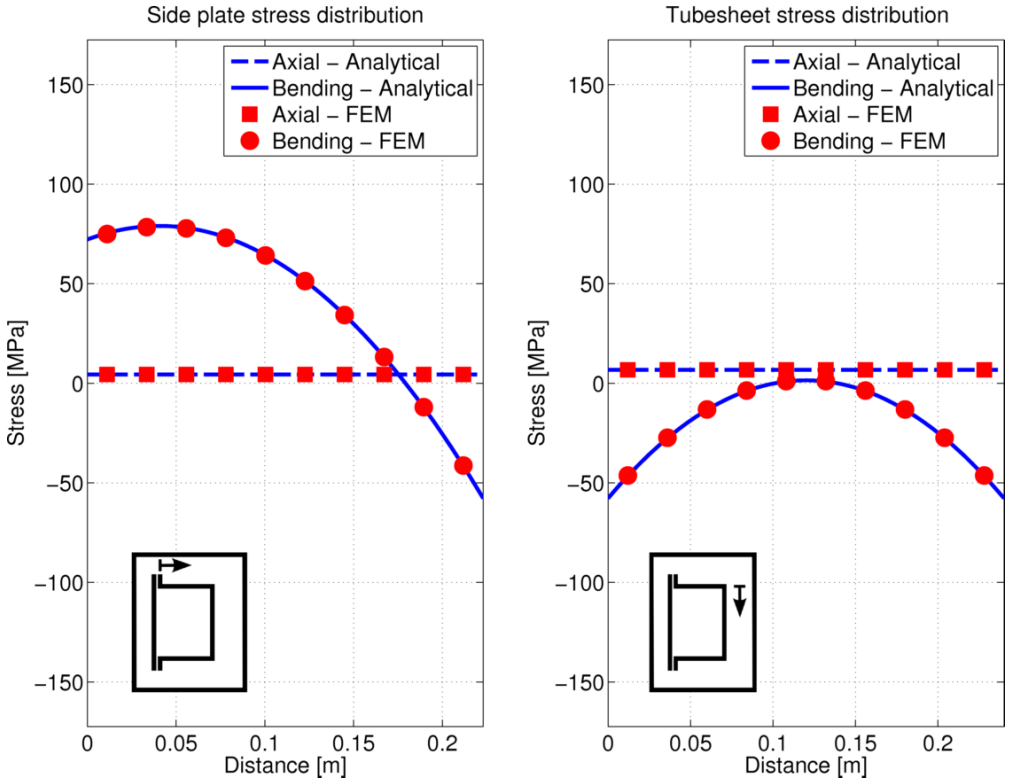

Figure A-6: Rigid frame stress distribution for hinged supports

A.2.2 Constrained fixed supports model

- ***Solution to the pressure loading problem***

As mentioned in Section 5.2.1.2, the two scenarios which may be superimposed from Griffel [15] are depicted in Figure A-7 to solve the pressure loading problem.

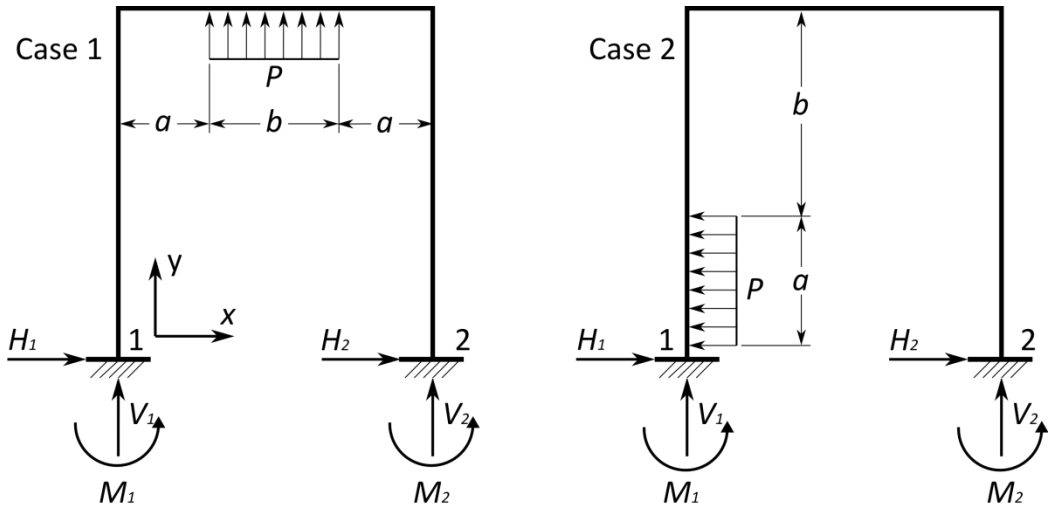

Figure A-7: Superimposed scenarios for fixed supports (adapted from [15])

The internal pressure load may be represented through simply extending the application region of the distributed load in Case 1 of Figure A-7 to where a = 0 and further evaluating Case 2 symmetrically for either side plate with the distributed load once again expanded (b = 0). Each of these cases will now be dealt with individually after which superposition will be performed. Note that the following frame constants apply:

$$C=\frac{I_2}{I_1}\left(\frac{h}{L}\right);\ D=2+C;\ E=1+6C \text{ and } K=\frac{1}{3+2C}.$$

Case 1:

The following solutions for reactions are presented in Griffel [15]:

$$M_1, M_2 = \pm\frac{P\times b\times(3L^2-b^2)}{24L\times D}; \quad \textbf{(A-3)}$$

$$H_1, H_2 = \mp\frac{3M_1}{h}; \quad \textbf{(A-4)}$$

$$V_1, V_2 = -\frac{Pb}{2}. \quad \textbf{(A-5)}$$

These may be modified through setting b = L to use for evaluation of the full internal pressure. By doing so, the following is reactions are obtained:

$$M_1, M_2 = \pm \frac{P \times L^2}{12D}; \quad \textbf{(A-6)}$$

$$H_1, H_2 = \mp \frac{3M_1}{h}; \quad \textbf{(A-7)}$$

$$V_1, V_2 = -\frac{PL}{2}. \quad \textbf{(A-8)}$$

Case 2:

Similarly, the following solutions are represented for the reactions in Case 2:

$$M_1, M_2 = \pm \frac{Pa^3}{h}\left\{\frac{C}{24D}\left[\left(8+\frac{6}{C}\right)-\frac{3a}{h}\left(1+\frac{3}{C}\right)-\frac{6h}{a}\right] \mp \left[\frac{h}{4a}-\frac{C}{2E}\right]\right\}; \quad \textbf{(A-9)}$$

$$H_2 = \frac{Pa^2}{h}\left\{\frac{1}{4}+\frac{C}{24D}\left[6-3\frac{a^2}{h^2}-\left(2-\frac{a}{h}\right)^2\left(3+\frac{3}{C}\right)\right]\right\}; \quad \textbf{(A-10)}$$

$$H_1 = Pa - H_2; \quad \textbf{(A-11)}$$

$$V_2 = -\frac{Pa^3 C}{hLE}; \quad \textbf{(A-12)}$$

$$V_1 = +\frac{Pa^3 C}{hLE}. \quad \textbf{(A-13)}$$

It now becomes necessary to implement these reaction forces in such a way so as to solve a scenario where the distributed load is applied on the inside of both of the side plates. This may be achieved through simply superimposing the solutions for full distributed load application on either side plate, whilst maintaining the depicted sign convention for the reactions. First reducing the reaction forces and moments for a case of full side plate action is achieved by setting $a = h$ and simplifying:

$$M_1, M_2 = \pm Ph^2\left\{\frac{C}{24D}\left[\left(8+\frac{6}{C}\right)-3\left(1+\frac{3}{C}\right)-6\right] \mp \left[\frac{1}{4}-\frac{C}{2E}\right]\right\}; \quad \textbf{(A-14)}$$

$$H_2 = Ph\left\{\frac{1}{4}+\frac{C}{24D}\left(\frac{-3}{C}\right)\right\}; \quad \textbf{(A-15)}$$

$$H_1 = Ph - H_2; \quad \textbf{(A-16)}$$

$$V_2 = -\frac{Ph^2 C}{LE}; \quad \textbf{(A-17)}$$

$$V_1 = +\frac{Ph^2 C}{LE}. \quad \textbf{(A-18)}$$

The mentioned symmetrical application with maintained sign convention further results in the following reactions:

$$M_1, M_2 = \pm Ph^2 \left\{ \frac{C}{12D} \left[\left(8 + \frac{6}{C} \right) - 3\left(1 + \frac{3}{C} \right) - 6 \right] \right\}; \quad \textbf{(A-19)}$$

$$H_1, H_2 = \pm Ph \left\{ \frac{1}{2} - \frac{C}{12D} \left(\frac{-3}{C} \right) \right\}; \quad \textbf{(A-20)}$$

$$V_1, V_2 = 0. \quad \textbf{(A-21)}$$

Superposition of cases:

Finally, the cases may be superimposed to represent the entirety of the internal pressure loading. The consequent reactions are as follows:

$$M_1, M_2 = \pm \frac{P \times L^2}{12D} \pm Ph^2 \left\{ \frac{-C}{12D} \left[1 + \frac{3}{C} \right] \right\}; \quad \textbf{(A-22)}$$

$$H_1, H_2 = \mp \frac{P \times L^2}{4hD} \pm Ph \left\{ \frac{1}{2} + \frac{1}{4D} \right\}; \quad \textbf{(A-23)}$$

$$V_1, V_2 = \frac{-PL}{2}. \quad \textbf{(A-24)}$$

- ***Superimposed solutions compared to 1D FEM***

Using the reactions in Equations (A-22) through (A-24), the nominal stress distribution throughout the frame can be found. To further establish the validity of these expressions, comparisons with a one-dimensional beam model were made. In Figure A-8 and A-9, the maximum combined stress distributions from the FEM solution may be observed for the respective loading scenarios. These results are superimposed on deformation plots. In Figure A-10, the superimposed FEM solution is furthermore compared with the analytical solution.

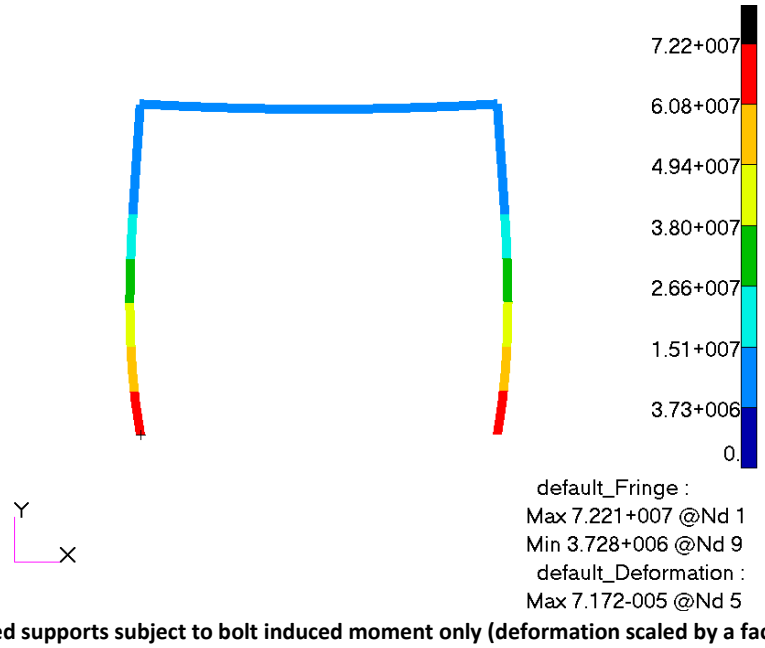

Figure A-8: Hinged supports subject to bolt induced moment only (deformation scaled by a factor of 100)

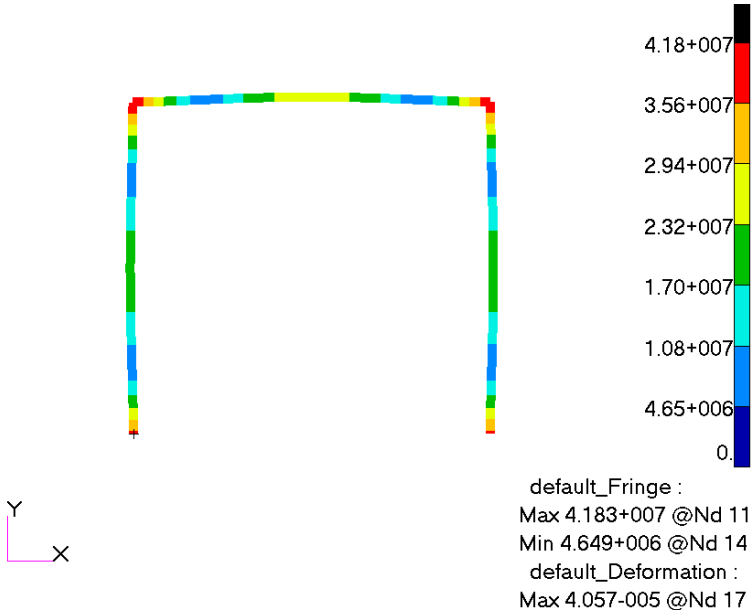

Figure A-9: Constrained fixed supports scenario subject to pressure load only (deformation scaled by a factor of 100)

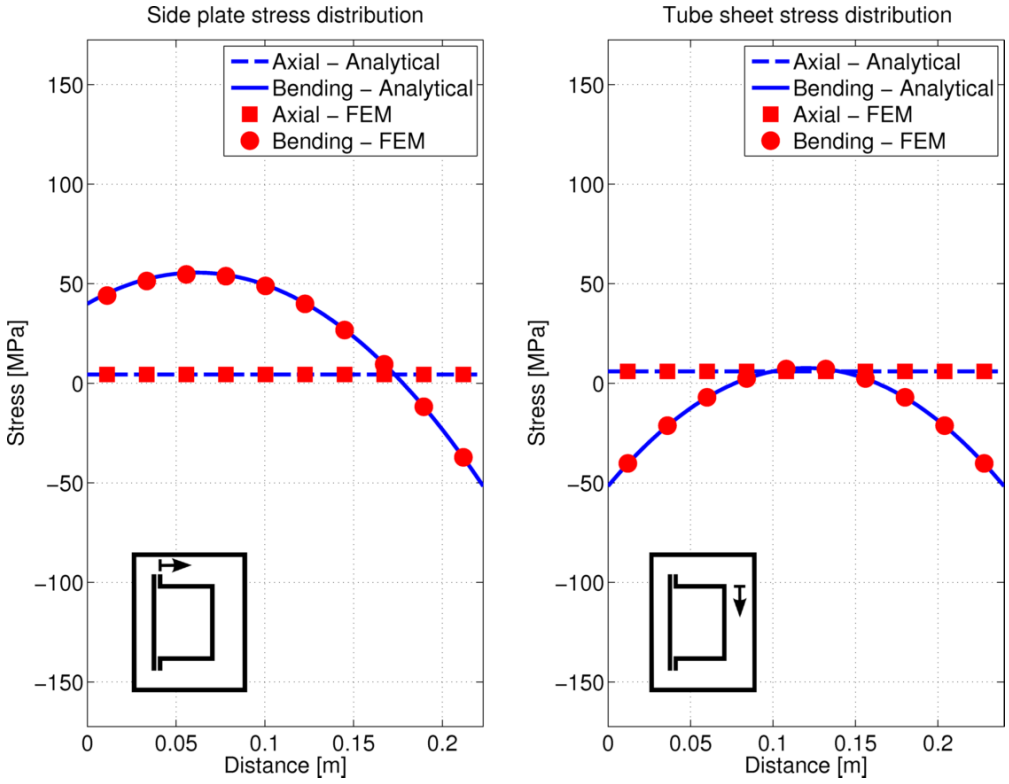

Figure A-10: Rigid frame stress distribution for constrained fixed supports

A.2.3 Unconstrained hinged supports model

- ***Superimposed solutions compared to 1D FEM***

The unconstrained hinged supports model presents a statically determinate problem which may be solved directly from the equations for equilibrium. In Figure A-11 a combined stress plot of the FEM solution for this case is presented, and in Figure A-12 it is compared with the analytical solution.

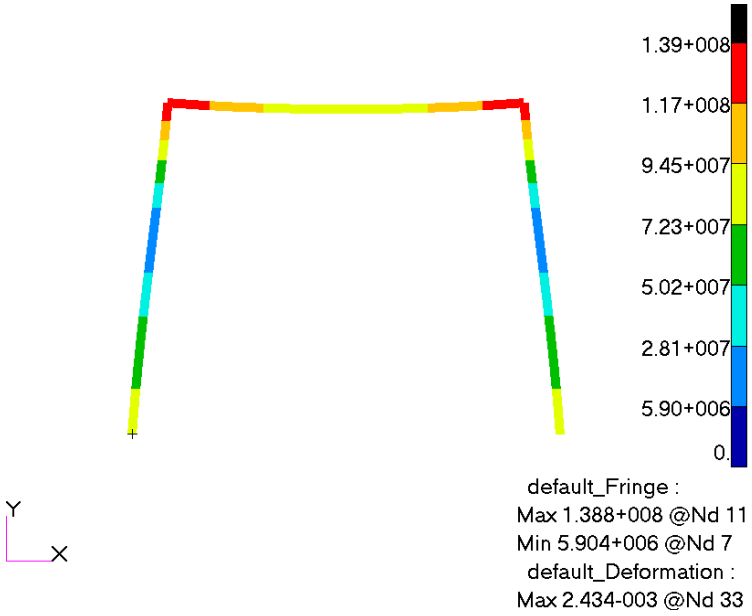

Figure A-11: Unconstrained hinged supports scenario (deformation scaled by a factor of 20)

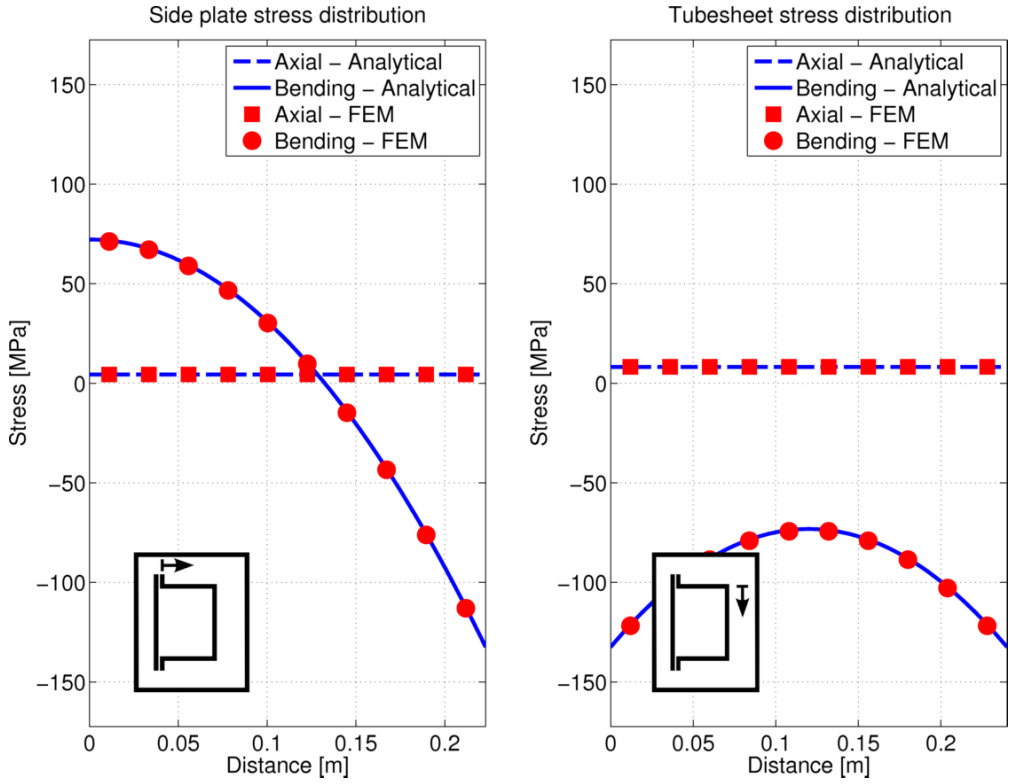

Figure A-12: Rigid frame stress distribution for unconstrained hinged supports

A.2.4 Unconstrained fixed supports model

- ***Solution to the pressure loading problem***

The two scenarios considered to meet the overall slope deformation requirement mentioned in Section 5.2.2.2 are depicted in Figure 5-13, where the "dummy" load M_1 is introduced. Solving the

overall slope deformation of each of these scenarios and setting their sum equal to zero, the reaction moment M_1 may be solved for (see Equation (A-25)).

$$\theta_A + \theta_B = 0$$

$$\left(2\int_0^h \frac{M_1}{EI_1}dy + \int_0^L \frac{M_1}{EI_2}dx\right) + \left(2\int_0^h \frac{Py^2}{2EI_1}dy + \int_0^L \frac{Ph^2 + Px^2 - PLx}{2EI_2}dx = 0\right) = 0$$

$$M_1\left(\frac{2h}{I_1} + \frac{L}{I_2}\right) + \left(\frac{Ph^3}{3I_1} + \frac{6PLh^2 - PL^3}{12I_2}\right) = 0$$

$$M_1 = \frac{Ph^3/3I_1 + P/I_2\left(Lh^2/2 - L^3/12\right)}{2h/I_1 + L/I_2} \qquad \textbf{(A-25)}$$

- ***Superimposed solutions compared to 1D FEM***

With the reaction M_1 known the nominal stress distribution can be found, and subsequently compared to superimposed results from a one-dimensional finite element model. The overall stress distribution following from the analytical evaluation is depicted in Figure A-13 in direct comparison with FEM results.

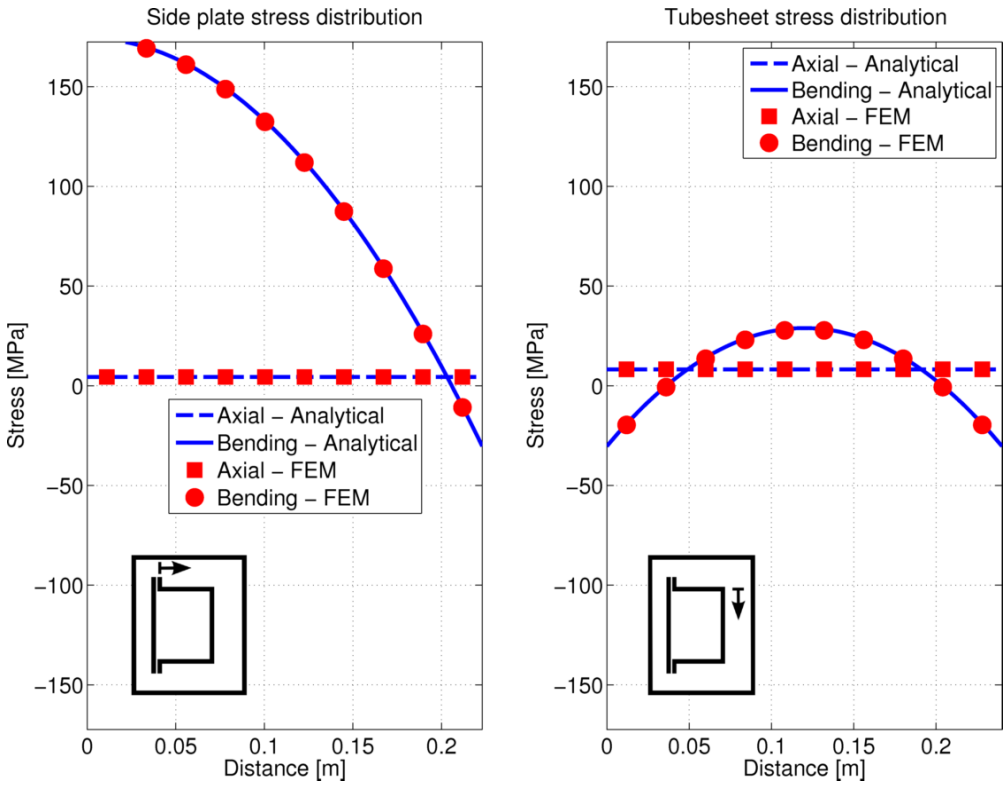

Figure A-13: Stress distribution throughout rigid frame for unconstrained built-in supports

Appendix B: Numerical implementation of the linearization method

- ***Extended trapezoidal rule:***

$$\sigma_{ij,m} \approx \frac{h}{t}\left[\left(\frac{1}{2}\sigma_{ij}\left(x_s^1\right)+\sum_{k=2}^{N-1}\sigma_{ij}\left(x_s^k\right)+\frac{1}{2}\sigma_{ij}\left(x_s^N\right)\right)\right] \quad \textbf{(B-1)}$$

$$\sigma_{ij,b} \approx \frac{6h}{t^2}\left[\sum_{k=1}^{N-1}\left(\frac{\sigma_{ij}\left(x_s^k\right)\times\left(t/2-x_s^k/2\right)+\sigma_{ij}\left(x_s^{k+1}\right)\times\left(t/2-x_s^{k+1}/2\right)}{2}\right)\right] \quad \textbf{(B-2)}$$

Where

$t =$ thickness of section;

$x_s =$ coordinate along section;

$\sigma_{ij}\left(x_s^k\right)=\sigma_{ij}$ at point k along section;

$h =$ the uniform interval size;

$N =$ the number of intervals.

Appendix C: Sensitivity of the header box to nozzle loading

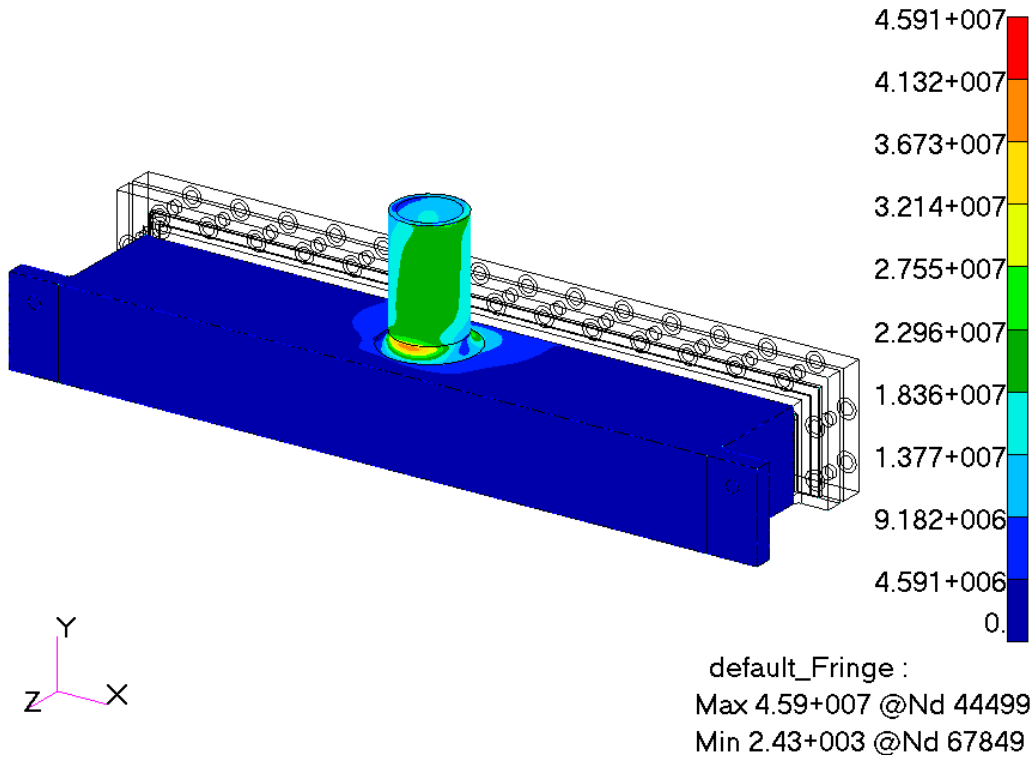

Figure C-1: Isometric representation of equivalent stress distribution subject to an assumed API nozzle loading only

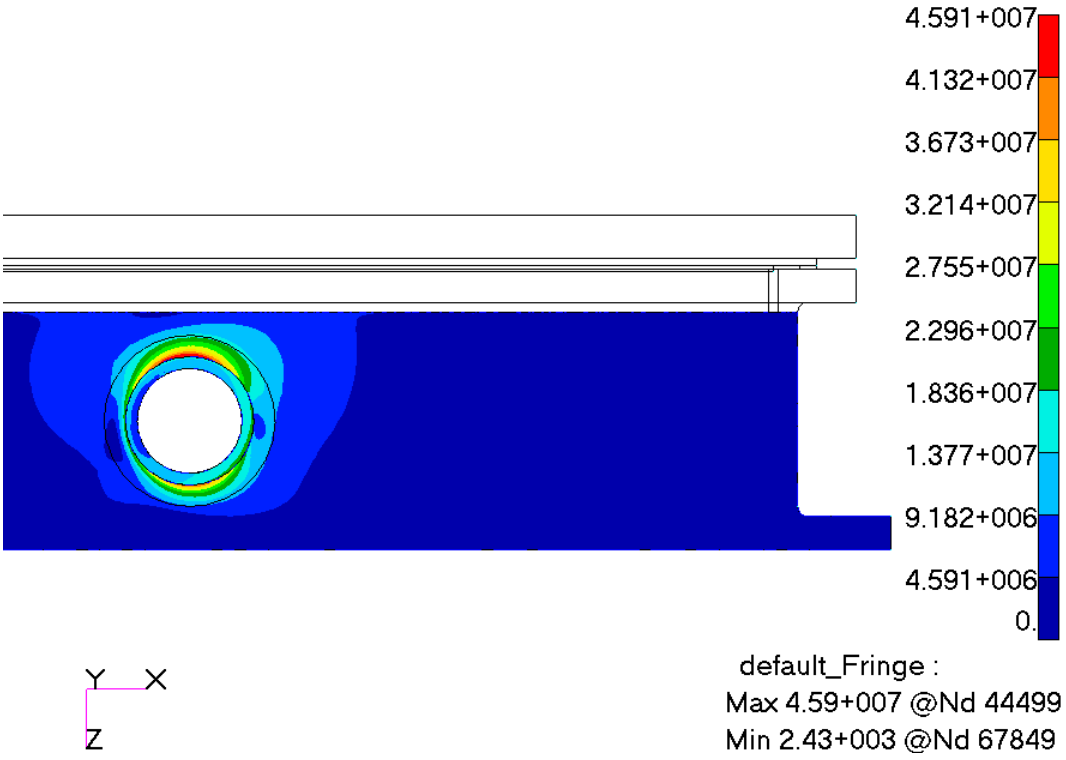

Figure C-2: Top view of the equivalent stress distribution subject to an assumed API nozzle loading only

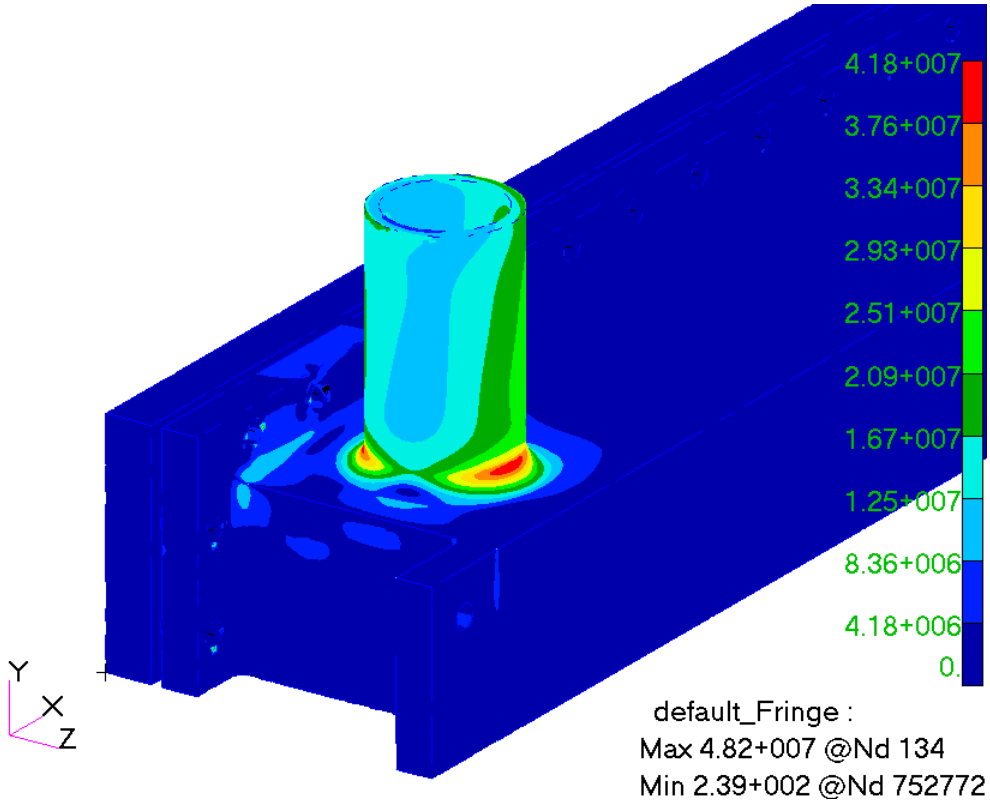

Figure C-3: Isometric representation of equivalent stress distribution subject to assumed API nozzle loading only (nozzle placed at far end)

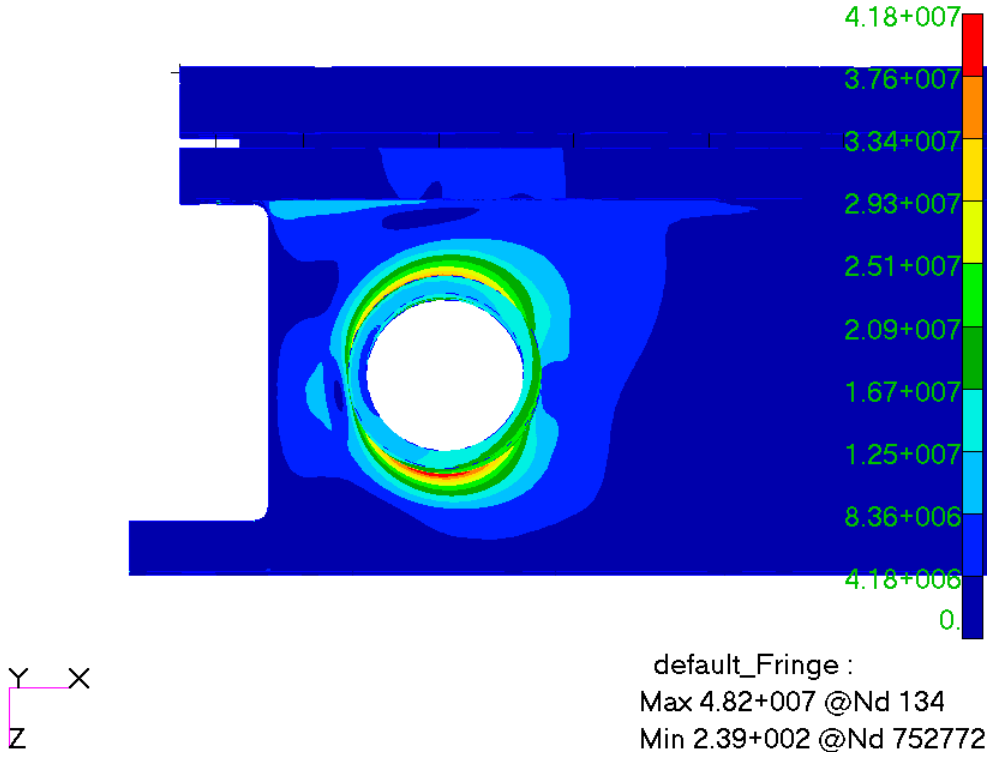

Figure C-4: Top view of the equivalent stress distribution subject to an assumed API nozzle loading only (nozzle placed at far end)